Acoustical tweezers based on acoustical vortices, for selective, 3D and contactless manipulation of micrometric particles and cells

Roudy Al Sahely

Université de Lille

iemn

ACOUSTICAL TWEEZERS BASED ON ACOUSTICAL VORTICES, FOR SELECTIVE, 3D AND CONTACTLESS MANIPULATION OF MICROMETRIC PARTICLES AND CELLS

Doctoral Thesis in Acoustics

University of Lille
Doctoral school "ENGSYS"
Research unit "IEMN"

Presented by:

ROUDY AL SAHELY

Defended on the 31st of March 2022

Thesis Committee:

Jean-François MANCEAU	Professeur de l'Université de Franche-Comté	Reviewer
Frédéric SARRY	Professeur de l'Université de Lorraine	Reviewer
Virginie HOËL	Professeur de l'Université de Lille	Jury President / Examiner
Michael BAUDOIN	Professeur de l'Université de Lille	Supervisor
Olivier BOU MATAR	Professeur de l'Université de Lille	Supervisor / Invited Member

PINCES ACOUSTIQUES BASÉES SUR LES VORTEX ACOUSTIQUES POUR LA MANIPULATION SÉLECTIVE, 3D ET SANS CONTACT DE PARTICULES MICROMÉTRIQUES

Thèse de doctorat en Acoustique

Université de Lille
Ecole doctorale "ENGSYS"
Unité de recherche "IEMN"

Présenté par:

ROUDY AL SAHELY

Soutenue le 31 Mars 2022

COMITÉ DE THÈSE:

Jean-François MANCEAU	Professeur de l'Université de Franche-Comté	Rapporteur
Frédéric SARRY	Professeur de l'Université de Lorraine	Rapporteur
Virginie HOËL	Professeur de l'Université de Lille	Président du jury/ Examinateur
Michael BAUDOIN	Professeur de l'Université de Lille	Co-directeur
Olivier BOU MATAR	Professeur de l'Université de Lille	Co-directeur / Membre invité

Acknowledgment

After finishing my master's internship at PHLAM – Lille, I had the opportunity to pursue my passion in research by starting this thesis in acoustics at the Institut d'électronique de microélectronique et de nanotechnologie laboratory, team FILMS. During my doctoral thesis, I became familiar with the different fabrication process and gained knowledge in acoustics, fluid mechanics and microfabrication. I would therefore like to thank this team who put their confidence in me to join their laboratory.

I would like to start by thanking my supervisor, Mr. Michael BAUDOIN, who guided me through these three years. He was always available for help, and gave me the courage I needed to develop my work. In addition to his positivity and motivation that always pushed me forward to be the better version of myself. I would also like to thank my 2nd supervisor Mr. Olivier BOU MATAR for his presence whenever I needed him. I had the pleasure to work with these two successful men, who helped me gain the scientific knowledge and the confidence I have today.

In addition, I would like to thank all the jury members for agreeing to review this work and for their fruitful discussion during my defense. My thanks therefore go to Mr. Jean-François MANCEAU and Mr. Frédéric SARRY who agreed to be the reviewers of this work, and to Ms. Virginie HOEL who agreed to be the examiner and the jury President.

When I first started my thesis with FILMS team at the IEMN laboratory, I was immediately welcomed as a member of this team. They certainly became not only colleagues, but also friends. I would like to thank Mr. Zhixiong GONG who was always encouraging and reminding me to stay humble and "not to be too proud", Mr. Ravinder CHUTANI for his everyday support, Mr. Jean-Claude GERBEDOEN for helping me to gain knowledge in fabrication process. I would like to thank other colleagues such as Samir and Udita.

When I moved from Lebanon to France, I met beautiful people inside out that were always supporting me through this journey. A big thank you goes to Mohammad Kalaagi, Perla Alalam, Salim Assaf, Jennifer Rached, Valentin Adamczyk. I would also like to thank all my Lebanese friends in Lille for their help and support.

In addition, I would like to thank one of the dearest persons to my heart that has been by my side since the first day I started my journey and was always there especially on the bad days trying to support, giving me hope and doing his best so that I get back stronger. Thank you Joseph El Kettaneh for your everlasting love and support.

Many of my Lebanese best friends also moved to France, and therefore shared with me my experience. I will start with a big thank you to the closest people to my heart, Mirella Katrib and Stephanie El Kalamouni, for their daily support and their amazing friendship. I want to also thank my friends outside France that have been also supporting me and sending me all the love from all over the world. Thank you Sandi Saardi, Maya Meselmani, Rita Hashash and Eliane Kahwaji.

Three years ago, I had to leave my country and adapt to a new culture and a new lifestyle to pursue my dreams. It was a beautiful experience, but the hardest part was being far from my family. Distance might have separated us, but they always remained next to me, closer than ever, and for that, I will always be grateful. The biggest thank you goes to my parents, for the education they offered me, and their unconditional love and support. I am forever grateful to them because they helped me become the successful man I am today. A big thank you to my mother for all her prayers, and for her daily support and motivation. I would also like to thank my sister for all her motivation and her love. Having them in my life is a blessing, and they all helped me evolve in my life and during my thesis. I would also thank my brother that he is watching me from heaven and I hope he is proud of me and of my achievements.

Last but not least, I would like to thank God for all the beautiful opportunities he offered me in life, for all the daily miracles he blessed me with and for all the angels he put in my path.

Contents

Abstract

Acoustical tweezers enable the manipulation of particles collectively or selectively with the acoustic radiation force. By comparison to their magnetic and optical counterparts, acoustical tweezers offer complimentary advantages for particle manipulation. One of the issue with optical tweezers is the sample overheating due to the tightly focused laser beam that can induce photodamage [1, 2]. Thus, manipulating bio-samples using optical tweezers is limited, especially when forces $\geq$ 100 pN are required. On the other hand, magnetic tweezers have a low trap stiffness and they can only trap magnetic particles. Otherwise pre-tagging the target particle is required [3]. Acoustical tweezers overcome all these difficulties. The radiation pressure in both optics and acoustics is proportional to the intensity of the incoming wave divided by the speed of the wave. Thus, much larger forces can be applied in acoustics than in optics at the same wave intensity, since the speed of acoustic waves in liquids is five orders of magnitude smaller than speed of light [4]. Moreover, pre-tagging is not required in acoustical tweezers since acoustic radiation force can be applied on any type of particles with a density and/or compressibility contrast with the surrounding medium. In addition, particles with sizes ranging from hundreds of nanometers to millimeters can be trapped and manipulated using acoustical tweezers, since ultrasonic sources are available from kilohertz to gigahertz frequencies.

Early developments of acoustical traps were first made by King et al. [5] and by Sölner and Bondy [6]. Initial systems were based on standing waves that can trap particles at the nodes or anti-nodes depending on their acoustical properties. Recently, scientists emerged towards using surface acoustic waves to trap smaller particles in microfluidic devices [7, 8], that led to renewed interest in the field, especially with the important developments that have been made in practical applications in biology [9]. Standing waves and surface acoustic waves can only manipulate particles collectively due to the multiplicity of nodes and antinodes unless there is only one particle present in the system. This multiplicity prevents selectivity (i.e. the ability to trap

and manipulate a particle independently of other neighbouring particles). Moreover, they require some transducers or reflectors to be positioned on each side of the trapping area to achieve a 3D trap.

Wu [10] investigated the possibility to use focused waves as in optics in order to develop selective tweezers. Even though, selectivity can be achieved using focused beams, most particles of practical interest (solid particles, cells) are expelled axially and/or laterally from the focal point. Hence, it is not possible to obtain a three-dimension (3D) trap.

Baresch et al. [11] were the first to propose a solution to solve these issues by using some specific wavefields called spherical acoustical vortices. They correspond to focused helical waves spinning around a phase singularity. They have a pressure intensity minimum at the focal point surrounded by a high intensity bright ring that can ensure the trap of a particle. One of their properties is that these waves are non-diffracting and carry orbital momentum [12]. The ability to trap particles in 3D with a one-sided synthesis system has been demonstrated experimentally by Baresch et al. [4]. The complex transducer array that has been used by Baresch et al. [4] can be replaced by a single spiraling interdigitated transducer as demonstrated by Baudoin et al. [13], which enables selective particle manipulation in a standard microscopy environment. These spiraling transducers are cheap since they are fabricated in a clean room using simple photolithography techniques, easily integrable since they are flat and transparent, and compatible with disposable substrates.

Thesis outline

While tremendous progress have been achieved in the last decades on selective acoustical tweezers, our aim during this PhD was to address the following unsolved issues:

1) Designing acoustical tweezers that are able to trap and manipulate selectively cells in a standard microscopy environment (Chapter 4). This project was achieved with 40 MHz acoustical tweezers based on active holographic spiraling IDTs (S-IDTs) producing trap size close to the size of the cells.

2) Designing high frequency tweezers that can trap and manipulate selectively very small micron-size particles in two dimensions, with NanoNewton forces (Chapter 5). This aim was achieved by designing some 250 MHz acoustical tweezers.

3) Finally, the last objective was to investigate the 3D trapping ability of one-sided acoustical tweezers based on holographic spiraling IDTs and in particular the possibility to translate the trapped object along the propagation axis by shifting the driving frequency (Chapter 6).

In this manuscript, we first introduce the relevant bibliography and key concepts in Chapter 1 and then the experimental and numerical methods used in this work in Chapters 2 and 3. Then we detail how each of these issues are addressed in chapters 4 to 6. Note that the results of Chapter 4 have been published in [14], that the results of Chapter 5 have been submitted recently to the journal "Physical Review Applied" and that 2 others publications are envisioned on Chapter 3 and 6.

Chapter 1

Introduction

1.1 Contactless tweezers

Contactless micro-particle and micro-organisms manipulation is of primary interest for microfluidics, microrobotics, micro/nano-medicine, or tissue engineering [13]. Different methods have been developed in the last decades for contactless manipulation including magnetic, optical and even acoustical tweezers.

1.1.1 Magnetic tweezers

Magnetic tweezers are based on permanent electromagnetic or superconducting magnets, which generate magnetic fields that can levitate particles. Some of the advantages of using magnetic tweezers are their low cost and their simplicity of implementation. The canonical implementation is shown in Figure 1.1.

A flow cell is placed on an inverted microscope, and a magnet is positioned above this flow cell [15]. The most common implementation is based on a pair of permanent magnets, but implementations based on the near-field of a single permanent magnet [16] or on electromagnets [17, 18] have also been reported. A magnetic moment is induced on the paramagnetic bead due to the applied magnetic field, and a force proportional to the gradient of this field is experienced by the bead. For paramagnetic beads in the micrometric range, forces between 10 and 100 pN can be readily exerted [19] by using magnets. The magnetic field gradient varies on a large length scale (of the order of 1 mm) [15], which leads to low trap stiffness and hence selectivity [3] (the ability to trap an object independently of other neighbouring objects).

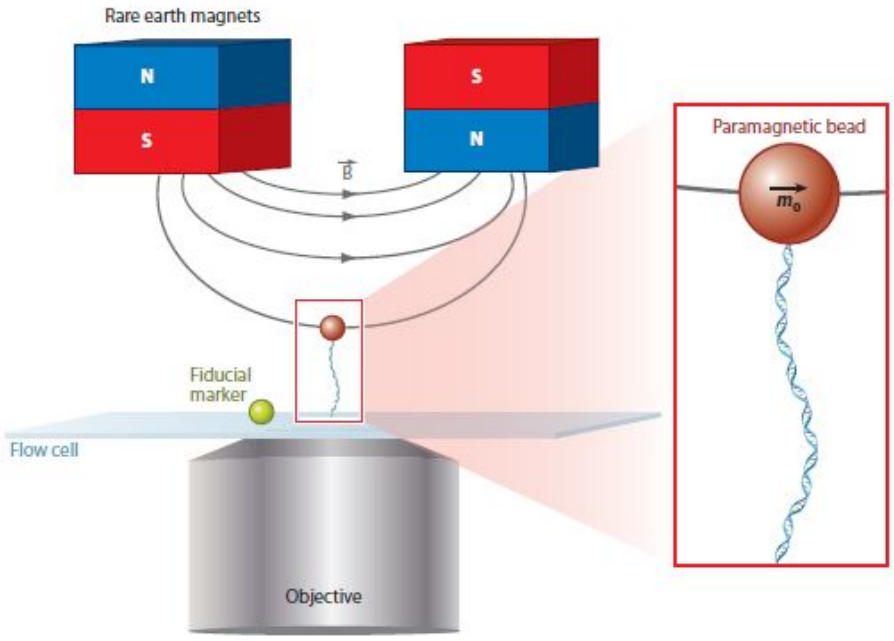

Figure 1.1: Schematic of basic implementation of magnetic tweezers. Magnetic moment m_0 is induced on the paramagnetic bead due to the magnetic field generated by a pair of magnets. A force proportional to the gradient of the field is experienced by the bead. By rotating the external magnet, the molecule can be coiled [15].

In addition to this limited selectivity, magnetic tweezers have some limitations due to the fact that they only enable the manipulation of magnetic particles. Otherwise they require the target particle to be pre-tagged.

1.1.2 Optical tweezers

In the last decades, contactless manipulation [1, 20] based on optical forces has been developed. Arthur Ashkin won a Nobel prize in 2018 due to his development of optical tweezers. By the help of the optical radiation force, particles can be freely suspended and accelerated (Figure 1.2). Ashkin et al. [1] developed single beam optical tweezers and showed that dielectric particles can be trapped by a focused laser beam due to gradient force, confirming the concept of negative light pressure (pulling a particle using light). It has been demonstrated that optical tweezers are able to trap viruses and bacteria by laser radiation pressure with single beam gradient traps [21, 22].

Even though optical tweezers are powerful tools for bio-molecular manipulation, they require high powered lasers that can damage biological samples

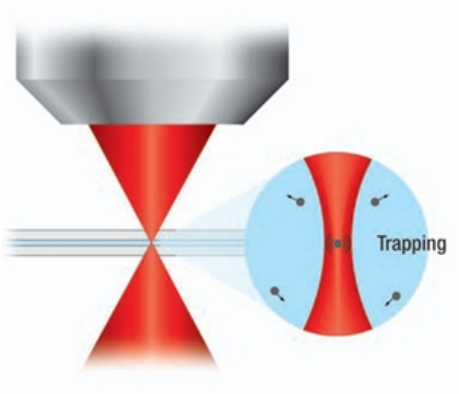

Figure 1.2: General scheme of optical tweezers [23].

[24, 25]. In addition, the radiation pressure is proportional to the wave field intensity divided by its speed of propagation (I/c_0). Since light intensities at the focus field are of the order of 10^7 – 10^8 W/cm^2, this can lead to heating both the object and the trapping medium, due to optical absorption, which limits the use of OTs for some applications. Moreover, since the speed of light is very high ($c_l = 3 \times 10^8$m/s), weak forces are yielded on micron-sized objects in the range of pN [4].

1.1.3 Acoustical tweezers

Similarly to optics, radiation forces can be applied on objects such as particle or cells using acoustic waves. The acoustical radiation force is a result of the non-linearities of Navier-Stokes equations but also a consequence of the averaging of the stress tensor over a vibrating surface. A major advantage of acoustical tweezers compared to their optical counterpart is that (i) since the acoustical radiation force is also proportional to I/c_0 and (ii) the speed of sound c_0 is several order of magnitude smaller than the speed of light, forces of 5 orders of magnitude higher on the force can be expected at same input power when using sound instead of light [4]. Furthermore, highly efficient piezo-electric sources are available with frequencies from kHz up to GHz, enabling manipulation from macroscopic to microscopic length scales, broadening the range of the size of the particles to be trapped. Moreover, acoustical tweezers have significantly higher efficiency due to their high radiation force and low power operation, which is critical for cell manipulation applications [26]. Thus, they are becoming fundamental tools for disease

diagnosis [27], laboratory on a chip manipulation [14], and in vivo applications such as the manipulation of kidney stones [28]. Moreover, they can manipulate matter in both liquids and gases.

There are two main types of acoustical tweezers; the first relies on standing plane waves and enables simultaneous multiple particle trapping, and the second is based on acoustical vortices and enables 3D selective particle trapping with a single beam (a beam produced from only one direction of space). Trapping of elastic particles with a gradient force of a single acoustic beam was first reported in three dimensions by Baresch [4]. They reported the first 3D trap and selection of one particle independently of its neighbors. A strong focalization of the acoustical vortex was required for this operation [11].

1.2 Acoustofluidics and non-linear acoustics

Acoustofluidics is defined as the use of non-linear acoustic effects to manipulate particles and fluids at small scales. Acoustic radiation force and acoustic streaming are the two main non-linear effects that can be used for these manipulations and will be discussed further in the following sections. Time averaged force acting at the interface between two media with different acoustic properties (density, sound speed) is called acoustic radiation pressure, as it is exposed to an acoustic field. While the time-averaged motion of the fluid due to the energy transfer from the acoustic field to the fluid is called acoustic streaming. Faraday was the first to describe these two phenomena in 1831 [29]. Kundt is often cited for his his famous cork dust experiment that has been made in 1874 [30] and illustrated radiation force. Both the acoustic pressure force and acoustic streaming have been widely theoretically investigated in the past [31, 5, 32, 33, 34].

1.2.1 Acoustic radiation force

Acoustic radiation pressure or more precisely acoustic radiation force (Figure 1.3) is a hydrodynamic force exerted at the interface between two media with different acoustical properties. Various physical effects can produce acoustic radiation force [35] like change in the density of the energy of the propagating wave due to wave absorption or scattering. This absorption and scattering can result from the presence of inclusions, walls or fluidic interfaces. Many

scientific and technical applications include acoustic forces such as acoustic levitation, acoustic coagulation of aerosols, calibration of sound transducers, biomedical ultrasonics [36]. They also play an important role in acoustic cavitation [36]

Particle manipulation was first described and by Kundt and Lehman in 1866 and tested experimentally on dust particles. The particles were organized in a series of bands by the acoustic forces at the nodes of the ultrasonic standing waves. King [5] in 1934 proposed an expression for the acoustic radiation force for rigid spheres freely suspended in non-viscous fluid that are exposed to standing and traveling plane waves. In 1955 Yosioka and Kawasima [37] found a good agreement between the theoretical and experimental data after extending King's theory to compressible spheres. In 1962, Gor'kov proposed an expression of acoustic radiation force exerted on a spherical particle in the long wavelength regime (LWR), that is to say when the wavelength is much larger than the size of the particle [34]. Bruus [38] and Andersen [39] further detailed the determination of the acoustic force that has been proposed by Gor'Kov [34], and extended it to include thermo-viscous effects. More recently some general expressions of the acoustic radiation force exerted on a spherical particle by an arbitrary beam have been derived [40, 41, 42, 43].

Primary and secondary radiation force

When a wave impinges, a suspension of particles the radiation force is generally divided into "primary" and "secondary" radiation force.

• Primary radiation force:

The primary radiation force is the force which results from the direct interaction between the incident field and a particle. This primary force is sensitive to several factors, including the size of the particle, but also the compressibility and the density of both the particle and the suspending fluid [44]. Due to the high order of magnitude of the acoustic force, micron sized particles [45, 46], lipids [47], cells [48] or even bacteria [49] are influenced by this force.

• Secondary radiation force:

Secondary radiation force results from the interaction between neighbouring particles. They generally become significant when particles are close

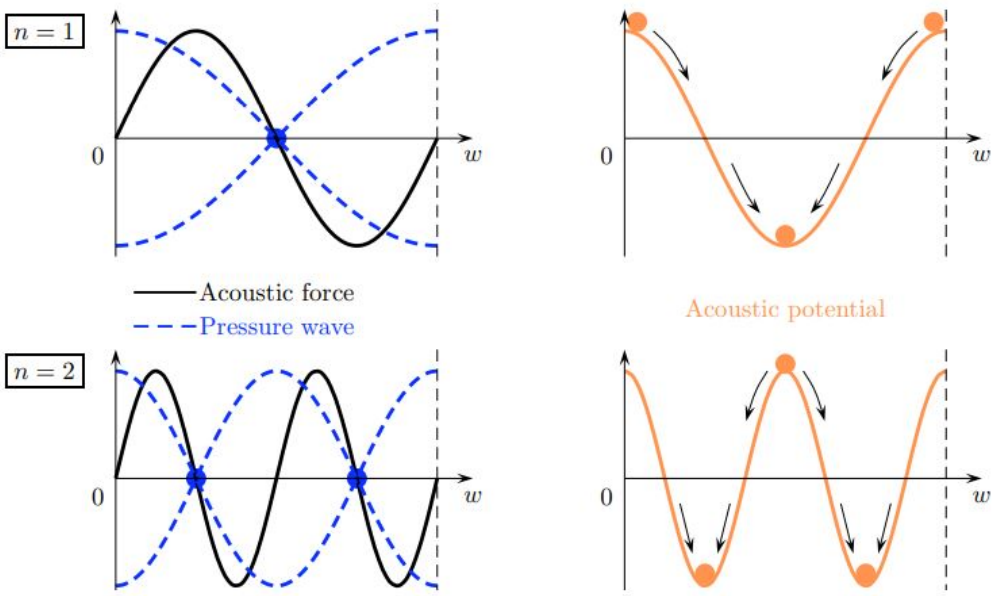

Figure 1.3: Left side: graphs representing a wave with one ($n = 1$) or two ($n = 2$) pressure nodes, the acoustic force (solid line) and the corresponding pressure field (dotted lines). Left side: graphs representing for the same values of n, the acoustic potential from which the force derivate. Stable equilibrium positions are the ones that have a minimum of potential that correspond to the pressure nodes. This figure has been taken from [50].

enough to each other. Secondary radiation force can be responsible of particle aggregation process. Bjerknes secondary forces [27] is an example of these inter-particle forces for bubbles [51].

Acoustic radiation force in the LWR

• Gor'kov potential:

The fluid exerts hydrodynamical forces on particles when they are suspended in the field of a sound wave. These forces are proportional to the acoustic velocity of the fluid in the linear approximation which leads to a harmonic motion of the particle but no net motion. Average forces arise as the result of the second order nonlinear effects acting on the particle [34]. A very simple and useful expression of the acoustic radiation force exerted by a standing wave on small particles compared to the wavelength (R$\ll \lambda$) was established by Gor'kov. It is written under the form of an acoustic potential $U(\vec{r})$ from which derives the force according to the expression [34]:

$$\vec{F}_{ac} = -\nabla\vec{U},$$

with $U(\vec{r})$ the acoustic potential:

$$U(\vec{r}) = V[f_1\langle PE\rangle(\vec{r}) - \frac{3}{2}f_2\langle KE\rangle(\vec{r})], \tag{1.1}$$

R the radius of the particle, $V = \frac{4\pi R^3}{3}$ the volume of the sphere, and where $\langle PE\rangle(\vec{r})$ and $\langle KE\rangle(\vec{r})$ are respectively the averaged potential and kinetic acoustic energies over a period of the acoustic wave. Their expressions are given by:

$$\langle PE\rangle(\vec{r}) = \frac{\beta_f}{2}\langle p_f(\vec{r},t)^2\rangle,$$

$$\langle KE\rangle(\vec{r}) = \frac{\rho_f}{2}\langle u_f(\vec{r},t)^2\rangle,$$

with β_f and ρ_f the compressibility and density of the fluid, $\langle p_f(\vec{r},t)^2\rangle$ and $\langle u(\vec{r},t)^2\rangle$ the pressure and velocity mean square fluctuations in the wave at the point where the particle is located, f_1 and f_2 two factors expressed as:

$$f_1 = 1 - \frac{\rho_f c_f^2}{\rho_p c_p^2},$$

$$f_2 = \frac{3(\rho_p - \rho_f)}{(2\rho_p + \rho_f)},$$

and finally c_p and ρ_p are the speed of sound and density of the particle.
If the factors f_1 and f_2 are both positive (corresponding to particles more dense and less compressible than the surrounding fluid), the particle is attracted to regions wherein the potential energy is small and the kinetic energy is large. Hence, the sphere migrates in this case to the velocity anti-node. However, the particle will go to the pressure anti-node if f_1 and f_2 are both negative, because the sphere is attracted to regions where the kinetic energy is small and the potential energy is large [52].

If we combine the above expression the acoustic potential $U(\vec{r})$ becomes:

$$U = 2\pi R^3 \rho_f \left(\frac{\langle p_f^2\rangle}{3\rho_f^2 c_f^2} f_1 - \frac{\langle u_f^2\rangle}{2} f_2\right). \tag{1.2}$$

The expression of the acoustic force in the case of a plane stationary wave turns into [34]:

$$\vec{F} = 4\pi\langle E\rangle R^2 (kR)\sin(2kx)\left(\frac{\rho_p + 2/3(\rho_p - \rho_f)}{2\rho_p + \rho_f} - \frac{1}{3}\frac{c_f^2\rho_f}{c_p^2\rho_p}\right). \tag{1.3}$$

with $k = \omega/c_o$ the acoustic wave number and $\langle E \rangle$ the averaged acoustic energy. Many researchers use Gor'kov potential for particle manipulation, but it has limitations since it is only valid for small particles compared to the wavelength.

Acoustic radiation force above the LWR

To treat the general problem of the acoustic radiation force and torque applied on a spherical particle of arbitrary size by an arbitrary acoustic field, three issues must be solved. First, the incident field must be decomposed into a sum of elementary waves which enable the resolution of the scattering problem. In the angular spectrum method, the incident field is decomposed into a sum of plane wave [41, 43]. While the incident field is decomposed into a sum of spherical waves in the multipole expansion method [53, 40, 42]. Second, the scattering problem must be solved. This task is complexified for an arbitrary wave by the non axisymmetry of the incident acoustic field. In the angular spectrum method, Sapozhnikov and Bailey [41] used the known solution of the scattering problem of a plane wave by a sphere and the Legendre addition theorem to solve this issue. While the scattering problem was solved for an arbitrary spherical wave in the multipole expansion method. Baresch et al. [42] showed that the problem degenerates to the one of an incident plane wave so that the classical scattering coefficients can be used. Third, by integrating the time-averaged linear and angular radiation stress tensor over the particle surface, the force and torque can be calculated. One major difficulty to compute the integral of the stress tensor or angular stress tensor comes from the fact that the surface of the particle is vibrating. This problem can be overcome in two ways: The first one relies on using Lagrangian coordinates instead of Eulerian coordinates. The second one, first introduced by Brillouin [54] relies on the transfer of the integral into a still surface by subtracting the flux of momentum to the stress tensor for the force, and the flux of angular momentum to the angular stress tensor for the torque. Gong and Baudoin demonstrated the formal equivalence between these different approaches [55].

1.2.2 Scattering theory

The scattering of waves by particles is studied and understood by the scattering theory. As discussed in the previous section, the computation of the acoustic radiation force requires to solve the scattering problem, i.e. to determine the scattering field as a function of the incident field and scatterer properties. When spherical scatterers are considered, it is convenient to de-

compose the incident field and the scattered field (Figure 1.4) into a sum of spherical waves to apply the boundary conditions and solve the scattering problem.

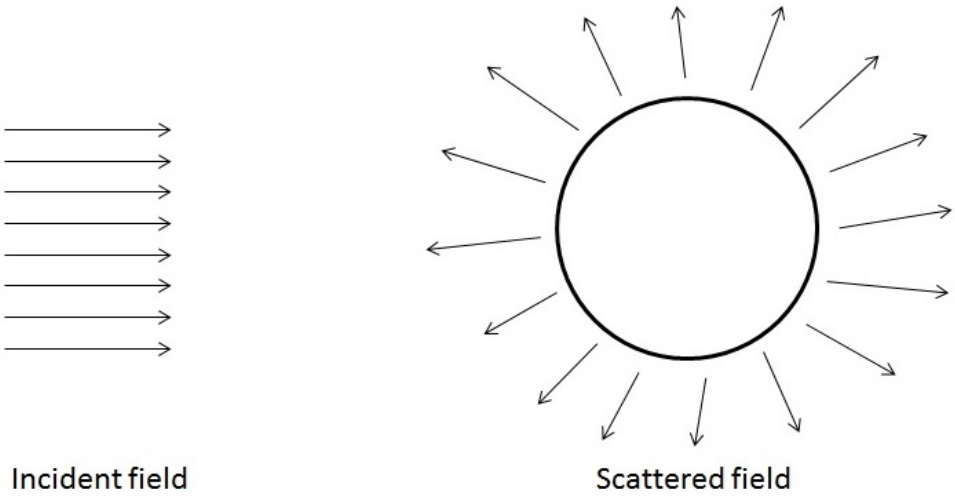

Figure 1.4: Incident and scattered field by a spherical particle.

Decomposition of the incident field

In the multipole expansion method (MEM) [53, 40], the incident acoustic potential is directly decomposed in the spherical waves basis [55]:

$$\Phi_i = \Phi_0 \sum_{n=0}^{\infty} \sum_{m=-n}^{n} a_n^m j_n(kr) Y_n^m(\theta, \varphi) \exp^{-i\omega t}, \tag{1.4}$$

where (r,θ, ϕ) are the spherical coordinates, j_n are the spherical Bessel functions of the first kind, Φ_0 is the potential amplitude, k is the wave-number, a_n^m are the so called incident beam-shape coefficients which set the weight of each spherical wave. While $Y_n^m(\theta, \varphi)$ is the normalized spherical harmonics and is defined by:

$$Y_n^m(\theta, \varphi) = \sqrt{\frac{2n+1}{4\pi} \frac{(n-m)!}{(n+m)!}} P_n^m(\cos\theta) \exp^{im\varphi}, \tag{1.5}$$

The associated Legendre functions is represented by P_n^m. In this expression, the Bessel functions of the second kind has been eliminated and only the Bessel functions of the first kind appear, since in the absence of the scatterer,

the incident field exists, and must be finite at (r = 0), while the Bessel functions of the second kind are singular at this point. The beam shape coefficients for an arbitrary field can be determined by different methods [56].

Scattered field

As the incident field, in the MEM, the scattered field can be decomposed into a sum of spherical waves [55]:

$$\Phi_s = \Phi_0 \sum_{n=0}^{\infty} \sum_{m=-n}^{n} s_n^m h_n^{(1)}(kr) Y_n^m(\theta, \varphi) \exp^{-i\omega t} . \tag{1.6}$$

The beam shape coefficient of the scattered field is presented by s_n^m. Noting that in the scattered field, the Bessel function is replaced by the Hankel function of the first kind. The latter is an outgoing wave like the scattered field, and since the Hankel function of the second kind is a converging wave, thus it is eliminated.

To determine the expression of the scattered beam shape coefficients s_n^m as a function of the incident beam shape coefficients, it is necessary to solve the scattering problem. These coefficients depend on the material composition, particle shape, and surface boundary condition [55]. The complete problem was solved by Baresh et al. [42] for elastic spheres and an arbitrary incident beam through the introduction of three scalar potentials.

1.2.3 Acoustic streaming

Acoustic streaming is a time averaged vortical flow resulting from the absorption of an acoustic wave by the supporting fluid. This absorption can result from the thermal/viscous dissipation in the bulk of the fluid, leading to so-called "bulk" or "Eckart" streaming (Figure 1.5a) or from dissipation near boundaries due to the presence of a viscous/thermal boundary layer, leading to so-called "boundary" or "Rayleigh" streaming (Figure 1.5b). The production of this flow is a second order non-linear phenomenon. Another type of steady flow induced by periodic flow is the so-called "Schlichting" streaming which occurs inside the boundary layer. This last type of streaming is not limited to acoustics and can even occur for incompressible flows. Acoustic streaming can also affect particles since it exerts a drag on a particle.

Rayleigh [31] studied for the first time boundary acoustic streaming in 1884. He addressed three configurations of streaming observed by Faraday and

Dvorak, and also treated the case of standing waves between parallel walls. Among these three cases, two of them were related to the observation that has been made by Faraday on the patterns assumed by sand and fine powders on Chladni's vibrating plates, while the third one is related to the observation on the circulation of air currents in a Kundt's tube made by Dvorak [57].

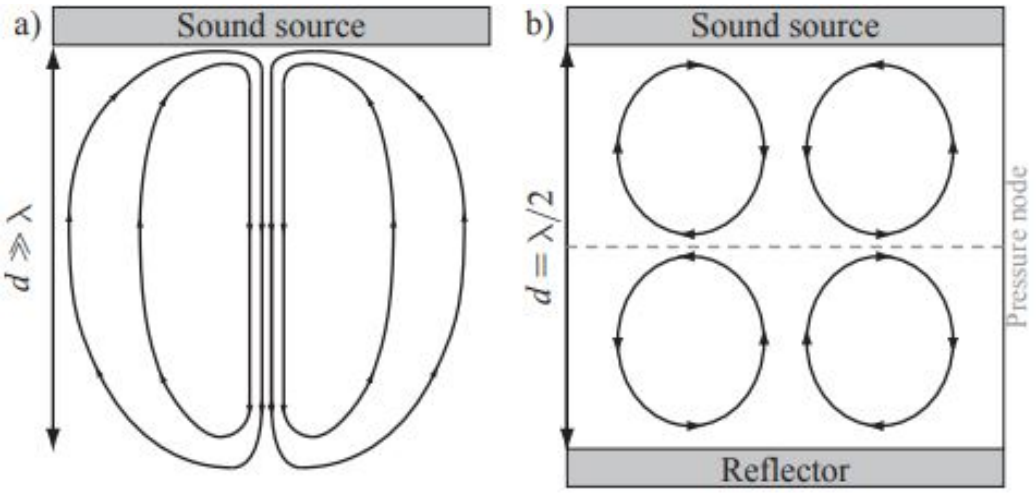

Figure 1.5: Types of streaming. a) Eckart streaming and b) Rayleigh streaming. This image is taken from [58].

1.3 Acoustic manipulation

1.3.1 Acoustic manipulation with standing waves

Standing waves can be produced in different ways: by using opposite transducers synthesizing progressive wave propagating in opposite directions or by exciting the eigen-modes of a cavity. These standing waves can trigger different non linear effects such as acoustic streaming and radiation pressure, which in turn can be used to manipulate particles and fluids.

When a suspension of particles is insonified by standing waves, particles migrate to the nodes or anti-nodes of the wave depending on their size and acoustic properties. Secondary radiation force can also lead to some specific aggregate structures owing to the interaction between the particles.

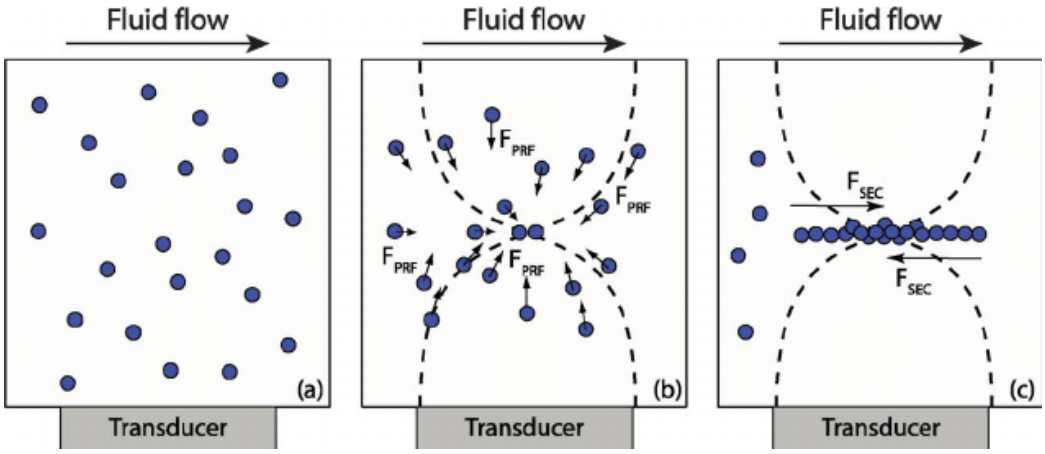

Figure 1.6: General scheme of acoustic forces in an acoustic resonator [59]. a) Ultrasonic resonator containing suspended particles. b) Primary radiation force pulling the particles towards the node. The dashed lines represents the pressure profile. c) Particle aggregation is being formed due to the transverse radiation force and the secondary forces.

In the case of a resonator (Figure 1.6), strong response can be obtained at some specific frequencies corresponding to eigen-modes of the resonator.

1D manipulation

As a start, scientists have used standing waves in order to manipulate particles in one dimension. In particular, long and straight channels were used to trap the particles in 1D only. This enables 1D focusing of particles for, e.g., concentration/sequential washing applications [60, 61], concentration/sorting applications [62, 63], and precise positioning of particles at the end of the channel [64, 65]. As an example, Figure 1.7a shows a device that is made up of microfluidic channel and a pair of interdigital transducers (IDTs) deposited on a piezoelectric substrate in a parallel that are responsible to make a patterning in 1D [66]. When the signal is applied to the transducers, SAWs will be generated and propagate in opposite direction and the particles will be trapped. Figures 1.8a and c show optical images of examples of 1D patterning in such SAW-based devices. The polystyrene beads aggregate at the pressure nodes when the standing surface acoustic wave (SSAW) is applied.

Then people have tried to manipulate particles in more than one spatial dimension simultaneously using ultrasonic standing waves.

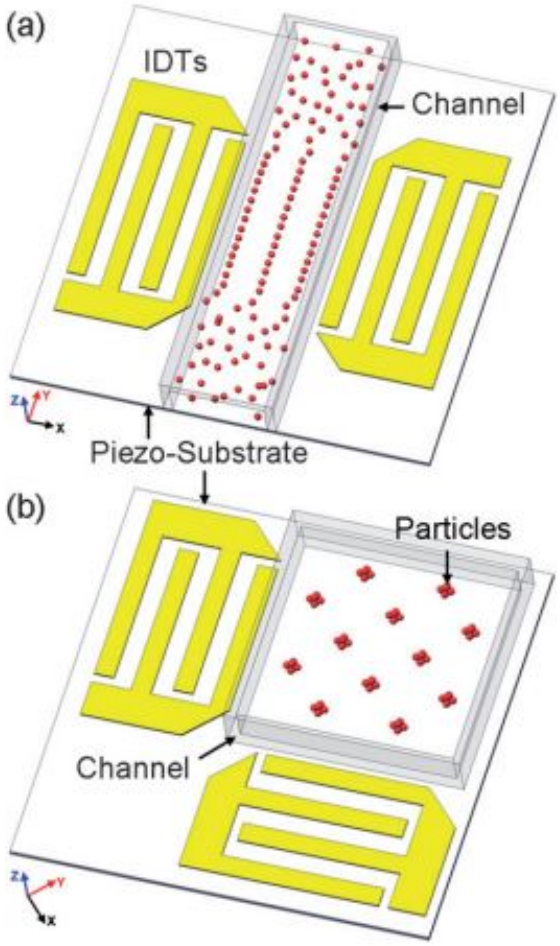

Figure 1.7: Schematic of the standing surface acoustic waves-based patterning devices. a) 1D patterning using two parallel interdigital transducers. b) 2D patterning using two orthogonal interdigital transducers. This figure was taken from [66].

Multi dimensional manipulation

Several ways can be used in order to achieve multi-dimensional manipulation. One way is to use pairs of transducers or transducer/reflector in each spatial dimension. A second way is to excite resonances of 2D and 3D cavities. In this case, different frequencies can be used to select the excited mode and hence resulting pattern. As an example, Figure 1.7b shows a device that is the same as the one mentioned in Figure 1.7a but this time the transducers are perpendicular to each other inducing a 2D pattern [66]. Once the signal is applied to the transducers, SAWs will be generated and propagate in orthogonal directions and the particles will be trapped. Figures 1.8b and d

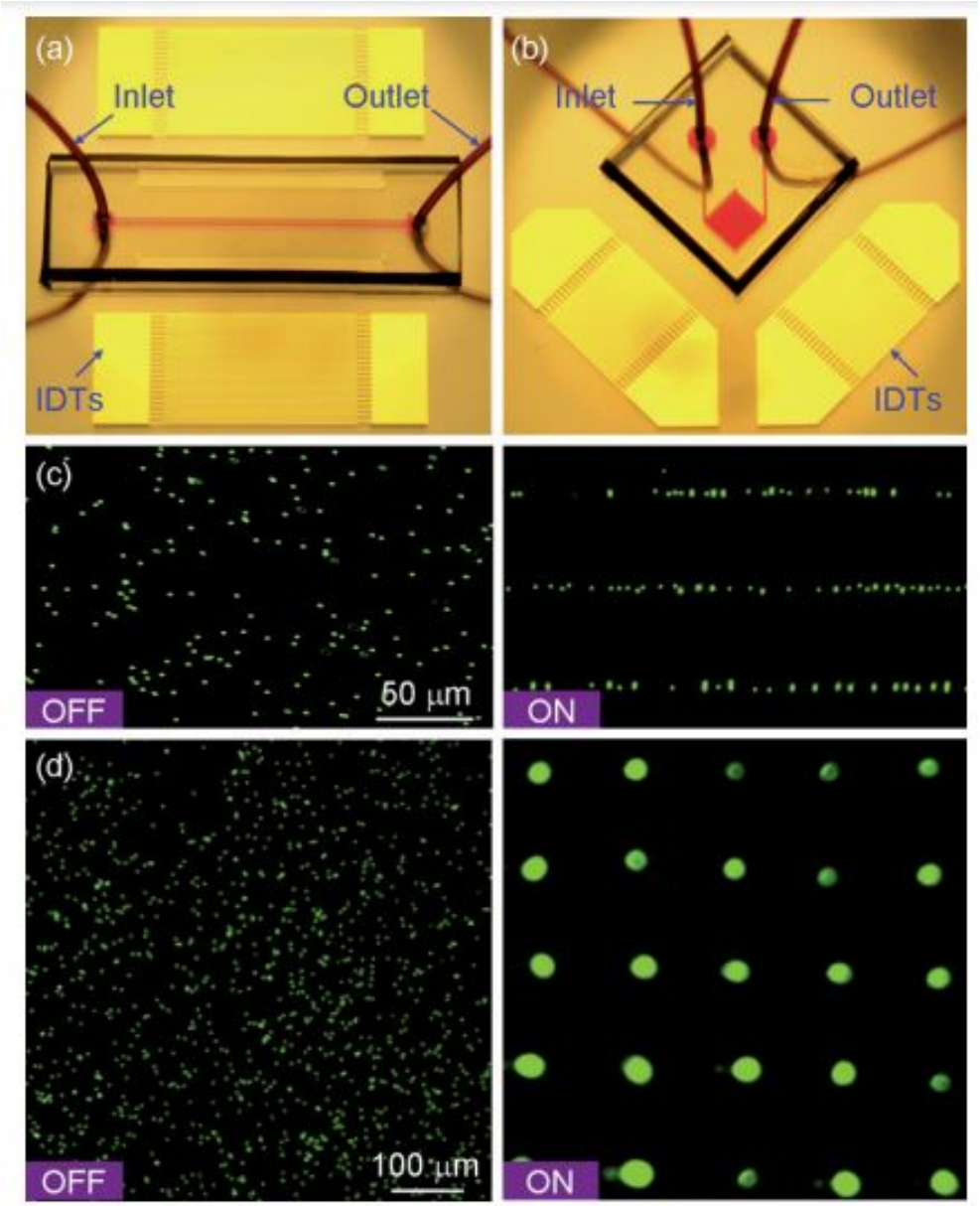

Figure 1.8: Patterning of fluorescent polystyrene micro-beads. Optical images of a) 1D b) 2D patterning experiments of the acoustical tweezers devices. c) Micro-beads distribution before and after exposing them to the acoustic field in 1D. Noting that the micro-channel width is 150 μm and depth is 80 μm. d) Micro-beads distribution before and after exposing them to the acoustic field in 2D. This figure was taken from [66].

show the optical images of the 2D patterning device and the traps.

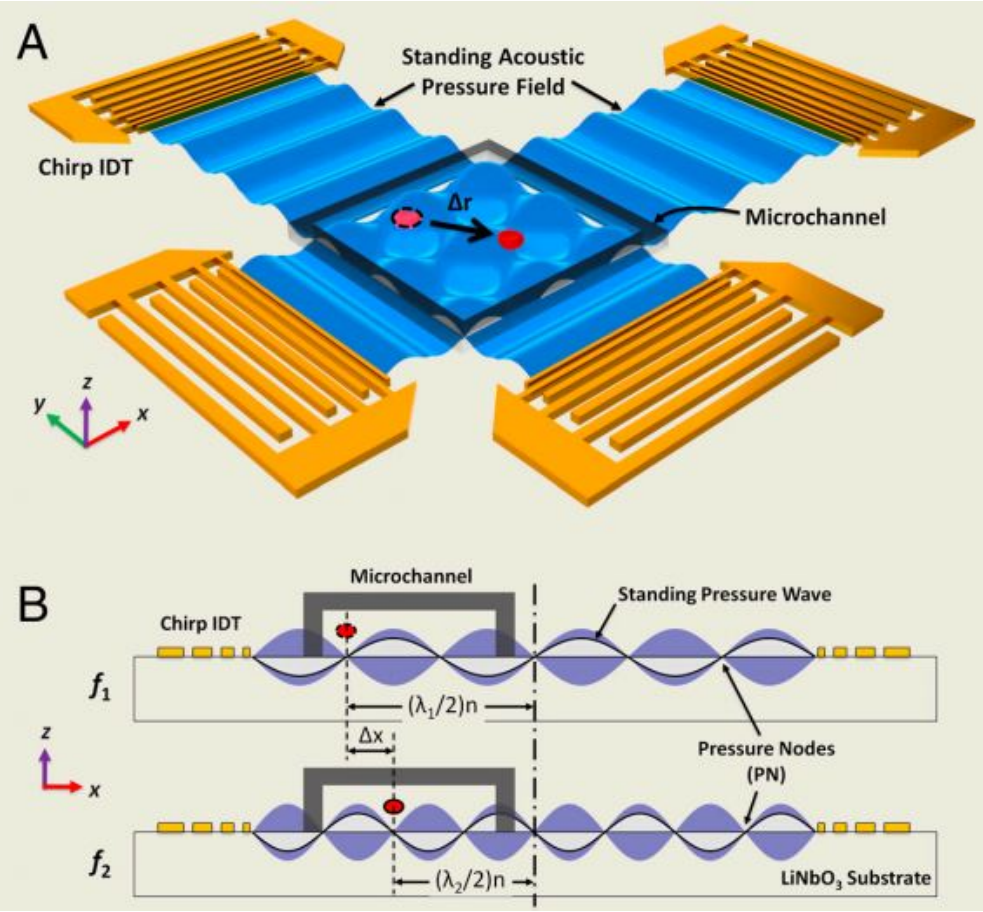

Figure 1.9: Schematic illustrating A) the device structure of an acoustical tweezer that is made up of a microfluidic device with orthogonal pairs of chirped IDTs for generating standing SAW. B) Transducers generating a standing SAW at frequency f_1 and f_2. The particles can be translated a distance of $(\Delta\lambda/2)n$ when particles are trapped at the nth pressure node by switching from f_1 to f_2. This figure was taken from [7].

Note that the position of the nodes and anti-nodes can be moved by using different frequencies for the opposite transducers [7, 8]. An example is shown in Figure 1.9A where a PDMS channel was bonded to a lithium niobate piezoelectric substrate asymmetrically between two orthogonal pairs of chirped IDTs. Each pair of transducers generate SAWs and the interference between them forms standing SAW. Figure 1.9B presents a schematic of the standing SAW and related pressure field along one dimension (x axis) of the device. Pressure nodes can be moved simply by altering the applied signal frequency. The node displacement (Δx_n) for a frequency change from f_1 to f_2 is described by $\Delta x_n = n(\lambda_1 - \lambda_2)/2 = n(c/f_1 - c/f_2)/2$ [7].

Even though acoustic tweezers based standing waves have many advantages on optical tweezers, like higher forces, broad range size of particle manipulation, and less heat that can prevent killing biological tissues and cells, it has many limitations as well. The selectivity is one of these limitations. A particle can't be selected and manipulated among others. A second limitation is that a 3D trap can be only achieved by using either multiple transducers or reflectors on the walls of the cavity.

1.3.2 Selective manipulation with acoustical vortices

In order to manipulate a particle independently of its neighbours (selective manipulation), the trap must be spatially localized near the particle. Using laterally (2D selective trapping) or radially (3D selective trapping) focused waves can achieve such localization. In acoustics in the LWR, particles which are less dense and more compressible than the surrounding liquid are attracted to the pressure anti-nodes of an acoustic standing wave field. While solid particles, cells, and most droplets (i.e. particles more dense and more stiff than the surrounding liquid), migrate toward the pressure nodes [34]. This type of particles are repelled from the focus of a focused wave. Thus, for trapping to occur, a pressure minimum is required at the trapping point surrounded by a high intensity ring. This can be achieved with acoustical vortices

Cylindrical acoustical vortices

Cylindrical acoustical vortices (Figure 1.10) are specific wave-fields that have been used for 2D particle trapping. Acoustical vortices are helical waves spinning around a phase singularity. Nye and Berry [67] were the first to introduce this class of waves, while studying wave phase singularities. On the central beam axis, the amplitude cancels due to the phase singularity and is surrounded by a bright ring that enables the lateral trapping and manipulation of particles [68]. Hefner and Marston [12] were the first to study and experimentally synthesize this kind of wave structures in acoustics.

Cylindrical vortices constitute a set of separated variable solutions; $\psi(r,\theta,z) = f(r)g(\theta)h(z)$ in cylindrical coordinates of the Helmholtz equation.

$$\frac{1}{r}\frac{\partial}{\partial r}(r\frac{\partial \Psi}{\partial r}) + \frac{1}{r^2}\frac{\partial^2 \Psi}{\partial \theta^2} + \frac{\partial^2 \Psi}{\partial z^2} + k^2\Psi = 0.$$

The solutions of this equation are given by [69]:

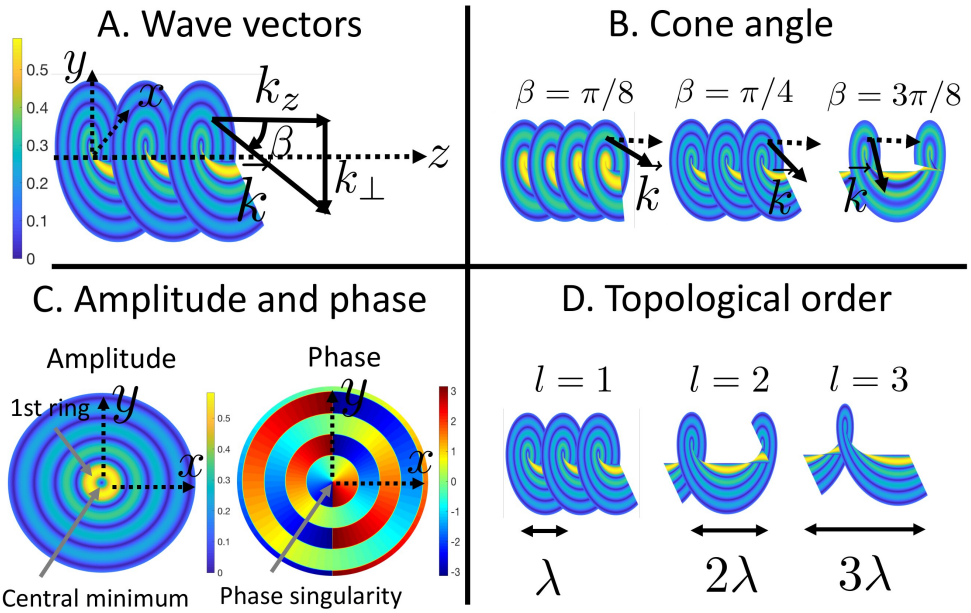

Figure 1.10: Bessel cylindrical vortices. A) Equiphase surface of a first order ($l = 1$) Bessel cylindrical vortex, having a cone angle $\beta = \pi/4$. The pressure amplitude is represented by the color field. k_z, $k_\perp$ and $k = k_z + k_\perp$ represent the axial component, the lateral component and the total wave vector. B) Equiphase surfaces for different cone angles ($\beta = \arctan k_\perp/k_z$) of a cylindrical vortex of topological order 1. C) The amplitude and the phase for the lateral evolution. D) Equiphase surfaces for different topological orders ($l = 1, l = 2$ and $l = 3$) of Bessel cylindrical vortices. Taken from [69].

$$\psi(r, \theta, z, t) = AJ_l(k_\perp r) \exp[i(l\theta + k_z z - \omega t)], \tag{1.7}$$

with A the amplitude of the vortex , J_l the cylindrical Bessel function of the first kind of order l (topological charge). $k_\perp$ is defined as $\sqrt{k^2 - k_z^2}$, where k is the wave number and k_z is the projection of k over the propagation axis z. The three parameters: topological order l, angular frequency ω, cone angle $\beta = \arccos(k_z/k)$ define the beam. The cone angle defines the angle between the propagation axis z and the wave vector k. Figure 1.10 shows as visual representation of the different parameters. For $l = 0$, the wave-field is no longer a vortex but a laterally focalized wave (which exhibits a pressure maximum in $r = 0$) since the field becomes invariant over θ and the lateral evolution is given by $J_0(kr)$. Only beams with topological order $|l| > 1$, represent vortices. For such orders, the Bessel functions exhibit a minimum amplitude at the center ($r = 0$) and then oscillate inside a decreasing envelope that evolves as $1/\sqrt{r}$. These waves, with a lateral evolution given by the Bessel function, are stationary over r and propagative over θ and z. The properties of these waves are good for lateral particle trapping. The wave-field exhibit a minimum in $r = 0$ and then increases to reach a maximum on the ring surrounding the central axis, which creates a gradient trap that keeps the particle at the center. Even though, cylindrical vortices are interesting for lateral particle trapping, they don't enable the particle trapping and hence manipulation in the z-direction [70, 71, 42, 72].

Spherical acoustical vortices

Baresch et al. [11] were the first to propose a way to obtain a 3D localized trap using spherical vortices (Figure 1.11A). Spherical vortices are the spherical analogs of cylindrical acoustical vortices. These wavefields are a set of orthogonal separate-variable solutions of the Helmholtz equation, but in spherical coordinates (r, θ, φ). These fields focalize the energy in three dimensions while maintaining a minimum at the focal point:

$$\psi(r, \theta, \varphi, t) = Aj_1(kr)P_l^m(\cos\theta) \exp[(i(m\varphi - \omega t)]. \tag{1.8}$$

The spherical Bessel function of the first kind of order $l \in Z$ is noted by $j_1(kr)$, and the associated Legendre polynomial of order$(1, m)$ is represented by P_l^m, where m is the topological charge ($-l \leq m \leq l$). For $m = 0$, the field is invariant over φ and the field becomes a focused wave. Thus, for $(m, l) = (0, 0)$ the wave-field is a spherically focused wave. For a topological

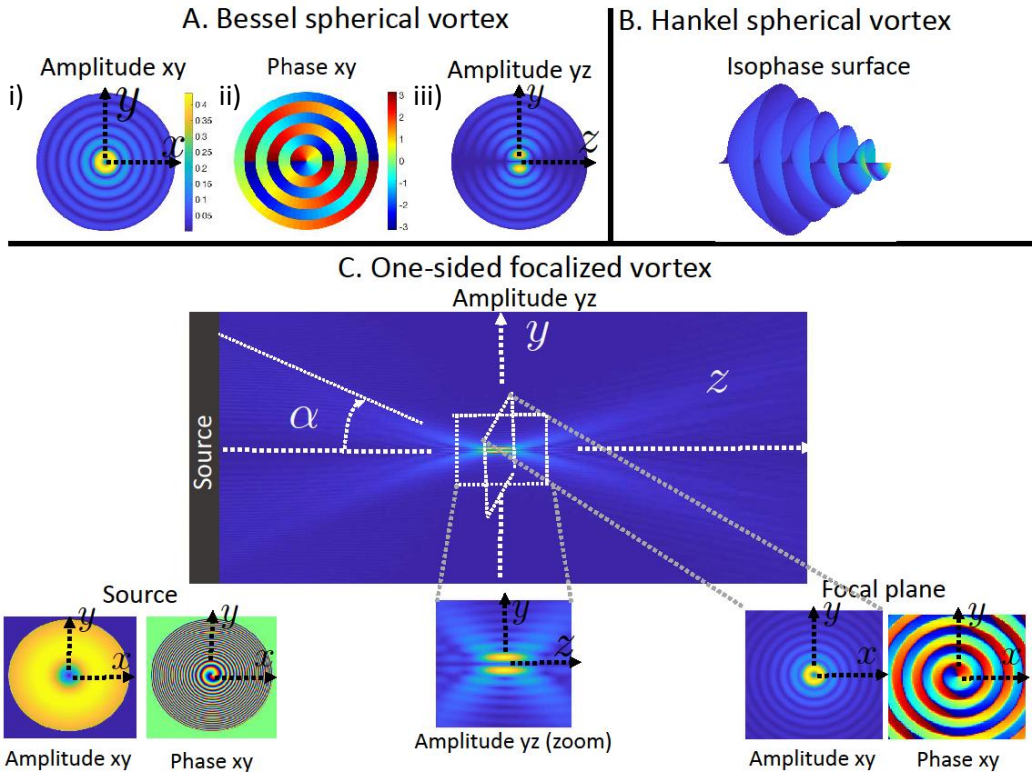

Figure 1.11: Bessel spherical focused vortices of topological order $(l, m) = (1, 1)$. A) Bessel spherical vortex amplitude and phase. B) Converging Hankel vortex. C) One-sided focused vortex amplitude and phase, noting that α corresponds to the aperture of the source. The focalization of the vortex is shown in the amplitude in the (x, y) plane; in the source plane (lower left) and the in the focal plane (lower right) the amplitude and the phase are also shown. Taken from [69].

order $|m| \geq 1$, the wave is referred as a spherical vortex. Figure 1.11A sub-panel i, shows a good framework for $3D$ trapping due to the spherical bright shell that surrounds the central phase singularity. Note that the phase is spinning around the z-axis (Figure 1.11A sub-panel ii). Figure 1.11A sub-panel iii, shows the amplitude of the vortex in the (y,z) plane. Figure 1.11C presents one sided spherical vortices. Similar to how two counter-propagating progressive waves can form plane standing waves, the interference between a converging and a diverging Hankel spherical vortices form a Bessel spherical vortex [69]:

$$Aj_1(kr)P_l^m(\cos\theta)\exp[(i(m\varphi-\omega t)] = \frac{A}{2}[b_l^{(1)}(kr)+b_l^{(2)}(kr)]P_l^m(\cos\theta)\exp[i(m\varphi-\omega t)],$$

where $b_l^{(1)}$ and $b_l^{(2)}$ are the Hankel functions of the first and second kind corresponding to the converging and diverging parts respectively.

One-sided spherical vortex synthesized from a control disk is represented in Figure 1.11C. With this wave-field a standing gradient trap in the z-direction (Figure 1.11C sub-panel ii) is produced by the interference between the converging Hankel vortex and the diverging Hankel vortex at the focal point. But the particle is also pushed away from the center in the direction of the wave propagation (along the z-axis) since the signal is generated from only one side. Hence, 3D trapping is possible only if the gradient restoring force overcomes the pushing force exerted by the propagative part of the wave. Moreover, an additional factor can contribute to push the particle away from the center of the trap, namely the acoustic streaming. As mentioned before, the first to demonstrate the ability of these vortex beams to trap particles was Baresch theoretically [11] and experimentally [4]. In addition, for a given array of transducers with phase control, Marzo [73] has shown that acoustical vortices are optimal wave-fields for 3D particle trapping in the LWR.

1.4 Thesis content

This thesis is composed of 6 chapters:

• Chapter 1 summarizes some relevant bibliography and key concepts related to the different types of contactless manipulation techniques, acoustofluidics and non-linear acoustics are introduced.

• Chapter 2 details the method used for the fabrication of holographic acoustical tweezers based on spiralling InterDigitated transducers (S-IDT).

• Chapter 3 introduces a new numerical method combining finite element simulation of the source and angular spectrum propagation of the wavefield to simulate the field produced by S-IDTs. This code is used in Chapter 3 to investigate two different designs to create a 3D trap.

• Chapter 4 demonstrates the selective manipulation of cells with single-beam acoustical tweezers. In particular, precise positioning of individual cells among a collection in a standard microscopy environment is shown with no impact on the viability of the manipulated cells.

• In Chapter 5, 250 MHz acoustical vortex are synthesized with spiraling interdigitated transducers. Spatially selective manipulation of 4μm silica particles using this ultra high frequency acoustical tweezer with high spatial selectivity and NanoNewton forces is demonstrated.

• Finally Chapter 6 discusses the ability to change the location of the acoustical trap axially of a one sided miniaturized acoustical tweezers by changing the driving frequency i.e. the ability to manipulate particles in three dimensions, by tuning the excitation frequency using this type of tweezers.

Chapter 2

Method: Fabrication process

Abstract

Designing miniaturized acoustical tweezers that are able to perform complex operations in a standard microscopy environment is a challenging task. In this chapter, we review the main steps, that were used by our team to design and fabricate holographic acoustical tweezers based on spiralling InterDigitated (S-IDT) Transducers.

2.1 Some definitions

Before introducing the tweezers fabrication recipe, let's introduce some definitions that will be used all along this chapter.

Niobate lithium

Lithium niobate ($LiNbO_3$) consists of niobium, lithium, and oxygen. It is a non-naturally-occurring salt. Its single crystals are an important material for mobile phones, optical wave-guides, optical modulators, piezoelectric sensors and various other linear and non-linear optical applications [74]. Figure 2.1 shows a 3 inches lithium niobate wafer Y cut 36^o of 0.5 mm thickness which are used in this thesis for all tweezers fabrication.

Figure 2.1: Niobate lithium wafer.

Lithium niobate is insoluble in water and it is a colorless solid. It has a trigonal crystal system, which lacks inversion symmetry. This crystalline structure gives lithium niobate certain properties: it is piezoelectric, photoelastic, electro-optical, pyroelectric, and ferroelectric [75].

• Piezoelectricity:
Piezoelectricity reflects the fact that a mechanical stress applied to a crystal creates a polarization in it, and hence an induced electric field and vice versa. The induced polarization varies linearly with the applied mechanical stress and is characterized by the creation of a potential difference between the faces of the crystal. This is the property of the Niobate Lithium that we used in our work.

• The photo-elastic effect:
It results in the fact that the refractive index of a medium is modified under the effect of an external force.

• The electro-optical effect:
It causes a change in the refractive index of a material when it is exposed to an electric field.

• Pyroelectricity:
It has a non-zero spontaneous polarization which varies with temperature. The variation in polarization is reversible over time when the temperature returns to its initial level.

• Ferroelectricity:
Ferroelectricity reflects the fact that it has a spontaneous electric polarization that can be reversed by the application of an external electric field. This polarization is naturally present in the material.

Lithium Niobate was used in this work owing to (i) its good piezoelectric coupling coefficient, (ii) its ability to generate high frequency vibrations and (iii) its transparency necessary for integrating acoustical tweezers in a microscope.

Photo-lithography

Photo-lithography is one of the most standard procedures used in microfabrication. It is also called UV lithography or optical lithography. In this process, UV light is used to transfer a geometric pattern from an optical mask to a light-sensitive photo-resist on the substrate. After that, a chemical treatment is done using a developer to etch the exposed patterns into the material or to enable the deposition of a new material in the desired pattern. Photo-lithography can create extremely small patterns and it has a high precision to control the shape and the size of the objects. It requires extremely clean operating conditions, that can only be achieved in clean rooms.

The main steps are the following. (i) A photo-resist is spread over the flat surface of a substrate using spin-coating. A photo-resist is a light-sensitive material that is used to protect some parts of the underlying substrate. This resist is generally spread using spin coating method: small amounts of a

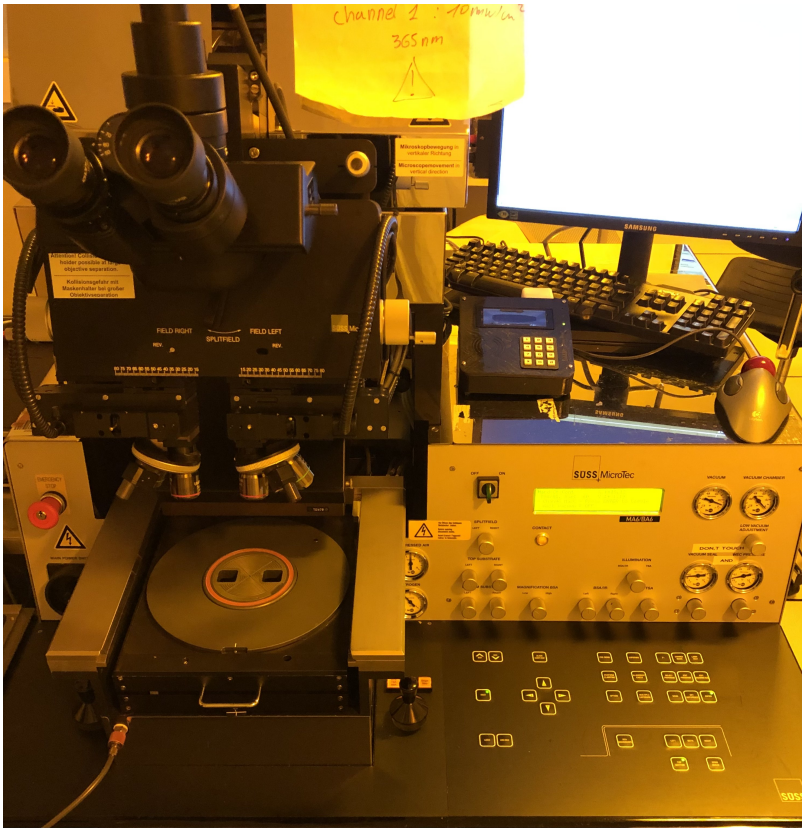

Figure 2.2: Photo-lithography equipment.

photo-resist are pipetted at the middle of the substrate which is then rotated using a spin coater (see Figure 2.3). The coating material is spread by centrifugal force, with a thickness of the film that depends both on the viscosity of the fluid and on the rotation speed [76]. Note that several authors studied the theoretical analysis of spin coating. The rate of spreading in spin coating was studied by Wilson et al. [77]. A universal description to predict the deposited film thickness was found by Danglad-Flores et al. [78]

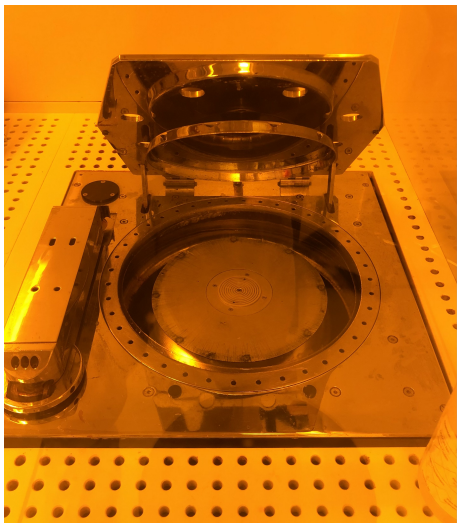

Figure 2.3: Spin coater.

(ii) A patterned mask is put on top of the resist with a mask aligner (see Figure 2.2). This mask protects some part of the resist from light. (iii) The photo-resist layer covered with the mask is exposed to UV light. Depending on the nature of the resist (positive or negative), either the exposed or the unexposed regions of the coating will be removed (check Figure 2.4). Indeed, positive photo-resist are degraded when exposed to light, which leads to dissolution of the exposed resist once plunged into the developer. Hence, only the unexposed portion of the coating remains on the covered surface. For negative photo-resists, the light strengthens the photosensitive material (either cross-linked or polymerized). Hence, only the regions that were not exposed to light will be dissolved by the developer. (iv) The substrate is placed in the developer to reveal the patterns.

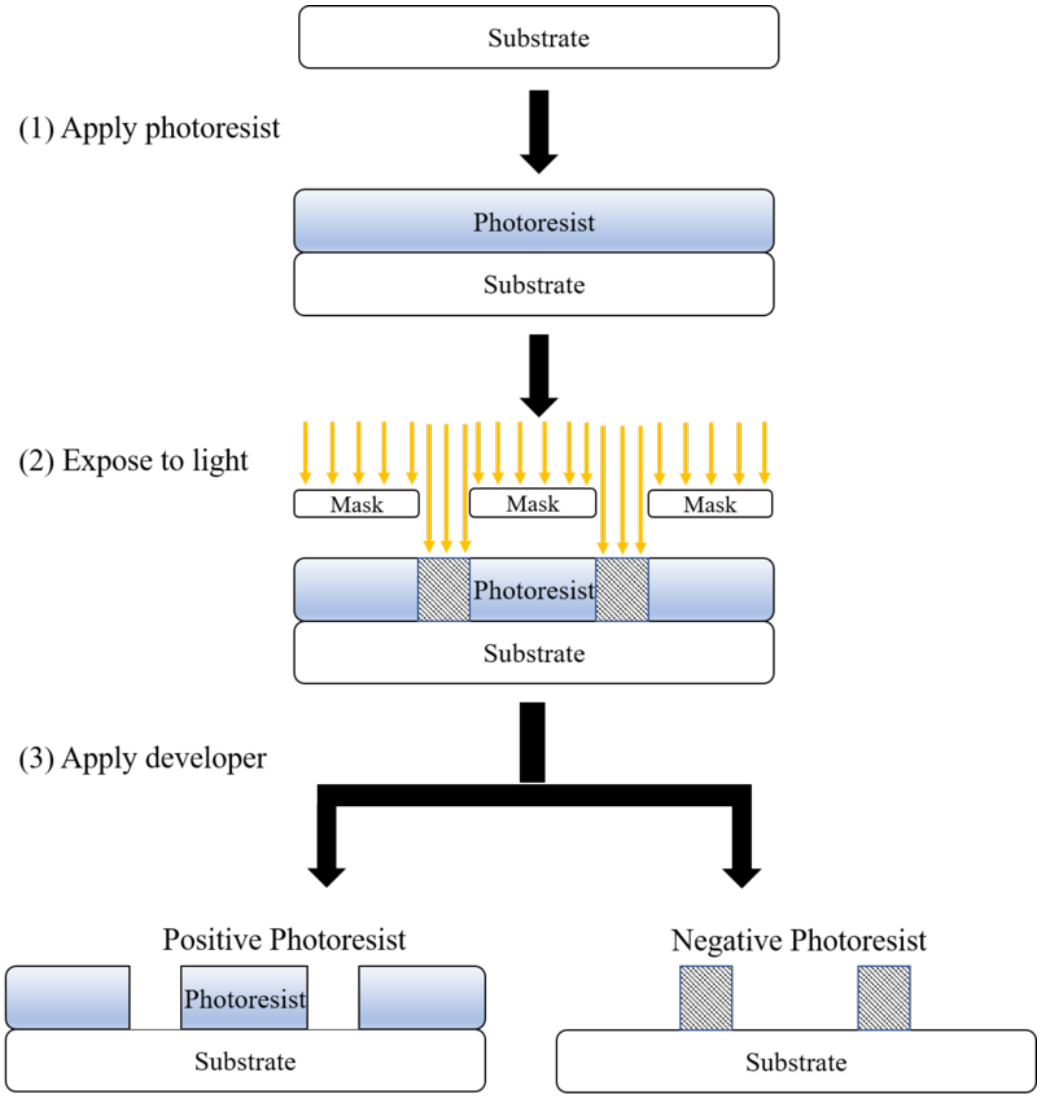

Figure 2.4: Photo-resist after Photo-lithography. This figure was taken from [79].

2.2 Active holographic tweezers based on Spiralling Interdigitated Transducers

As discussed in the introduction, selective 3D manipulation of micro-particles require the synthesis of specific wave-fields called acoustical vortices. The first cylindrical acoustical vortex were synthesized by Hefner and Marston in 1999 [80]. Since then, many techniques have been developed to synthesize cylindrical and focused (spherical) acoustical vortices: (i) active techniques based on arrays of bulk [81, 82, 83, 84, 85, 86, 87] or surface acoustic wave transducers [88, 89, 90], (ii) passive techniques based on helicoidal sources [80], photo-acoustics [91], phase engineered surfaces [92, 93, 94, 95], metamaterials [96], space coiled paths [97], delay lines [98] and diffraction gratings [99, 100, 101, 102].

But all these techniques are strongly limited in the activation frequency and hence the dimension of the acoustical vortex, that they can produce. Yet, reducing the spatial dimensions of the acoustical vortex is mandatory to extend the capabilities of acoustical tweezers to smaller and smaller particles with increased selectivity and trapping forces, since these two last parameters strongly rely on the size of the vortex compared to the size of the particle [103]. Indeed, the vortex ring is repulsive for surrounding particles. Hence high selectivity can only be achieved when the vortex ring has a size close to the particle size. And since the force applied on the particle depends on the gradient of the acoustic field, strong forces on small objects can only be obtained at high frequencies.

In 2017, Riaud et al. [104] proposed to use active holograms based on spiraling interdigitated transducers (S-IDTs) to synthesize cylindrical and then focused acoustical vortices [105]. Indeed, it is well known that classical interdigitated transducers can be used to synthesize surface acoustic waves (see e.g. [106] for acoustofluidics applications). But the possibilities offered by IDTs to generate more complex wave-fields remained mostly unexplored. The idea to generate a focused vortex with IDTs (see Figure 2.5) is (i) to take the intersection of the vortex wave-field with a plane, (ii) discretize the phase over two levels and (iii) materialize the equiphase lines with electrodes. We thus obtain a set of two intertwined spiraling electrodes of inverse polarity, whose polar equations (electrodes center-line) are given by:

$$\rho_1 = \frac{1}{k}\sqrt{(\theta + C_2)^2 - (kz)^2}, \tag{2.1}$$

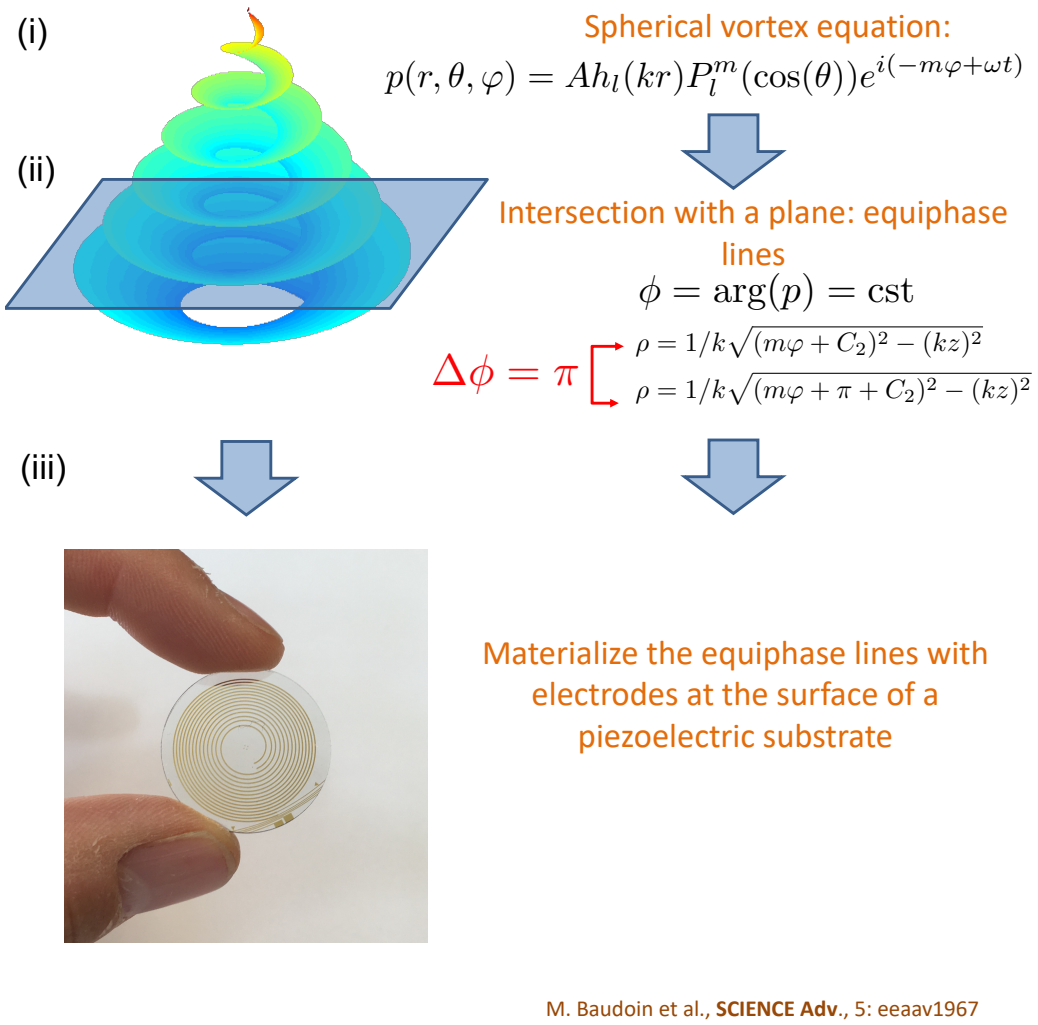

Figure 2.5: Scheme illustrating how S-IDT are designed. In this figure p is the pressure of the wave-field, (r, θ, φ) are the spherical coordinates, (ρ, θ, z) the cylindrical coordinates, h_l is the spherical Hankel function of order k, P_l^m is the associated Legendre polynomial, t is the time, ω the angular frequency, ϕ is the phase of the wave-field, m is the topological order of the vortex.

$$\rho_2 = \frac{1}{k}\sqrt{(\theta + C_2 + \pi)^2 - (kz)^2}, \tag{2.2}$$

with (ρ, θ, z) the cylindrical coordinates (the subscripts 1 and 2 stand for the electrodes 1 and 2), $k = \omega/c_o$ the wave-number, $\omega = 2\pi f$ the angular frequency, f the driving frequency of the system, c_o the sound speed in the focusing medium. The width of the electrodes equally distributed on both sides of the center-line defined by Equations (2.1) and (2.2) is kept equal to half the distance between the two electrodes. The distance between the two electrodes decreases with the radius to ensure focalization, similarly to the principle of Fresnel lenses.

This type of holograms is called active hologram. Indeed, contrarily to classic holograms that are enlightened with an external source, the electrodes on top of the piezoelectric substrate directly produce the sound field.

2.3 Tweezer fabrication

The acoustical tweezers used in this PhD are made of spiralling IDTs sputtered at the surface of a lithium niobate piezoelectric substrate, covered with a glued glass wafer used to focus the wave before reaching the microfluidic chamber where the operations are performed. Figure 2.6 shows an example of a set of acoustical tweezers. To fabricate them, several steps must be performed:

- Standard Photo-lithography.
- Fabrication of the spiral metallic electrodes.
- Report of target on glass wafer.

2.3.1 Standard Photo-lithography

Here is the standard procedure used for the fabrication: (i) $LiNbO_3$ piezoelectric substrate are cleaned for 3 minutes in acetone and propanol each, using an ultrasonic machine and dried with nitrogen gas. (ii) Moving towards the photo-resist spin coating process, the niobate lithium substrate is coated with HMDS which is an adhesion promoter and then with a negative AZnLof2020 photo-resist (see Figure 2.7). The protocol for the spin coating is 800(rpm) /300(m/s^2) /10(seconds) and then 2000(rpm)/1000(m/s^2)/30(s). Using this protocol, the desired thickness of the photo-resist is 2.9μm. After

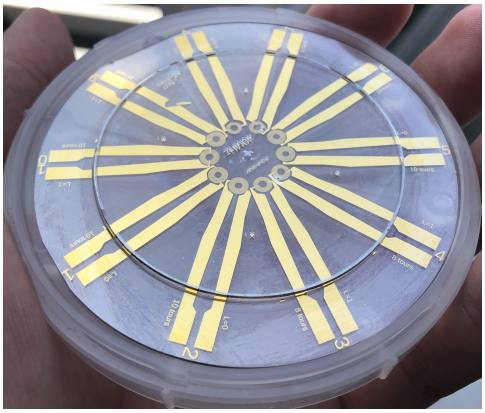

Figure 2.6: An example of a fabricated tweezers of 40MHz.

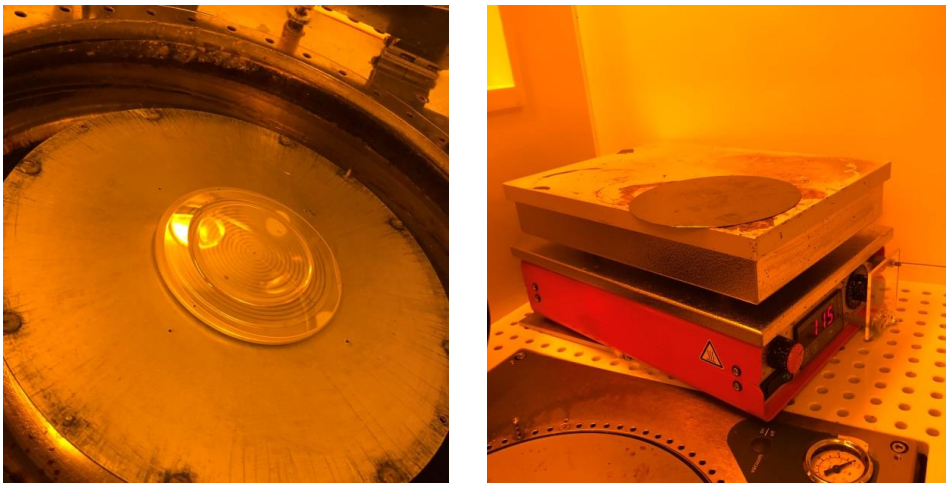

Figure 2.7: The left image shows a Niobate lithium wafer coated with AZnLof2020 photo-resist before spin coating process. The right image shows the hot plate that has been used to cure the resist.

the spin coating process, the niobate wafer is put on a hot plate at 110°C in order to remove the solvent in the photo-resist (First 30 seconds with only 1 point contact and then 90 seconds full contact, to prevent any thermal shock). In this step silicon (Si) substrate was used to elevate the wafer during curing since the wafer is extremely sensitive to temperature fluctuations (Figure 2.7).
The next step is to print the desired shape of an optical mask on the niobate wafer using photo-lithography. The spiraling electrodes are designed using a Matlab code and then imported in Layout Editor software where the lead electrodes are added. Figure 2.8 shows the design of a specific mask using Layout Editor software and the high precision corresponding optical mask fabricated in the clean room of IEMN using e-beam lithography. The mask

Figure 2.8: The left image represents the design for the transducers using layout editor software. The right image presents the optical mask of the design.

has to be aligned with the wafer. After alignment, The wafer is exposed to the UV light, using the parameters that are presented in Table 2.1.

The wafer has to be baked another time after exposure for 120 seconds at 110°C in order to finish the cross-linking process (make a strong bond between the exposed parts so that these parts will stay after placing the wafer in the developer). After baking the wafer, the latter is placed in AZ326 developer for 25 seconds and rinsed with de-ionized water and dried with nitrogen gas. Thus, the unexposed parts will be gone and the only parts resting are the exposed parts. This step is followed by an oxygen plasma treatment using Bati 5 machine to clean the wafer at 150W for 10 seconds.

Contact type	Hard contact
Gap	$300\mu m$
UV light	365nm
Time	3.6 s
Power	10 mW/cm^2

Table 2.1: Parameters for Photo-lithography.

2.3.2 Fabrication of the spiral metallic electrodes

Once the resist mask is fabricated, the electrodes are deposited over the substrate with the following process. (i) Metalization: After the oxygen plasma treatment, the whole niobate wafer is coated with a 40 nm titanium layer and a 400nm gold layer, using evaporation process. (ii) Lift-off procedure: The wafer is put in a SVC14 or AR300-76 solution and placed on a hotplate at 100°C for 2 hours. This solution helps to remove all the photo-resist remaining. A pipette is helpful in the lift off step. After making sure that all the unnecessary parts are removed and the only remaining parts are the electrodes (Figure 2.9), the wafer is rinsed with propanol and dried with nitrogen gas.

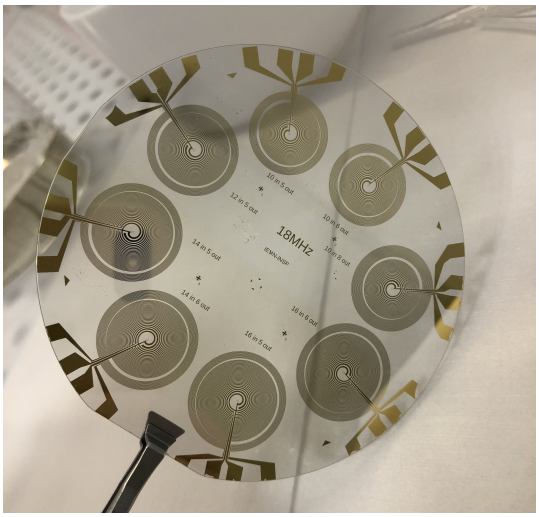

Figure 2.9: Lift off and formation of spiral metallic electrodes.

2.3.3 Glass wafer gluing and report of the markers.

For 2D applications in microfluidic chambers, a glass wafer is glued on top of the substrate to ensure the vortex focalization before the wave reaches the microfluidic chamber. Indeed, these chambers are thin (typically a few wavelength). Hence it is not possible to focus the wave in this fluid thin layer and focalization must be achieved before the microfluidic chamber. To ensure the focalization, we hence glued a glass wafer of thickness either 6.5 mm or 1.1 mm (depending on the activation frequency) with epoxy glue (Epotek 301-2) with the following process: (i) The glass wafer is cleaned with acetone and propanol and dried with nitrogen gas. The surface of the wafer is coated with

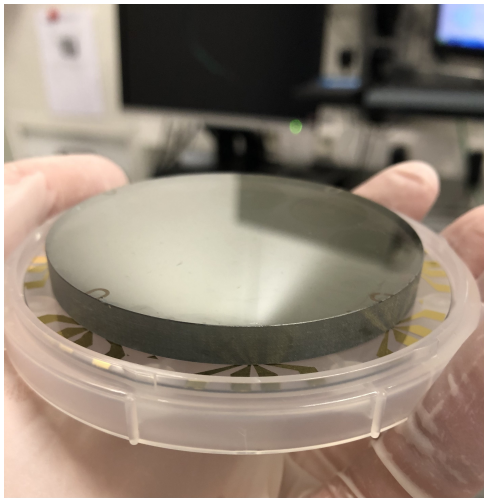

Figure 2.10: Glass wafer glued on the top of the niobate wafer.

a 15nm chromium layer using evaporation process (see Figure 2.10), that will be used later on to report markers localizing the center of the vortex. (ii) The glue is obtained by mixing two components (for 5 g of glue, 1.75 g of curing agent is needed) and leaving it in a vacuum bow (Figure 2.11) to remove all the bubbles from the mixture. (iii) In the meantime, both the niobate and the glass wafer are treated with oxygen plasma using bati PICO machine to make the two surfaces hydrophilic, using power of 100W, pressure of 1mbar, and for 60s. (iv) After removing the gas from the glue, a drop of 3.45 ml (calculated to obtain a 1μm layer of glue) is placed on top of the niobate wafer. The glass wafer is then positioned on top of the glue (see Figure 2.10) and capillarity enables to spread the glue over the whole wafer. Finally, the whole system is placed on horizontal plane (Marble plate) and left for two days to dry. After two days, the substrate is cleaned with Acetone for three seconds followed by propanol and dried with nitrogen gas.

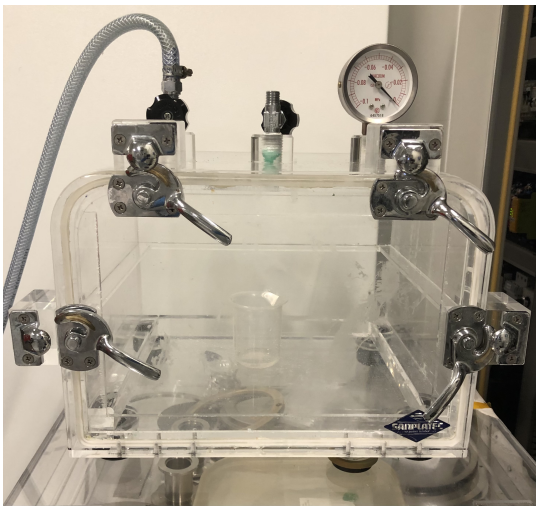

Figure 2.11: Vacuum box.

After gluing the glass wafer, it is necessary to create some markers on top of it to localize the center of the vortex. Thus, the following steps are used to report the center of the vortex (marked at the top of the niobate wafer) to the top of the glass wafer by patterning the chromium layer deposited earlier: photo-resist spin coating, baking, alignment and developing. Starting with the spin coating on the glass, the photo-resist used is AZ1505 which is a positive resist. The protocol for the spin coating is 500(rpm) /300(m/s^2) /6(seconds) and 2000(rpm)/1000(m/s^2)/20(s). Using this protocol, the desired thickness of the photo-resist is about 0.5μm. After the spin coating process, the substrate was put on a hot plate at 110°C in order to remove the solvent in the photo-resist (first 30 seconds with only 1 point contact and then 90 seconds full contact, to prevent any thermal shock). Again, Si substrate was used to elevate the wafer during curing since the wafer is extremely sensitive to temperature fluctuations as mentioned before. After spin coating and baking, it's time to print the marks on the top of the glass wafer using backside alignment photo-lithography. The mask has to be aligned with the wafer. After aligning the marks of the niobate wafer with the ones on the mask, the wafer is exposed to the UV light, using the parameters shown in Table 2.1. After exposure, the substrate is immersed in MIF726 developer for 25 seconds and then rinsed with de-ionized water. In this step, all the exposed parts during photo-lithography, are removed using this developer since the photo-resist used was a positive one. Then, it is immersed again in chromium etchant solution for about 20 seconds and rinsed with de-ionized water, in order to remove the chromium layer, except the parts where the

photo-resist stays (unexposed parts). The last step is to remove the resist on the top of the chromium by acetone, followed by propanol and dried with nitrogen gas. Finally, using all these steps, the tweezer is fabricated (Figure 2.12).

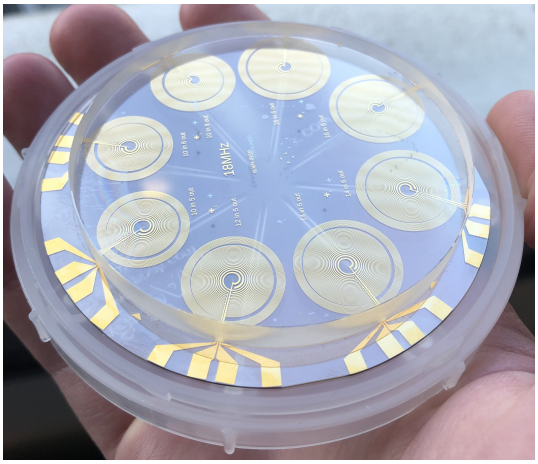

Figure 2.12: Acoustical tweezer.

2.4 Micro-channel fabrication

Micro-channels are commonly used in all 2D manipulations experiments in this thesis. These micro-channels, wherein the particles/cells are dispersed, are acoustically coupled with the transducer with a drop of silicone oil.

They are mainly made of a glass slide glued to a Plexiglas frame and covered with a PDMS micro-channel. The Plexiglas frame is used to enable precise mechanical displacement of the PDMS micro-channel compared to the transducer.

To fabricate them, several steps must be performed:

- Mould fabrication.
- Micro-channel preparation.
- Frame fabrication.
- Glass slide preparation.

2.4.1 Mould fabrication

Silicon wafer is used to fabricate the mould. The wafer is cleaned using piranha solution which is a mix of 5ml of H_2SO_4 sulfuric acid and 1ml of H_2O_2 hydrogen peroxide for 10-15 minutes. The wafer was washed with 2 baths of de-ionized water and dried with nitrogen gas.

As usual after cleaning the wafer the next step is going to be spin coating followed by photo-lithography to print the desired shape needed on it. For spin coating, the photo-resist used is SU8-2035 which is a negative resist. The protocol for the spin coating is 800(rpm) /1000(m/s^2) /10(seconds) and 2250(rpm)/1000(m/s^2)/30(s). Using this protocol, the desired thickness of the photo-resist is about 45μm. After the spin coating process, the substrate was put on a hot plate in order to dry the photo-resist at 65°C for 3 minutes and at 95°C for 6 minutes.

After baking, to print the desired shape of an optical mask on the silicon wafer, photo-lithography is needed. The mask has to be aligned with the wafer. After alignment, The wafer is exposed to the UV light, using the parameters presented in Table 2.2.

Contact type	Hard contact
Gap	300μm
UV light	365nm
Time	20 s
Power	10 mW/cm^2

Table 2.2: Parameters for Photo-lithography to fabricate the mould.

The wafer has to be baked another time after exposure at 65°C for 2 minutes and at 95°C for 6 minutes in order to make a strong bond between the exposed parts (unmasked parts) so that these parts will stay after placing the wafer in the developer. After baking, the wafer is placed in SU8 developer for 5 minutes and rinsed with propanol and dried with nitrogen gas.

2.4.2 Micro-channel preparation

The first step to prepare the PDMS is to mix the polymer with it's curing agent (for each 10g of polymer, 1g of curing agent is needed). The mixture is put in the vacuum box until no bubbles are seen. The silicon wafer that has been prepared before, is put in a three inches glass petri-dish. The PDMS is poured over the wafer. The petri-dish is put in the oven on 110^{o}C for 10 minutes. When the PDMS becomes solid and cooled down, the PDMS is cut and peeled. Inlets and outlets are created using a hole punch if needed.

2.4.3 Frame fabrication

The design of the frame is made using Inkscape software (Figure 2.13) and by using TROTEC LASER system, plexy glass of 4mm thickness is cut having the same shape of the design. The protocol of the laser cutting for 4mm

Figure 2.13: Design of the frame to be cut.

plexy glass is represented in Table 2.3

protocol	Cut	Etch
Power	70%	100%
Speed	0.25%	12%
Pulse	8500Hz	500PPI

Table 2.3: Parameters for laser cutting.

2.4.4 Glass slide preparation

Glass slides are cleaned with acetone and propanol, and dried with nitrogen gas. Next step is to glue the plexy glass frame with the glass slide using

NOA61 glue, and they are further exposed to UV light for one minute to dry the glue. Finally, the piece of the PDMS is put on the top of the glass slide (Figure 2.14).

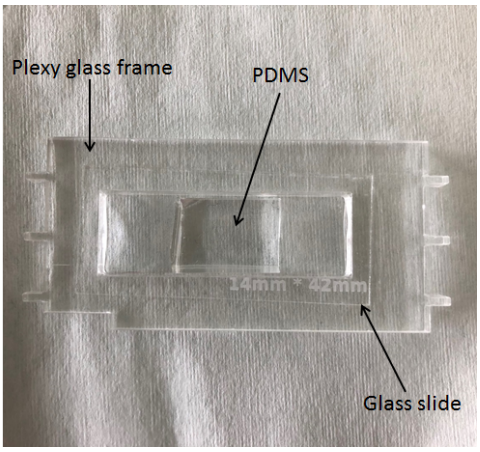

Figure 2.14: Microchannel.

2.5 Conclusion

For each project conducted in this PhD thesis, specific acoustical tweezers with optimized designs have been fabricated. For the first project, where the objective is to trap and manipulate selectively breast cancer cells in a microfluidic chamber, 40MHz acoustical tweezers with focalization at the bottom of the microfluidic chamber were fabricated. For the second project, where the objective is to manipulate micron sized particles with high selectivity and NanoNewton forces, higher frequency tweezers (250 MHz) have been designed. For the third and the last project, we designed some tweezers with the ability to trap and manipulate particles in 3D in a free environment (water tank).

Fabrication process needs a lot of time and efficiency. Any variation in any of its steps might lead to dis-function. This is why we give in this chapter the detailed recipes to fabricate the tweezers.

Chapter 3

Tweezers simulation

Abstract

In this chapter, we introduce a mixed Finite Element (FEM) / Angular Spectrum (AS) numerical method, which enables to compute the field produced by tweezers based on inter-twinned spiralling electrodes with reasonable computation time. This method is used in Chapter 5 to compute the acoustic field produced by ultra-high frequency acoustical tweezers. In this chapter, we use this numerical code to compare the ability of two different setups to produce a 3D focused acoustical vortex with the good properties for 3D particle trapping: a first system wherein the wave produced by the electrodes is radiated first inside a glass slide and then in water and a second system wherein the wave is radiated directly in water. The numerical results show that the first design enables to obtain higher amplitudes at same injected electrical power. This design will also result in weaker acoustic streaming, since no acoustic streaming is produced during the propagation in the solid. But this device also produces some spurious waves that affect the quality of the focalization of the vortex. The second design enables to produce a vortex of less intensity but of better quality to produce a 3D trap. We hence selected this second system to design 3D tweezers in Chapter 6.

3.1 Introduction

In the literature, most simulations of the field produced by spiraling interdigitated transducers were performed with an angular spectrum (AS) method [13, 14]. This method enables to compute the field in a target plane, knowing the field in the source plane, by decomposing it into a sum of plane waves (with spatial Fourier transform) and propagating each plane wave from the source to the target plane. But in these simulations, (i) the source is not simulated and is approximated by a binary acoustic source, with two spirals oscillating in phase opposition and (ii) the effects of the transmission through media with different acoustic properties on the amplitude of the wave were not considered. On the other hand, the full 3D direct numerical simulation of these multiphysics systems (piezoelectric synthesis + acoustic propagation) with a Finite Element (FEM) code would be prohibitive since the dimensions of the transducer and the propagation distance are huge compared to the wavelength which constitutes the characteristic length of the mesh. In this work, we introduce a mixed method which combines the direct simulation of the source with a FEM method, with an AS propagation of the source field to the target plane, and takes into account precisely the transmission at each interface.

The source consisting of the spiral-shaped metal electrodes deposited at the interface between $LiNbO_3$ and glass is simulated using a commercial finite element software (COMSOL Multiphysics). The electrodes are considered to be infinitely thin and are represented in the numerical model as surface conditions for the electric potential. In order to limit the size of the finite element simulation, Convolutional Perfectly Matched Layers (C-PML) are used to absorb the waves leaving the computational domain in all directions (except the backside of the piezoelectric wafer). Finite element simulation allows us to calculate the three components of the displacement in the glass at one wavelength of the interface between $LiNbO_3$ and the glass, when a excitation potential is applied to one of the two electrodes, the other being grounded.

The displacement obtained by finite element simulation is then decomposed into, on the one hand, a shear wave whose displacement component is in the plane perpendicular to the solid/fluid interface, called shear horizontal (SH), and to a shear vertical wave (SV) and a longitudinal wave on the other hand. The SH wave is not transmitted to water (considered as an ideal fluid), and thus not considered further. The SV and longitudinal waves are then propagated to the interface between the glass layer and the water using the angular spectrum technique. They are then multiplied by the solid/fluid transmission coefficients of each and added to obtain the pressure in the fluid

at the interface between the glass layer and the water. The pressure in water is finally propagated using also the angular spectrum technique.

3.2 Finite elements simulation

3.2.1 Introduction

Numerical solutions of Partial Differential Equations (PDE) for wave propagation require the truncation of an unbounded media to fit into computers with a limited memory and computation time. For such problems, an Absorbing Boundary Condition (ABC) is needed at the truncated boundary to eliminate the reflections from this boundary to the computational domain. Many kinds of ABCs have been found, for example, the ABCs of Clayton and Engquist [107], Peng and Toksoz [108] and Mur [109], etc. These ABCs, although successful in many fields, provide only limited absorption to waves within a limited range of incidence angles and limited frequencies [110].

In 1994, an implementation of Perfectly Matched Layer (PML) media [111] has introduced by Berenger for electromagnetic waves. Since then, it has been proven to be one of the most robust and efficient technique for the termination of unbounded domain [112]. In addition to be useful for electromagnetism simulation [113, 114], it was demonstrated to be very efficient for acoustic [115, 116] and elastic waves in isotropic [117, 118] and anisotropic solids [119]. It has been proven that theoretically, before discretization, at the interface between a computational medium and a perfectly matched medium no reflection occurs, and the incident waves from the computational medium are completely absorbed, regardless of their incidence angle and frequency [111, 117]. Nevertheless, this property is lost when a discretization is needed for numerical implementation, especially in the case of oblique incidence. One then needs to optimise the PML parameters in order to decrease parasitic reflections [120, 121].

Convolution Perfectly Matched Layer (C-PML), first presented in electromagnetism by Roden and Gedney [122], and applied in the simulation of elastic wave propagation [123, 124, 125, 126], has been shown to improve the behaviour of the discrete PML for grazing angles encountered in the case of surface waves. The main advantage of C-PML over the classical PML layer is that it is based on the un-split components of the wave field, and lead to a more stable scheme. Moreover, it is highly effective at absorbing signals of long time-signature [127], surface waves [126] or in elongated domains

of calculation [125]. Classically, C-PML has been introduced in first-order formulation of both electromagnetism and elastodynamic. We extend here the C-PML absorbing layer to the second-order system describing elastic waves in displacement formulation in piezoelectric solids, as it was done for classical split PML [128]. In frequency domain, this technique is easy to implement in commercial software based on Finite Element Method (FEM). The simulations are realized with the commercially available software Comsol Multiphysics. In some anisotropic media, numerical instabilities appear in the CPML [129], limiting the use of this absorbing layer. In order to stabilize the absorbing layer, another PML has been proposed by Meza-Fajardo et al. [130] and referred to as the "Multiaxial Perfectly Matched Layer" ("MPML"). Only few works are available in the literature on the use of PML for elastic wave propagation in piezoelectric solids. Split field PML, as the one introduced by Berenger [111], has been first derived for angular spectrum [131] and FDTD [132] methods. In both papers, instabilities appear in the PML for some of the presented simulations. This problem will be addressed here in more detail. Here, we propose to improve these first formulations by using unsplit C-PML in stead of split PML.

3.2.2 Wave Equations for Piezoelectric Solid

For a piezoelectric medium, the equations of motion, the Hooke's law and the Maxwell equations in the quasi-static approximation are given in the frequency domain by:

$$-\rho\omega^2 u_i = \frac{\partial T_{ij}}{\partial x_j}, \tag{3.1}$$

$$T_{ij} = C_{ijkl}\frac{\partial u_l}{\partial x_k} + e_{ijk}\frac{\partial \phi}{\partial x_k}, \tag{3.2}$$

$$\frac{\partial D_i}{\partial x_i} = 0, \tag{3.3}$$

$$D_i = \epsilon_{ij}\frac{\partial \phi}{\partial x_j} + e_{ijk}\frac{\partial u_j}{\partial x_k}, \tag{3.4}$$

where ρ is the density, ω is the pulsation, u_i are the components of the displacement vector, x_i are the components of the position vector ($x_1 = x, x_2 = y$, and $x_3 = z$), T_{ij} are the components of the stress tensor, D_i the components of the electric displacement vector (in), C_{ijkl} the components of the elastic constants tensor, e_{ijk} the components of the piezoelectric constants tensor, and ϵ_{ij} the components of the dielectric permitivity tensor.

3.2.3 Formulation of C-PML in Frequency Domain

Here, the methodology used for the introduction of C-PML zones for axisymmetric active solid media [123], is used for the system of Eqs. 3.1-3.4. First, taking the Fourier transform of the system, it is rewritten in the frequency domain. Then, the following complex coordinate's transformation [133] is used:

$$\tilde{x_i} = \int_0^{x_i} s_i(x_i')dx_i', \tag{3.5}$$

Where s_i are the Complex Frequency Shifted (CFS) stretched-coordinate metrics proposed by Kuzuoglu and Mittra [134]

$$s_i(x_i) = k_i(x_i) + \frac{\sigma_i(x_i)}{\alpha_i(x_i) + j\omega}, \tag{3.6}$$

where α_i and σ_i are assumed to be positive and real, and k_i are real and ≥ 1. The σ_i and k_i are the so-called [112] attenuation factor used for the attenuation of propagating waves, and scaling factor used for the attenuation of evanescent waves, respectively. The choice of the optimum spatial variation of these variables has been discussed in the literature [120, 135]. The α_i are frequency-dependent terms that implement a Butterworth-type filter in the layer. Using the complex coordinate variables $\tilde{x}_i$ to replace x_i in Eqs. 3.1-3.4, and noting that $\frac{\partial}{\partial \tilde{x}_i} = \frac{1}{s_i}\frac{\partial}{\partial x_i}$, we obtain the following frequency-domain equations in Cartesian coordinates:

$$-\rho\omega^2 u_i = \frac{1}{s_j}\frac{\partial T_{ij}}{\partial x_j}, \tag{3.7}$$

$$T_{ij} = C_{ijkl}\frac{1}{s_k}\frac{\partial u_l}{\partial x_k} + e_{ijk}\frac{1}{s_k}\frac{\partial \phi}{\partial x_k}, \tag{3.8}$$

$$\frac{1}{s_i}\frac{\partial D_i}{\partial x_i} = 0, \tag{3.9}$$

$$D_i = \epsilon_{ij}\frac{1}{s_j}\frac{\partial \phi}{\partial x_j} + e_{ijk}\frac{1}{s_k}\frac{\partial u_j}{\partial x_k}, \tag{3.10}$$

In order to implement these C-PML in a commercial FEM software (COMSOL Multi-physics), the resulting second-order C-PML wave equations are interpreted as a fictitious anisotropic medium, as it has already been done for PML [136]. Multiplying Eqs. 3.7 by $s_1 s_2 s_3$ and introducing the new stress tensor T' and density ρ', we get the following equations:

$$-\rho'\omega^2 u_i = \frac{\partial T_{ij}'}{\partial x_j}, \tag{3.11}$$

$$T'_{ij} = C'_{ijkl}\frac{\partial u_l}{\partial x_k} + e'_{ijk}\frac{\partial \phi}{\partial x_k}, \tag{3.12}$$

$$\frac{\partial D'_i}{\partial x_i} = 0, \tag{3.13}$$

$$D'_i = \epsilon'_{ij}\frac{\partial \phi}{\partial x_j} + e'_{ijk}\frac{\partial u_j}{\partial x_k}, \tag{3.14}$$

where i, j, k, l = 1, 2 or 3. The effective elastic tensor C'_{ijkl}, piezoelectric strain matrix e'_{ijk}, permittivity matrix ϵ'_{ij} and density ρ' are given by:

$$C'_{ijkl} = C_{ijkl}\frac{s_1 s_2 s_3}{s_i s_k}, \tag{3.15}$$

$$e'_{ijk} = e_{ijk}\frac{s_1 s_2 s_3}{s_i s_k}, \tag{3.16}$$

$$\epsilon'_{ij} = \epsilon_{ij}\frac{s_1 s_2 s_3}{s_i s_k}, \tag{3.17}$$

$$\rho' = \rho s_1 s_2 s_3. \tag{3.18}$$

In the stretched-coordinate metrics, the following spatial coordinate dependencies are used for the parameters of the C-PML layers in the x_i direction:

$$k_i = 1 + k_{imax}\left(\frac{x_i - x_{i0}}{d_i}\right)^{n_1}, \tag{3.19}$$

$$\sigma_i = \sigma_{imax}\left(\frac{x_i - x_{i0}}{d_i}\right)^{n_1+n_2}, \tag{3.20}$$

$$\alpha_i = \alpha_{max}\left(\frac{d_i - x_i + x_{i0}}{d_i}\right)^{n_3}, \tag{3.21}$$

with $\alpha_{max} = 2\pi f_c$, where f_c is a low cut-off frequency and:

$$\sigma_{imax} = (1 + n_1 + n_2)\sqrt{\frac{C_{11}}{\rho}}\log\left(\frac{1}{R_0}\right)\frac{1}{2d_i}, \tag{3.22}$$

where R_0 is the theoretical desired reflection coefficient and x_{i0} and d_i are respectively the starting position and thickness of the C-PML layer in the x_i direction.

The introduction procedure of the stabilized absorbing boundary layer, the so-called “MPML”, is in all points similar to C-PML. However, in the “MPML”

the attenuation parameters σ_i' of the stretching parameter s_i are now a function of the three space variables x_i:

$$\sigma_i(x,y,z) = \sigma_i(x_1,x_2,x_3) = \sigma_i(x_i) + \sum_{j\neq i} p^{ij}\sigma_j(x_j), \tag{3.23}$$

where p^{ij} are stabilizing parameters that need to be determined. Using the method introduced for PML by Bécache et al. [129] , and Appelo and Kreiss [137] for C-PML, to analyse the stability of the "MPML" the following criteria has been obtained for the stability condition:

$$S_i V_{gi} + \sum_{j\neq i} p^{ij} S_i V_{gi} > 0, \tag{3.24}$$

where S_i are the components of the slowness vector and V_{gi} the ones of the group velocity.
Details of the calculations can be found in the PhD thesis of Yifeng Li [138]. In the simulations presented below for a Y-36 cut $LiNbO_3$ wafer, the following C-PML parameters in the stretched-coordinate metrics have been chosen: $f_c = f_0/3$ (where f_0 is the working frequency of the tweezer), $n_1 = 2$, $n_2 = 1$, $n_3 = 1$, $R_0 = 10^{-6}$, $k_{imax} = 3$, and $p^{ij} = 0.3$.

3.3 Angular spectrum simulations

3.3.1 Propagation in fluids

In the angular spectrum method, a plane wave decomposition of a source plane (x, y) is used [139, 140]:

$$s(x,y,z_0,\omega) = FT_{2D}^{-1}[S(k_x,k_y,z_0,\omega)], \tag{3.25}$$

where

$$S(k_x,k_y,z_0,\omega) = FT_{2D}[s(x,y,z_0,\omega)]. \tag{3.26}$$

Each plane mode corresponds to a plane wave propagating along the direction given by $\vec{k}(k_x,k_y,k_z)$ where the component k_z of the wave vector is given by:

$$k_z = \sqrt{k^2-\xi^2} \text{ if } \xi^2 \leq k^2, \tag{3.27}$$

for propagative waves, or

$$k_z = j\sqrt{\xi^2-k^2} \text{ if } \xi^2 > k^2, \tag{3.28}$$

for evanescent waves. Here $k = \frac{\omega}{c_f}$ is the wave-number, $\xi = \sqrt{k_x^2 + k_y^2}$ and c_f is the sound speed in the fluid.

The propagation operator for a distance $\Delta z = z - z_0$ is given by:

$$H(k_x, k_y, \Delta z, \omega) = e^{jk_z \Delta z}, \tag{3.29}$$

Therefore, we have:

$$S(k_x, k_y, z_0 + \Delta z, \omega) = S(k_x, k_y, z_0, \omega) H(k_x, k_y, \Delta z, \omega), \tag{3.30}$$

and

$$s(x, y, z_0 + \Delta z, \omega) = FT_{2D}^{-1}[S(k_x, k_y, z_0, \omega) H(k_x, k_y, \Delta z, \omega)], \tag{3.31}$$

The numerical implementation of the Eqs. 3.26 and 3.31 uses a Fast Fourier Transform (FFT) algorithm that performs a discrete version of the convolution between the source and the propagation operator, and can thus introduce a convolutional wraparound error. Thus, it has been shown that in the case where $\Delta k_x = \frac{2\pi}{X_{max}}$ and $\Delta k_y = \frac{2\pi}{Y_{max}}$ are smaller than $\Delta k_{x,ycrit} = \frac{\pi\sqrt{k^2 - \xi^2}}{2\Delta z k_{x,ymax}}$, ymax then the direct use of H$(k_x, k_y, \Delta z, \omega)$ no longer gives correct results [141, 142, 143]. In this case, it is better to use the following operator:

$$H(k_x, k_y, \Delta z, \omega) = FT_{2D}[h(x, y, \Delta z, \omega)], \tag{3.32}$$

where

$$h(x, y, \Delta z, \omega) = -\frac{\Delta z e^{jkR}}{2\pi R^2} \left(jk - \frac{1}{R} \right), \tag{3.33}$$

which is the response of a source point and $R = \sqrt{x^2 + y^2 + \Delta z^2}$.
So, we have two solutions for the implementation [143, 144]

-Frequency Sampled Convolution (FSC) algorithm: We sample the source and the transfer function in the frequency domain.

- Spatially Sampled Convolution (SSC) algorithm: We sample the source and the impulse response in the spatial domain.

The SSC algorithm by using a sufficiently small spatial discretization, directly sampling the spatial functions s(x, y, z_0, ω) and $h(x, y, \Delta z, \omega)$ and then transforming, multiplying the results, and inverse transforming the product, correctly implements the discrete, circular version of the Fourier convolution theorem. The FSC algorithm corresponds to a convolution between samples

of the source in the spatial domain and samples of the given $H(k_x, k_y, \Delta z, \omega)$ function in the spatial frequency domain. These samples of the H function correspond to samples of the infinite h function which has been infinitely wrapped around to produce a function of finite extend. It is as if instead of having a single source we had an infinite number of sources spaced at a distance equal to the size of the chosen calculation area. Thus, it is not surprising that large errors can appear in the output of the FSC algorithm. It is therefore preferable to use the SSC algorithm to simulate wave propagation in a homogeneous medium.
Moreover, it is preferable to do the calculation from the source (in z = 0) because it is the only plane in which $u(x, y, 0, \omega)$ or $p(x, y, 0, \omega)$ are of finite size. If we have a normal velocity source of finite size (especially if there is no apodization) then the pressure source given by $p(x, y, 0, \omega) = \rho c_f FT^{-1}[FT[u(x, y, 0, \omega)]\frac{k}{k_z}]$ can have infinite size and will be truncated during the discretization.
When we want to simulate a wave propagating from one medium to another (or in a stratified medium), it is necessary to propagate the wave to the interface, to take into account the transmission from one medium to another, and then to propagate it in the second medium. In this case, we must use a multi-step algorithm to propagate the wave. A point spread function h_m which would account for all propagation effects during a transmission through an interface or through multiple layers does not appear to be analytically derivable. Thus, updating the SSC approach to allow for taking into account interface appears to be very difficult. In this case, we must use the FSC algorithm which, as we have seen, has wraparound errors. To reduce these errors, it is possible to use angular restrictions, which applies a spatial low-pass filter to the spectral propagator function [142, 144, 145, 146], or to use an absorption layer [147] We have chosen the second method, which although it increases the computation time a bit, is much more efficient.
The transfer function H and the impulse response h correspond to the propagation from a pressure plane to a pressure plane. If we want to propagate the given source in normal velocity to a pressure plane, we must use the following functions for the FSC and SSC algorithms:

$$H_u(k_x, k_y, \Delta z, \omega) = \frac{\rho c_f k}{k_z} e^{jk_z \Delta z}, \tag{3.34}$$

$$h(x, y, \Delta z, \omega) = -j\rho c_f k \frac{e^{jkR}}{2\pi R}, \tag{3.35}$$

Up to now we have worked with the pressure or the particle velocity, but we can also work with the potential ϕ_f:

$$u = \nabla \phi_f, \tag{3.36}$$

and

$$p = -\rho \frac{\partial \phi_f}{\partial t}, \tag{3.37}$$

This will be useful when we study the transmission of a wave between a solid and a fluid. For the notation chosen here, $e^{-j\omega t}$, we have then:

$$u = jk_z \phi_f, \tag{3.38}$$

and

$$p = j\omega\rho\phi_f, \tag{3.39}$$

3.3.2 Propagation in isotropic solids

The angular spectrum method is extended now to the case of elastic wave propagation in a solid by following the method proposed by Vezzetti [148].

Angular spectrum in a solid

For a homogeneous solid, the equations of motion and Hooke's law give:

$$C_{ijkl} \frac{\partial^2 u_l}{\partial x_j \partial x_k} + \rho\omega^2 u_l = 0. \tag{3.40}$$

The solution is sought for a plane wave propagating along $\vec{k} = (k_x, k_y, k_z)$, where $k_z^2 = k^2(k_x, k_y, k_z) - k_x^2 - k_y^2$:

$$u_i(r,t) = u_i(r)e^{-j\omega t} = U_i e^{j(k_x x + k_y y + k_z z - \omega t)}. \tag{3.41}$$

We consider the propagation along $z > 0$. Thus, we have:

$$[C_{ijkl} k_j k_l - \rho\omega^2 \delta_{il}] U_l = 0, \tag{3.42}$$

or

$$[C_{ijkl} n_j n_l - \rho v^2 \delta_{il}] U_l = 0, \tag{3.43}$$

where $v = \frac{\omega}{k}$ is a velocity in m/s. Three solutions correspond to a propagation along $z > 0$: v_L, v_{FT} and v_{ST}. A non trivial solution exists if:

$$\det[C_{ijkl} k_j k_l - \rho\omega^2 \delta_{il}] = 0, \tag{3.44}$$

Introducing the Christoffel tensor $\Gamma_{il} = C_{ijkl}k_j k_l$ we have:

$$\det[\Gamma_{il} - \rho\omega^2\delta_{il}] = 0, \tag{3.45}$$

This corresponds to finding the roots of a polynomial of order 6 in $k_z(k_x, k_y, \omega)$:

$$\sum_0^6 \alpha_i k_z^i = 0, \tag{3.46}$$

The coefficients α_i are generally very difficult to express for an anisotropic material. Among the 6 solutions $k_z^{(i)}, i \in [1, 6]$, we have to select the 3 solutions which correspond to a propagation along z > 0 (the 3 others correspond to a propagation along z < 0). The coefficients being real, the solutions of k_z are either complex conjugate ($a + jb$ and $a - jb$) or inverse (a and $-a$) two by two. For the conjugated complex roots, we choose the one with a positive imaginary part because we are looking for a propagation following:

$$e^{j(k_z z - \omega t)} = e^{j((a+jb)z - \omega t)} = e^{j(az - \omega t)}e^{-bz}, \tag{3.47}$$

which tends well towards 0 when $z \to \infty$. For real roots things are more complicated because it is not necessarily the positive root which is the good one.
Let us suppose that we have found the 3 values of $k_z^{(i)}$, i = 1, 2 or 3 which respect our criterion of propagation following $z > 0$. For each of these eigenvalues $k_z^{(i)}$ we have an associated eigenvector $U^{(i)}$. The displacement field at a distance z from the source is then written as the sum of the angular spectra of the three eigenmodes:

$$\begin{aligned} u_l(x, y, z) &= \int_{-\infty}^{+\infty}\int_{-\infty}^{+\infty}\sum_{i=1}^{3}\beta^{(i)}U_l^{(i)}e^{j(k_x x + k_y y + k_z^{(i)})}dk_x dk_y \\ &= TF_{2D}^{-1}\left[\sum_{i=1}^{3}\beta^{(i)}U_l^{(i)}e^{jk_z^{(i)}}\right], \end{aligned} \tag{3.48}$$

We must therefore determine the respective amplitudes of the 3 eigenmodes $\beta^{(i)}$ from the initial conditions on the source (in $z = 0$). How to do it, will be explained now in the case of an isotropic solid.

Isotropic solids

When the solid is isotropic the solution of the Christoffel equation (3.45) can be obtained analytically, and is given by:

$$k_z^{(1,2)} = k_{zT} = \sqrt{k_T^2 - k_x^2 - k_y^2}, \tag{3.49}$$

where $k_T = \frac{\omega}{v_T}$ with $v_T = \sqrt{\frac{C_{44}}{\rho}}$ being the velocity of the transverse wave. Moreover, we have:

$$k_z^{(3)} = k_{zL} = \sqrt{k_L^2 - k_x^2 - k_y^2}, \tag{3.50}$$

where $k_L = \frac{\omega}{v_L}$ with $v_L = \sqrt{\frac{C_{11}}{\rho}}$ being the velocity of the longitudinal wave. If the displacement on the surface of the source is known (from a finite elements calculation as proposed here) then:

$$\hat{U}_j(k_x, k_y) = FT_{2D}[u_j(x, y, 0, \omega)] = \sum_{i=1}^{3} \beta^{(i)} U_j^{(i)}, \tag{3.51}$$

These equations can be rewritten in the following matrix form:

$$A \cdot (\beta) = \hat{U}, \tag{3.52}$$

Where

$$\hat{U} = \begin{pmatrix} \hat{U}_1 \\ \hat{U}_2 \\ \hat{U}_3 \end{pmatrix}, \tag{3.53}$$

and $A_{ij} = U_i^{(i)}$. The amplitude of the three eigenmodes are then given by $\beta = A^{-1}\hat{U}$.

For an isotropic solid, the choice of eigenvectors is not unique. In the Vezzetti paper [148], the author has chosen:

$$U^{(1)} = \frac{1}{\sqrt{k_T^2 - k_x^2}} \begin{pmatrix} 0 \\ -k_{zT} \\ k_y \end{pmatrix}, \tag{3.54}$$

$$U^{(2)} = \frac{1}{k_T\sqrt{k_T^2 - k_x^2}} \begin{pmatrix} k_T^2 - k_x^2 \\ -k_x k_y \\ -k_x k_{zT} \end{pmatrix}, \tag{3.55}$$

$$U^{(3)} = \frac{1}{k_L} \begin{pmatrix} k_x \\ k_y \\ k_{zL} \end{pmatrix}. \tag{3.56}$$

In the case we are interested in, where we consider propagation in a stratified medium perpendicular to the z-axis, it is preferable to use eigenvectors corresponding on the one hand to a transverse wave whose displacement component is in the (x, y) plane (SH wave), and on the other hand to a vertical transverse wave (SV) and a longitudinal wave:

$$\vec{u} = \vec{u'}_{SH} + \vec{u'}_{SV} + \vec{u'}_{L} \tag{3.57}$$

For this we consider at first that the projection of the wave vector in the (x, y) plane is oriented along the x direction only. In this case we have [149]:

$$\vec{u'}_{SH} = \nabla \times \vec{\psi}_{SH}, \tag{3.58}$$

$$\vec{u'}_{SV} = \nabla \times \vec{\psi}, \tag{3.59}$$

$$\vec{u'}_{L} = \nabla \phi, \tag{3.60}$$

where $\vec{\psi} = (0, \psi, 0)$ and $\vec{\psi}_{SH} = (0, 0, \psi_{SH})$. So we have:

$$\vec{u'}_{SH} = \begin{pmatrix} \frac{\partial}{\partial x'} \\ \frac{\partial}{\partial y'} \\ \frac{\partial}{\partial z} \end{pmatrix} \wedge \begin{pmatrix} 0 \\ 0 \\ \psi_{SH} \end{pmatrix} = \begin{pmatrix} 0 \\ -j\xi\psi_{SH} \\ 0 \end{pmatrix} \tag{3.61}$$

$$\vec{u'}_{SV} = \begin{pmatrix} \frac{\partial}{\partial x'} \\ \frac{\partial}{\partial y'} \\ \frac{\partial}{\partial z} \end{pmatrix} \wedge \begin{pmatrix} 0 \\ \psi \\ 0 \end{pmatrix} = \begin{pmatrix} -jk_{zT}\psi \\ 0 \\ j\xi\psi \end{pmatrix} \tag{3.62}$$

$$\vec{u'}_{L} = \begin{pmatrix} \frac{\partial \phi}{\partial x'} \\ \frac{\partial \phi}{\partial y'} \\ \frac{\partial \phi}{\partial z} \end{pmatrix} = \begin{pmatrix} j\xi\phi \\ 0 \\ jk_{zL}\phi \end{pmatrix} \tag{3.63}$$

The wave vector in the considered basis (x', y', z) is given by:

$$\vec{k'} = \begin{pmatrix} \xi \\ 0 \\ k_z \end{pmatrix}, \tag{3.64}$$

Now if we consider:

$$\vec{k} = \begin{pmatrix} k_x \\ k_y \\ k_z \end{pmatrix} = R_z(\Phi)\vec{k'}, \tag{3.65}$$

where $R_z(\Phi)$ is the rotation matrix of an angle Φ with respect to the x axis around z:

$$R_z(\Phi) = \begin{pmatrix} \cos\Phi & -\sin\Phi & 0 \\ \sin\Phi & \cos\Phi & 0 \\ 0 & 0 & 1 \end{pmatrix}, \tag{3.66}$$

then

$$\vec{k} = \begin{pmatrix} \xi\cos\Phi \\ \xi\sin\Phi \\ k_z \end{pmatrix}, \tag{3.67}$$

Thus in the new basis we have:

$$\vec{u}_{SH} = R_z(\Phi)\vec{u'}_{SH} = \begin{pmatrix} j\xi \sin\Phi\psi_{SH} \\ -j\xi\cos\Phi\psi_{SH} \\ 0 \end{pmatrix}, \tag{3.68}$$

$$\vec{u}_{SV} = R_z(\Phi)\vec{u'}_{SV} = \begin{pmatrix} -jk_{zT}\cos\Phi\psi \\ -jk_{zT}\sin\Phi\psi \\ j\xi\psi \end{pmatrix}, \tag{3.69}$$

$$\vec{u}_{L} = R_z(\Phi)\vec{u'}_{L} = \begin{pmatrix} j\xi\cos\Phi\phi \\ j\xi\sin\Phi\phi \\ jk_{zL}\phi \end{pmatrix}, \tag{3.70}$$

Remembering that $k_x = \xi\cos\Phi$ and $k_y = \xi\sin\Phi$, we obtain:

$$\vec{u}_{SH} = j\psi_{SH}\begin{pmatrix} k_y \\ -k_x \\ 0 \end{pmatrix}, \tag{3.71}$$

$$\vec{u}_{SV} = j\psi\begin{pmatrix} -k_{zT}\frac{k_x}{\xi} \\ -k_{zT}\frac{k_y}{\xi} \\ \xi \end{pmatrix}, \tag{3.72}$$

$$\vec{u}_{L} = j\phi\begin{pmatrix} k_x \\ k_y \\ k_{zL} \end{pmatrix}, \tag{3.73}$$

Finally, by normalizing these three vectors we arrive at the following basis of eigenvectors:

$$U^{(1)} = \frac{1}{\xi}\begin{pmatrix} k_y \\ -k_x \\ 0 \end{pmatrix}, \tag{3.74}$$

$$U^{(2)} = \frac{1}{k_T\xi}\begin{pmatrix} -k_{zT}k_x \\ -k_{zT}k_y \\ \xi^2 \end{pmatrix}, \tag{3.75}$$

$$U^{(3)} = \frac{1}{k_L}\begin{pmatrix} k_x \\ k_y \\ k_{zL} \end{pmatrix}, \tag{3.76}$$

and $\vec{u}_{SH} = j\xi\psi_{SH}U^{(1)}$, $\vec{u}_{SV} = jk_T\psi U^{(2)}$, and $\vec{u}_L = jk_L U^{(3)}$. Moreover, the three potentials ψ_{SH}, ψ, and ϕ in the plane $z_0 = \lambda T$ can then be calculated using:

$$\psi_{SH} = -j\beta^{(1)}\frac{k_y U_x^{(1)} - k_x U_y^{(1)}}{\xi^2}, \tag{3.77}$$

$$\psi = -j\frac{\beta^{(2)}U_z^{(2)}}{\xi}, \tag{3.78}$$

$$\phi = -j\frac{\beta^{(3)}U_z^{(3)}}{k_z L}, \tag{3.79}$$

Solid / Fluid interface

At the interface between a solid and a perfect fluid, the shear waves propagating in the solid with a displacement parallel to the interface (the SH waves of the previous paragraph are not transmitted in the fluid). We must therefore focus only on the transmission of transverse waves whose polarization is vertical (SV waves of the previous paragraph) and longitudinal waves. The transmission coefficients relating the potentials ϕ and ψ of the solid to the potential ϕ_f of the fluid are given by [149]:

$$\phi_f = \begin{bmatrix} \tilde{W}_{ll} & \tilde{W}_{tl} \end{bmatrix} \begin{bmatrix} \phi \\ \psi \end{bmatrix}, \tag{3.80}$$

with

$$\tilde{W}_{ll} = \frac{(1-\tilde{V}_{ll})}{\cos 2\theta_t}\tan\theta\cot\theta_l, \tag{3.81}$$

$$\tilde{W}_{tl} = \frac{(1+\tilde{V}_{tt})}{2\sin^2\theta_t}\tan\theta. \tag{3.82}$$

The pressure (in the spatial frequency domain) in the fluid just above the interface is then calculated by:

$$P = j\omega\rho(\tilde{W}_{ll}\phi + \tilde{W}_{tl}\psi). \tag{3.83}$$

3.4 Outline of the calculation procedure

In this chapter we simulate two systems that are envisioned to create a 3D acoustical trap:

- A first system based on spiraling electrodes wherein the field is first radiated (and partially focused) inside a glass plate and then finishes its focalization inside water. Note that this system is similar to the one used for 2D trapping in a microfluidic chamber in Chapters 3 and 4 but (i) a glass with low transverse wave speed is used to reduce impedance mismatch with water and (ii) focalization occurs inside water and not at the top of the glass slide.

- A second system wherein the wave is radiated directly in water.

The system with the glass plate had in theory several advantages: (i) The glass slide glued on top of the electrodes enables a more efficient synthesis of bulk waves. (ii) Since part of the focalization occurs in the glass plate before reaching the fluid, this system will produce less acoustic streaming, which can contribute to push the particle out of the trap in the axial direction. (iii) The glass slide isolate both electrically and thermally the electrodes from the fluid. This is why we investigated this system first experimentally. But experiments showed that with this system some spurious waves are also generated, which reduce the focalization of the energy. This is confirmed by the simulations presented in this chapter. This is why we investigated a second method wherein the electrodes are only protected with a thin SU8 layer to isolate them electrically, and the wave is directly radiated into water. As we will see in the next section, the 3D focused vortex has the expected properties for 3D trapping.

3.4.1 Tweezers with an intermediate glass plate

For the simulation of acoustic tweezers radiating in water through a glass layer, the calculation procedure can be summarized as follows:

- The interface between the piezoelectric wafer ($LiNbO_3$) and the glass on which the spiral-shaped electrodes are located (see Figure 3.1) is simulated by the finite element method. C-PMLs are placed on all six sides of the simulation domain, except on the bottom side of the piezoelectric wafer in the case where finite thickness is desired. The computational domain is meshed using tetrahedra whose size does not exceed half a wavelength of the transverse wave in the glass, as shown in Figure 3.2.
The equations (3.11)-(3.22) are solved using the PDE mode of COMSOL Multiphysics.
- The three components of the displacement, at one wavelength from the electrode in the glass layer, calculated using the COMSOL Multiphysics simulation (see Figure 3.3) are saved in a text file to be used as input for the simulation using the angular spectra method.
- A Fourier transform of the three components of the displacement is performed. The result is then projected on the basis of the SH, SV and L eigenmodes to obtain the $\beta^{(i)}$ amplitudes of each of these modes using the equations (3.52) and (3.74)-(3.76).
- The three potentials ψ_{SH}, ψ, and ϕ in the plane $z_0 = \lambda_T$ are then calculated using equations (3.77-3.79).

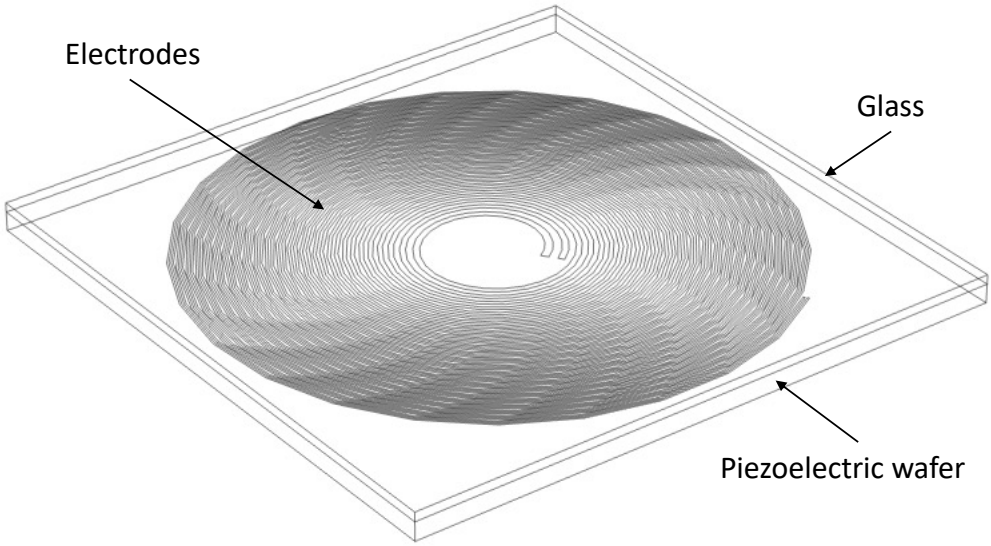

Figure 3.1: Finite element calculation domain comprising a piezoelectric wafer layer, a glass layer and the two spiral shaped electrodes placed on the interface between the two layers.

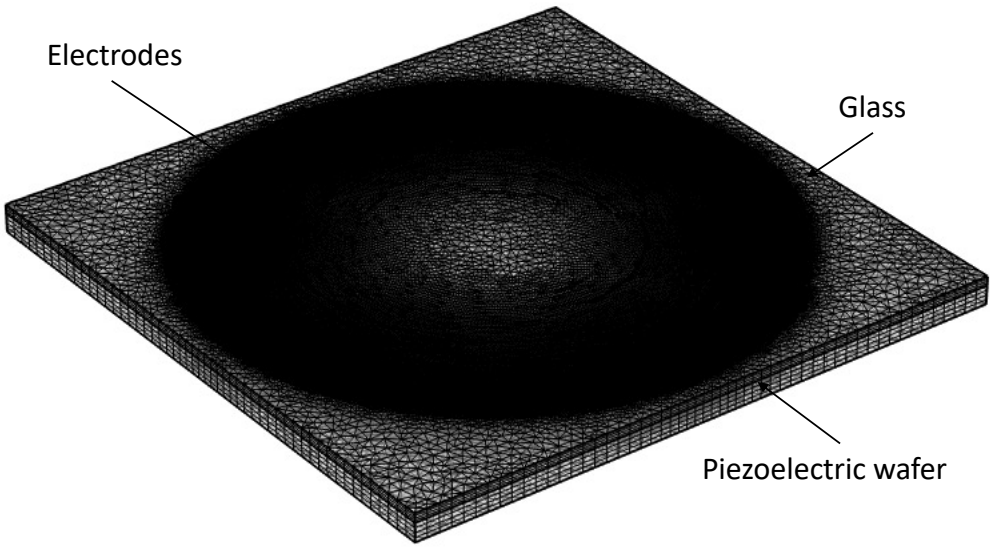

Figure 3.2: Meshing of the calculation domain.

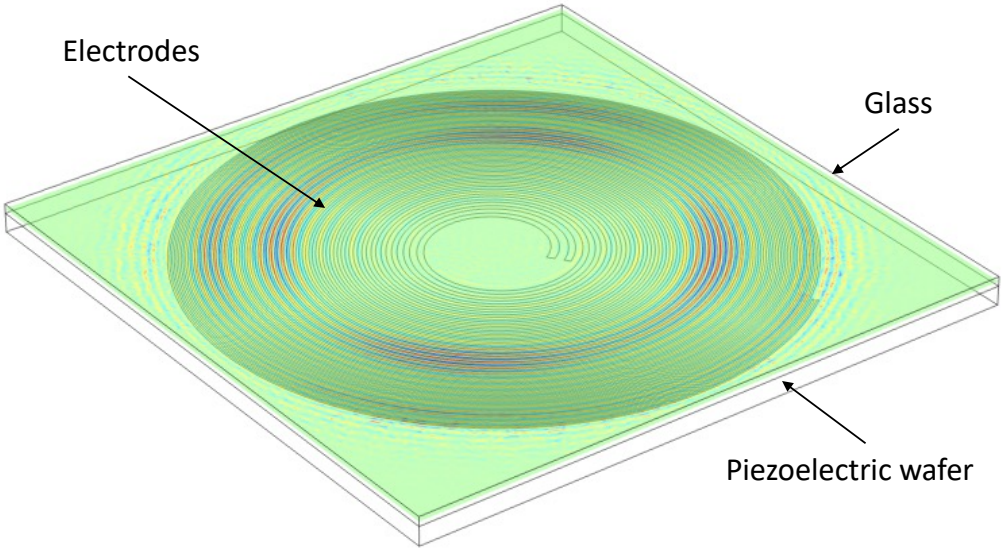

Figure 3.3: Component u_3 of the displacement (in nm), at one wavelength from the electrode in the glass layer, calculated using the COMSOL Multiphysics simulation.

- They are then propagated to the interface between glass and water by the angular spectrum method using an operator adapted to transverse waves for ψ_{SH} and ψ, and to longitudinal waves for ϕ. It is possible to return to the displacements by using the equations (3.71)-(3.73), summing the results obtained for each of the modes and performing an inverse Fourier transform to return to the spatial domain.
- The pressure (in the spatial frequency domain) in the fluid just above the interface is then calculated using equation (3.83). It is important to remember that only the components along z of the longitudinal and vertical transverse waves contribute to the pressure in the fluid. All the energy corresponding to the horizontal transverse waves is lost.
- The pressure is then propagated in water using the angular spectrum method. An inverse Fourier transform allows to return to the spatial domain.

3.4.2 Tweezers with direct emission into the fluid

For tweezers radiating directly into water without passing through a glass layer, the procedure is much simpler. The interface between the piezoelectric wafer ($LiNbO_3$) and the water in which the wave must focus, and which contains the spiral electrodes, is simulated by the finite element method. The pressure obtained in water at one wavelength from the interface is then

propagated by the angular spectrum method.

3.5 Simulations of 3D tweezers based on spiraling interdigitated transducers

3.5.1 Tweezers with a glass plate

Full simulation

The Low Frequency (LF) 3D device working at 5 MHz is simulated using the mixed method described in the previous paragraph. This device is made of a Y-36 cut $LiNbO_3$ wafer of 1 mm thickness on which are deposited two spiral shaped electrodes with 17 turns. A 6.5 mm low speed glass layer (Schott SF57HTUltra) is glued on the wafer. The electrodes are designed following the technique described in [13, 14], to focus in water, 2 mm above the glass surface (more precisely 8.5 mm above the electrodes considering the propagation of shear waves in glass).

Here, Convolutional Perfectly Matched Layers (C-PML) are used to absorb the waves leaving the FEM computational domain in all directions except below the 1 mm thickness $LiNbO_3$ wafer. The calculation domain is limited to 74 x 74 wavelengths in width. The thicknesses of $LiNbO_3$ and glass are respectively 1 mm and 2 wavelengths (of the shear wave in glass). The C-PMLs occupy 3 wavelengths on each side of the computational domain, except on the top surface of the glass where they are only one wavelength of thickness. The following properties are used in the simulations for the different materials:

- Water : Density $\rho = 1000\text{kg/m}^3$ and speed of sound $c_f = 1481\text{m/s}$.

- Glass : Density $\rho = 5510\text{kg/m}^3$, Young modulus E = 54GPa and Poisson ratio $\nu = 0.248$.

- Y-36 cut $LiNbO_3$: Density $\rho = 4700\text{kg/m}^3$,

Elastic stiffness tensor
$$\begin{bmatrix} 202.9 & 58.753 & 69.074 & -13.239 & 0 & 0 \\ 58.753 & 222.32 & 90.339 & -8.6765 & 0 & 0 \\ 69.074 & 90.339 & 192.79 & -7.6485 & 0 & 0 \\ -13.239 & -8.6765 & -7.6485 & 75.333 & 0 & 0 \\ 0 & 0 & 0 & 0 & 78.336 & 4.3932 \\ 0 & 0 & 0 & 0 & 4.3932 & 56.557 \end{bmatrix}$$

(GPa),

$$\text{Piezoelectric constant tensor e} = \begin{bmatrix} 0 & 0 & 0 & 0 & 0.11943 & -4.481 \\ -1.6482 & -2.2978 & 2.574 & 0.46692 & 0 & 0 \\ -1.9392 & -1.5917 & 4.5277 & -0.2593 & 0 & 0 \end{bmatrix},$$

$$\text{Relative dielectric permitivity tensor } \epsilon_r = \begin{bmatrix} 43.6590 & 0 & 0 \\ 0 & 34.1950 & 6.8760 \\ 0 & 6.8760 & 38.6635 \end{bmatrix}.$$

Finite element simulation allows us to calculate the three components of the displacement in the glass at one wavelength of the interface between $LiNbO_3$ and the glass, when a potential of 10V is applied to one of the two electrodes, the other being grounded. The obtained three components are displayed in Figure 3.4.

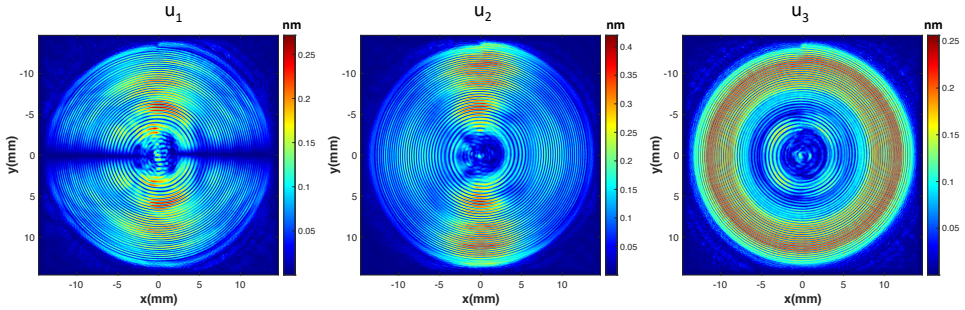

Figure 3.4: Components of the displacement (in nm), at one wavelength from the electrode in the glass layer, calculated using the COMSOL Multiphysics simulation of the LF 3D tweezers with a 1mm thickness wafer.

The displacements (amplitude and phase) calculated with COMSOL Multiphysics are used as a source in the angular spectra method described above. The components of the displacement obtained in the glass layer are displayed in Figure 3.5. Note that in these figures, the transducer are located at the top of the simulation window and radiating downward.

Most of the energy is focused well above the interface between the glass and water (6.5 mm from the electrodes), but a second focal point appears in the glass at about 4 mm from the electrodes. As we will see, this does not affect the quality of the focused vortex formed in water.

The pressure transmitted in the fluid is shown in Figure 3.6. It is clear that

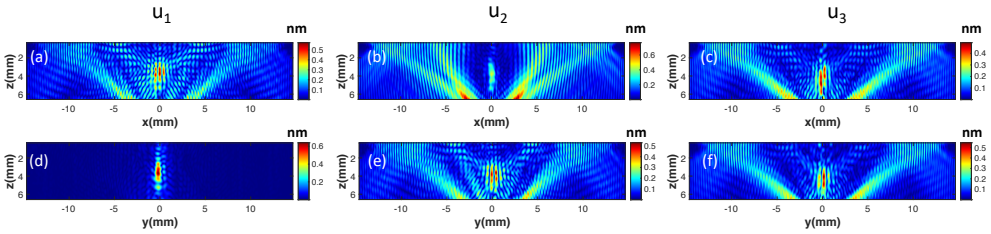

Figure 3.5: Components of the displacement (in nm) in the glass layer: u_1 (a) and (d), u_2 (b) and (e), u_3 (c) and (f), in the xz plane (a)-(c) and yz plane (d)-(f). The simulations were performed for the LF 3D tweezers with a 1 mm thickness wafer.

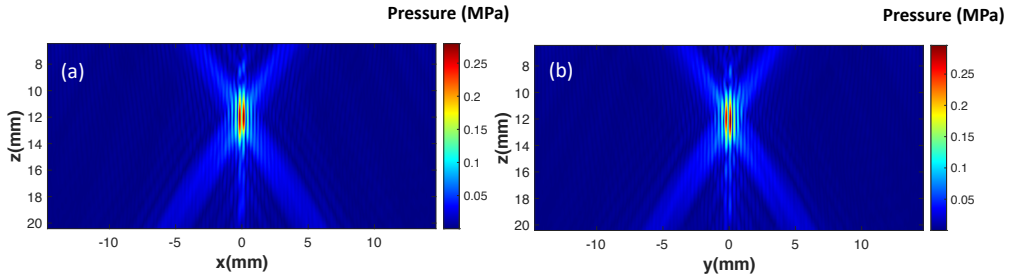

Figure 3.6: Pressure in the fluid (in MPa) in the xz plane (a) and yz plane (b) for the LF 3D tweezer with a 1 mm thickness wafer.

the wave focuses, but at about 12 mm from the electrodes. The increase of the focal length compared to the initial design comes from the refraction of the waves when passing from glass to water. This can easily be taken into account when designing the electrodes.

In the focal plane, at 12 mm from the electrodes, we find as expected a Bessel vortex of order 1, as shown in Figure 3.7.

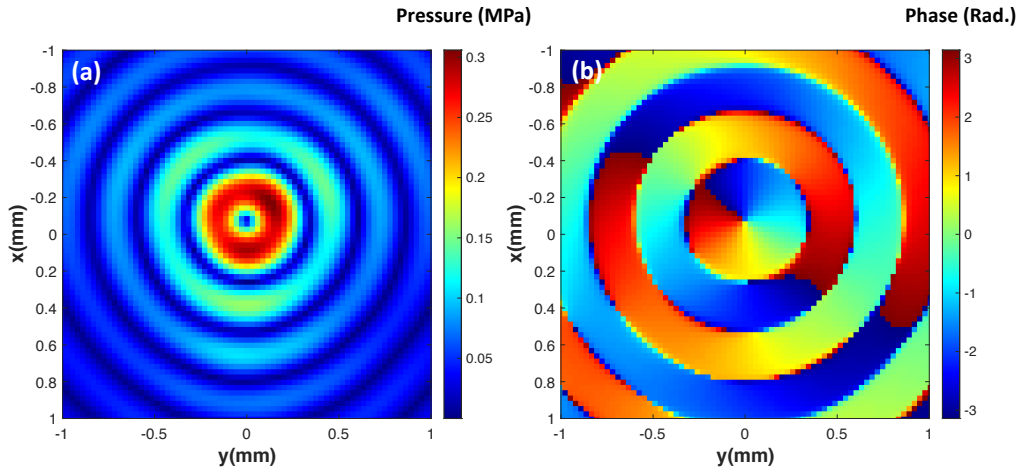

Figure 3.7: Pressure in the focal plane (12 mm above the electrodes) for the LF 3D tweezers with a 1 mm thickness wafer: (a) Amplitude (in MPa), (b) phase (in Radian).

However, the center of the vortex is slightly shifted due to the asymmetry of the electrodes. The amplitude of the first ring of the Bessel vortex is 0.3 MPa for an excitation of 10 V applied on the electrodes.

Respective contributions of Longitudinal and SV waves

In order to better understand the underlying physics of the tweezers synthesis, the simulation by the method of angular spectra is redone by considering separately the contributions of longitudinal waves and SV waves. For this purpose the amplitudes of the other modes ($\beta^{(i)}$) are set to zero when calculating the propagation in the glass. Thus, when we consider only the longitudinal wave, we have ($\beta^{(1)} = \beta^{(2)} = 0$). The component u_3 of the displacement in the glass layer and the pressure transmitted in the fluid are displayed in Figure 3.8.
In this case, only the focal point in the glass at about 4 mm from the electrodes is visible. The longitudinal waves emitted by the tweezers do not focus in water, and do not generate any vortex, as can be seen in Figure 3.9

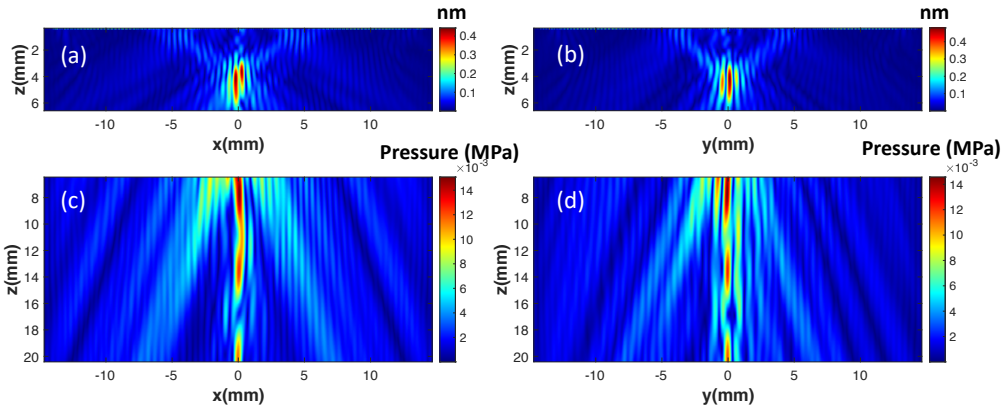

Figure 3.8: Component u_3 of the displacement (in nm) in the glass layer in the xz plane (a) and yz plane (b). Pressure in the fluid (in MPa) in the xz plane (c) and yz plane (d). The simulations were performed for the LF 3D tweezer with a 1 mm thickness wafer considering only the longitudinal waves contribution.

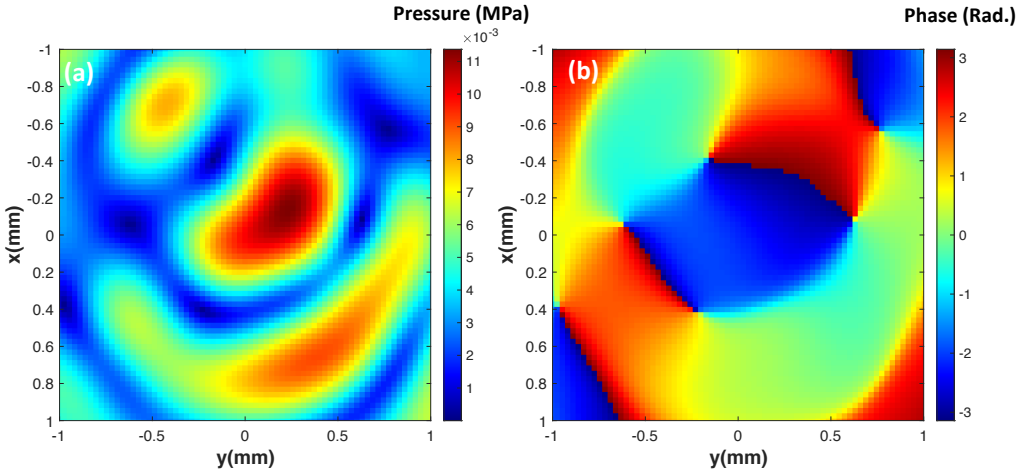

Figure 3.9: Pressure in the focal plane (12 mm above the electrodes) for the LF 3D tweezers with a 1 mm thickness wafer considering only the longitudinal waves contribution: (a) Amplitude (in MPa), (b) phase (in Radian).

displaying the pressure in the focal plane at 12 mm above the electrodes.
If we now perform the calculation considering only the SV waves, we find the vortex in water but without the second focal point in the glass, as shown in Figures 3.10 and 3.11.

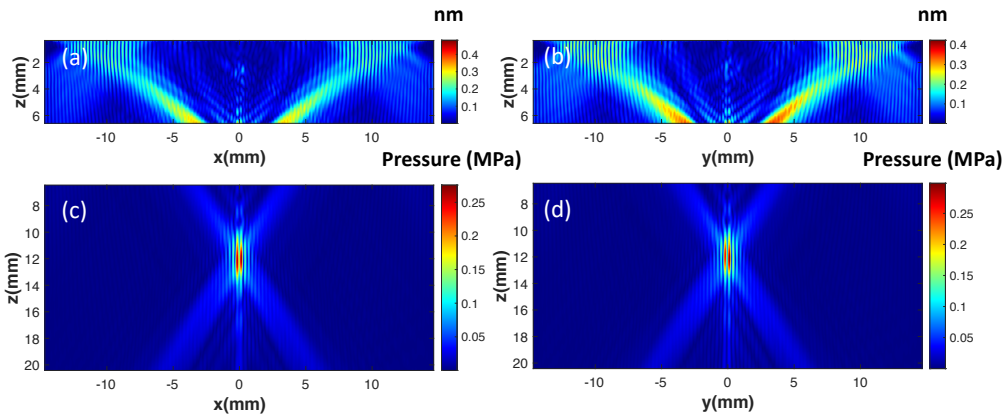

Figure 3.10: Component u_3 of the displacement (in nm) in the glass layer in the xz plane (a) and yz plane (b). Pressure in the fluid (in MPa) in the xz plane (c) and yz plane (d). The simulations were performed for the LF 3D tweezer with a 1 mm thickness wafer considering only the transverse waves contribution.

This is normal, as the design of the electrodes was made to focus the shear waves in the glass. The simulations show that, although part of the energy is used to generate longitudinal and SH waves, these do not disturb the formation of the focused vortex. We can however note the presence of a low amplitude parasitic wave propagating along the z axis (see Figure 3.10).

Influence of the finiteness of the piezoelectric wafer

One hypothesis of the origin of the parasitic wave are the finiteness of the substrate. Indeed the thickness of the wafer (1 mm) is comparable to the wavelength of transverse waves in glass (about 0.4 mm), and even smaller than the wavelength of longitudinal waves in $LiNbO_3$ (about 1.3 mm) at the considered frequency. So this could create some spurious waves.
To test this hypothesis, some simulations were performed in which the piezoelectric wafer is assumed to be of infinite thickness by adding some Convolutional Perfectly Matched Layers (C-PML) on the back side of the piezoelectric substrate. The components of the displacement obtained at one wavelength from the electrode in the glass layer using the COMSOL Multiphysics are displayed in Figure 3.12.

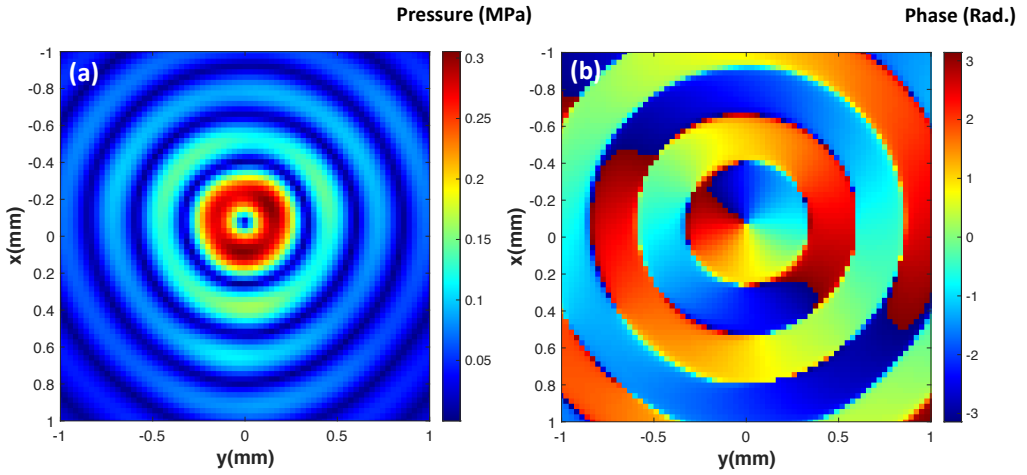

Figure 3.11: Pressure in the focal plane (12 mm above the electrodes) for the LF 3D tweezers with a 1 mm thickness wafer considering only the transverse waves contribution: (a) Amplitude (in MPa), (b) phase (in Radian).

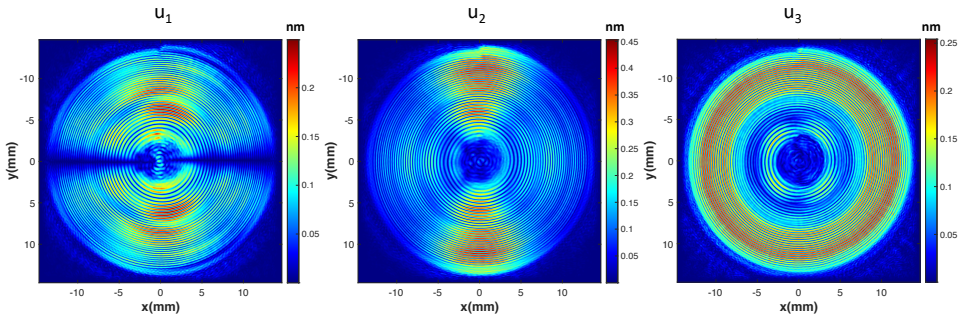

Figure 3.12: Components of the displacement (in nm), at one wavelength from the electrode in the glass layer, calculated using the COMSOL Multiphysics simulation of the LF 3D tweezers with an infinite thickness wafer.

The calculated components of the displacement in the glass layer and the pressure transmitted in the fluid are really very similar to those obtained by considering a wafer thickness of 1 mm, as shown in Figures 3.13 and 3.14.

The vortex obtained in the focal plane, at 12 mm from the electrodes, is still of good quality and is slightly shifted (see Figure 3.15). The thickness of the wafer does not seem to play an important role in the operation of the tweezers, at least when it is designed to focus transverse waves.

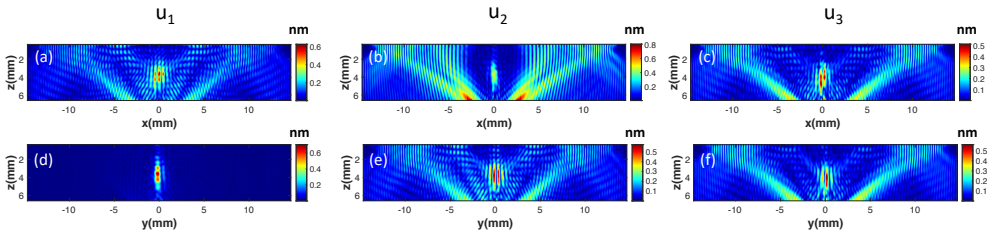

Figure 3.13: Components of the displacement (in nm) in the glass layer for the LF 3D tweezers with an infinite thickness wafer: u_1 (a) and (d), u_2 (b) and (e), u_3 (c) and (f), in the xz plane (a)-(c) and yz plane (d)-(f).

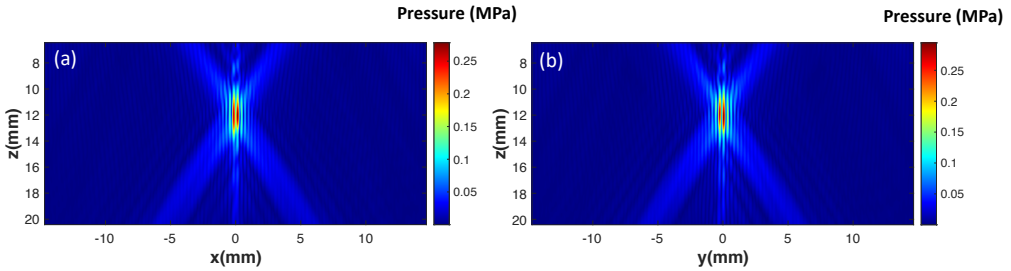

Figure 3.14: Pressure in the fluid (in MPa) in the xz plane (a) and yz plane (b) for the LF 3D tweezers with an infinite thickness wafer.

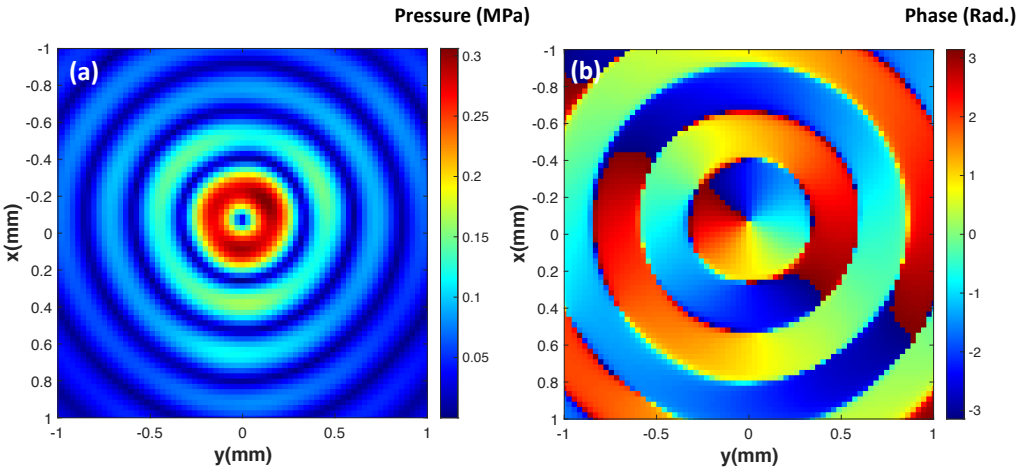

Figure 3.15: Pressure in the focal plane for the LF 3D tweezers with an infinite thickness wafer: (a) Amplitude (in MPa), (b) phase (in Radian).

Thus, the presence of the low amplitude parasitic wave propagating along the z axis is not linked to the finite thickness of the piezoelectric wafer, but to surface waves created on the interface between the piezoelectric wafer and the glass on which the electrodes are located.

3.5.2 Tweezers without glass plate

Now a low Frequency (LF) 3D device working at 5 MHz and made of a Y-36 cut $LiNbO_3$ wafer of 1 mm thickness in direct contact with water (with in fact a very thin layer of SU8 deposited the electrodes in experiments) is studied. The electrodes are designed to focus in water at 6.5 mm away from the transducers. C-PML is used to absorb the waves leaving the FEM computational domain in all directions except below the 1 mm thickness $LiNbO_3$ wafer. The calculation domain is limited to 74 x 74 wavelengths in width. The pressure (in MPa), at one wavelength from the electrode in water, calculated using the COMSOL Multiphysics is displayed in Figure 3.16. The pressure calculated from this source, using the angular spectrum method, in the xz plane and yz plane is shown in Figure 3.17. It can be seen that the focusing quality is better than the one obtained with the system having a glass layer between the piezoelectric wafer and the water, even if the amplitude of the wave obtained here is about two times weaker (0.15 MPa instead of 0.3 MPa) for the same excitation level (10V). The pressure in the focal plane at 6.5 mm from the electrodes, shown in Figure 3.18, confirms the high quality of the obtained vortex.

The simulation was redone considering a semi-infinite piezoelectric wafer. For this purpose a C-PML is also placed on the back side of the computational domain under the piezoelectric material. The pressure calculated in the fluid (in MPa) in the xz and yz plane in the focal plane are displayed in Figures 3.19 and 3.20 respectively. The results are very close to those obtained in the case of a 1 mm thick piezoelectric wafer, showing that in this case also the source of the vortex is mainly on the surface containing the electrodes.

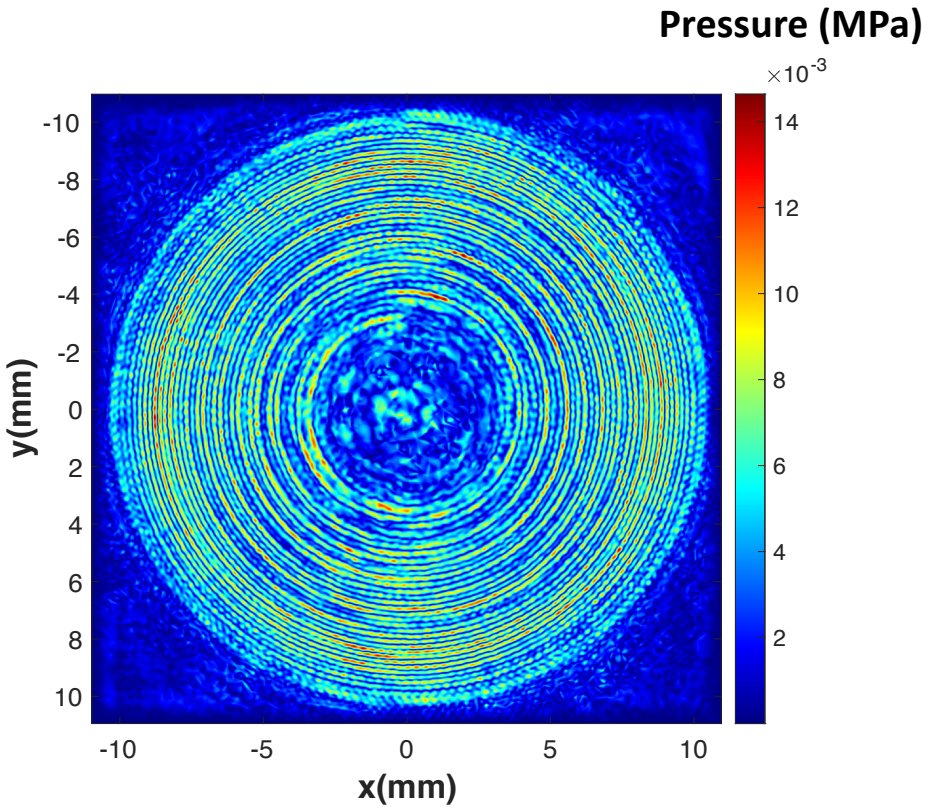

Figure 3.16: Pressure (in MPa), at one wavelength from the electrode in water calculated using the COMSOL Multiphysics simulation of the LF 3D tweezers with a 1 mm thickness wafer and without glass plate.

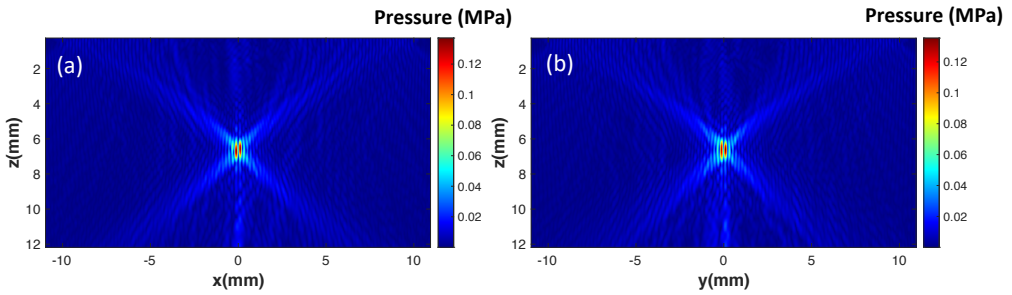

Figure 3.17: Pressure in the fluid (in MPa) in the xz plane (a) and yz plane (b) for he LF 3D tweezers with a 1 mm thickness wafer and without glass plate.

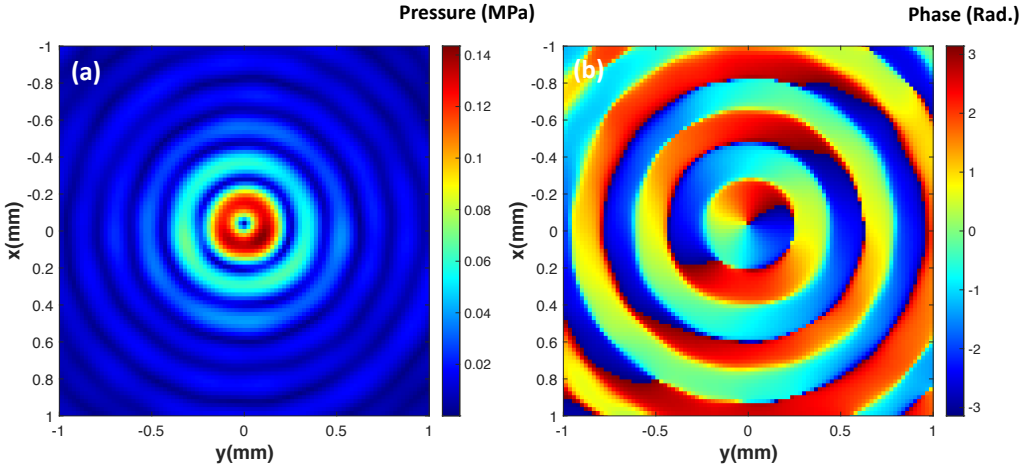

Figure 3.18: Pressure in the focal plane for he LF 3D tweezers with a 1 mm thickness wafer and without glass plate: (a) Amplitude (in MPa), (b) phase.

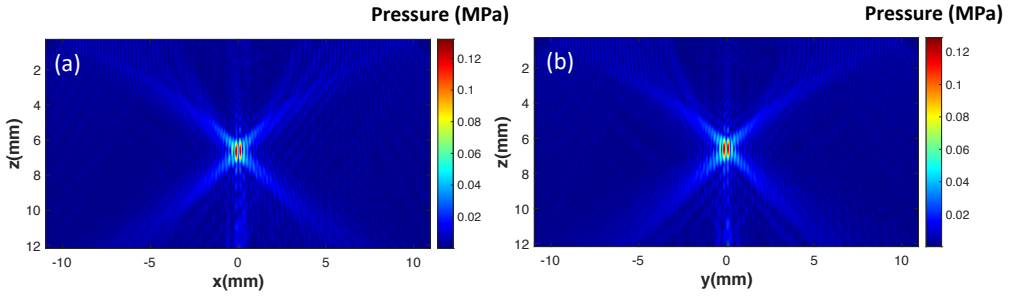

Figure 3.19: Pressure in the fluid (in MPa) in the xz plane (a) and yz plane (b) for the LF 3D tweezers with an infinite thickness wafer and without glass plate.

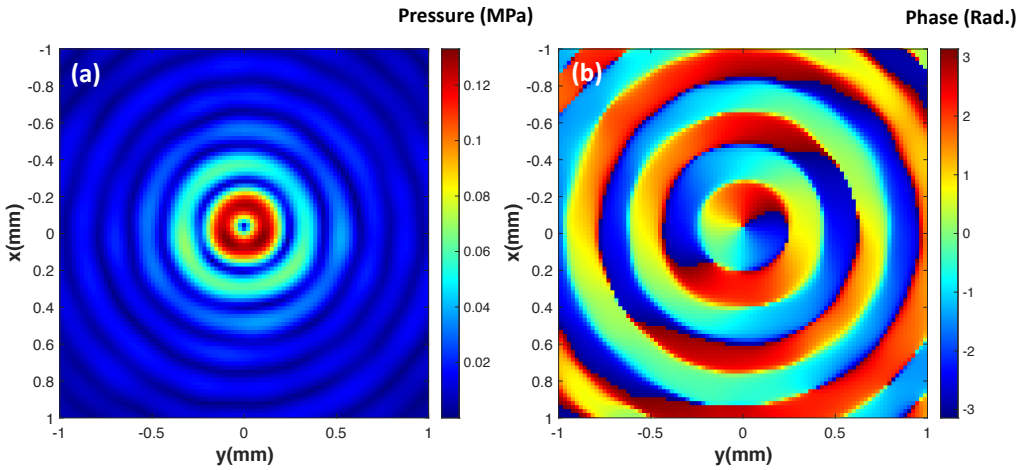

Figure 3.20: Pressure in the focal plane for the LF 3D tweezers with an infinite thickness wafer and without glass plate: (a) Amplitude (in MPa), (b) phase.

3.6 Conclusion

In this chapter a mixed method, combining a finite element simulation of the source and an angular spectrum technique for wave propagation in isotropic solids and fluids, has been described and used to study how a 3D tweezer made of a pair of spiral-shaped electrodes deposited on a $LiNbO_3$ wafer works.

A first design with a glass layer bonded on top of the piezoelectric substrate in order to use shear waves to focus a vortex in water, has been studied. The numerical study confirmed that it is indeed the shear waves (and more precisely the SV waves) which contribute to the generation of the vortex in water, and that the longitudinal waves also generated by the electrodes do not deteriorate the quality of the vortex obtained. The second design of the tweezers emitting directly into water allows to obtain better quality vortices but with a lower amplitude for the same level of excitation voltage imposed on the electrodes. In the studied designs, the finite thickness of the piezoelectric substrate has no significant influence on the focused vortices generated in water.

Chapter 4

Spatially selective manipulation of cells with single-beam acoustical tweezers

Abstract

Acoustical tweezers open major prospects in microbiology for cells and microorganisms contactless manipulation, organization and mechanical properties testing since they are bio-compatible, label-free and have the potential to exert forces several orders of magnitude larger than their optical counterpart at equivalent power. Yet, these perspectives have so far been hindered by the absence of spatial selectivity of existing acoustical tweezers - i.e., the ability to select and move objects individually - and/or their limited resolution restricting their use to large particle manipulation only and/or finally the limited forces that they could apply. Here, we report precise selective manipulation and positioning of individual human cells in a standard microscopy environment with trapping forces up to $\sim$ 200 pN without altering their viability. These results are obtained with miniaturized acoustical tweezers combining holography with active materials to synthesize specific wave-fields called focused acoustical vortices designed to produce stiff localized traps with reduced acoustic power. The results of this chapter have been published in [14].

4.1 Introduction

Contactless tweezers based on optical [1, 20] and magnetic forces [150, 151] have been developed in the last decades and have led to tremendous progress in science recognized by several Nobel prizes. Nevertheless, these technologies have stringent limitations when operating on biological matter. Optical tweezers rely on the optical radiation pressure, a force proportional to the intensity of the wave-field divided by the speed of light. The high value of the latter severely limits the forces which can be applied and imposes the use of high intensity fields. This can lead to deleterious photo-thermal damages (due to absorption-induced heating) and/or photo-chemical damages (due to excitation of reactive compounds like singlet oxygen) [152, 153, 154] adversely affecting cells' integrity. Magnetic tweezers, on the other hand, can only manipulate objects susceptible to magnetic fields and thus require other particles to be pre-tagged with magnetic compounds, a limiting factor for many applications. In microbiology, acoustical tweezers have many assets to become a prominent technology [155, 156, 157]. Indeed, they rely on the acoustical radiation force [26, 158], which is, as for their optical counterpart, proportional to the intensity of the wave divided by the wave speed. But, the drastically lower speed of sound compared to light leads to driving power several orders of magnitude smaller than in optics to apply the same forces (or conversely, forces several orders of magnitude larger at the same driving power) [26, 4]. In addition, the innocuity of ultrasounds on cells and tissues below cavitation and deleterious heating thresholds defined by the mechanical and thermal indexes is largely documented [159, 160, 161, 162] and demonstrated daily by their widespread use in medical imaging [163]. Indeed, the frequencies typically used in medical ultrasound ($1-100$ MHz) and in the present work (~ 45 MHz) are far below electronic or molecular excitation resonances thus avoiding adverse effects on cells' integrity. In addition, the attenuation in water at these frequencies remains weak for manipulation at the micrometric scale, hence limiting absorption induced thermal heating [161, 162]. Finally, almost any type of particles (solid particles, biological tissues, drops) can be trapped without pre-tagging [9] and the low speed of sound enables spatial resolution down to micrometric scales even at these comparatively low frequencies. Nevertheless, the promising capabilities offered by acoustical tweezers have so far been hindered by the lack of selectivity of existing devices [8, 7] and/or their restricted operating frequency [4, 73, 13, 164] limiting their use to large particles only. Here, selectivity refers to spatial selectivity, i.e. the ability to select and move an object independently of other neighboring objects. Yet, the ability to select, move and organize individual microscopic living organisms is of the utmost impor-

tance in microbiology for fields at the forefront of current research such as single-cell analysis, cell–cell interaction study, or to promote the emergence of disruptive research e.g. on spatially organized co-cultures. In this chapter, we unleash the potential of acoustical tweezers by demonstrating individual biological cells' manipulation and organization in a standard microscopy environment with miniaturized single-beam acoustical tweezers. The strength and efficiency of acoustical tweezers is illustrated by exerting forces ($\sim$ 200 pN) on cells one order of magnitude larger than the maximum forces reported with optical tweezers [165], obtained with one order of magnitude less wave power (<2 mW). Cells' viability was assessed following exposure to the acoustic field measured by short and long-term fluorescence viability assays.

4.2 Review of existing acoustical technologies for cells manipulation and experimental challenge

First experimental evidences of large particles trapping with acoustic waves date back to the early twentieth century [166]. Nevertheless, the first demonstration of controlled manipulation of micrometric particles and cells with acoustic waves appeared only one century later with the emergence of microfluidics and high frequency transducers based on interdigitated electrodes [8, 7]. In these recent works, trapping relies on the 2D superposition of orthogonal plane standing waves, an efficient solution for the collective motion of particles, but one which precludes any selectivity, i.e., the ability to select and move one particle out of a population[26]. Indeed, the multiplicity of nodes and anti-nodes leads to the existence of multiple trapping sites [167] which cannot be moved independently. In addition, multiple transducers or reflectors positioned around the manipulation area are mandatory for the synthesis of standing waves, a condition difficult to fulfill in many experimental configurations. With such orthogonal standing wave devices, Guo et al. [168] demonstrated (i) particles' collection at the multiple nodes of the standing wave-field; (ii) cells' patterning by bringing the cells one by one and waiting for each manipulated cell to adhere on the substrate in between two cells' manipulation (otherwise multiple free cells would move collectively and follow the same trajectory preventing their organization owing to the absence of spatial selectivity) and (iii) displacement of particles and cells along an axis perpendicular to the substrate by tuning the acoustic power to adjust the equilibrium between upward acoustic forces (acoustic radiation

force and acoustic streaming) and downward gravity. Selective trapping on the other hand, requires strong spatial localization and hence tight focusing of the wave-field. In optics, this ability has been achieved with focused progressive waves [1], a solution also investigated in acoustics [169]. But such wave-fields are inadequate in acoustics for most particles of practical interest, since objects with positive contrast factors (such as rigid particles or cells) are generally expelled from the focal point of a focused wave [42]. Acoustical vortices [12] provide an elegant solution to this problem [11]. These focused helical progressive waves spin around a central axis wherein the pressure amplitude vanishes, surrounded by a ring of high pressure intensity, which pushes particles toward the central node. Two-dimensional trapping [164, 68] and three dimensional levitation [73] and trapping [4] have been previously reported at the center of laterally and spherically focused vortices, respectively. Compared to tweezers based on focused beams operating in the Mie regime [170], the vortex-based tweezers enable to trap objects with positive contrast factors at the beam center, in 3D, and at lower operating frequencies, hence limiting deleterious heating. Conversely, these lower frequencies (and hence wavelength) lead to weaker gradients compared to tweezers operating in the Mie regime. However, all demonstrations with vortex based tweezers were performed on relatively large particles (> 300 μm in diameter) using complex arrays of transducers, which are cumbersome, not compatible with standard microscopes, and which cannot be easily miniaturized to trap micrometric particles. Recently, Baudoin et al. [13] demonstrated the selective manipulation of 150 μm particles in a standard microscopy environment with flat, easily integrable, miniaturized tweezers. To reach this goal, they sputtered holographic electrodes at the surface of an active piezoelectric substrate, designed to synthesize a spherically focused acoustical vortex. Nevertheless, transcending the limits of this technology to achieve selective cells' manipulation remained a major scientific and technological challenge. Indeed, the system should be scaled down (frequency up-scaling) by a factor of 10 (since cells have a typical size of 10 μm), while increasing drastically the field intensity, owing to the low acoustic contrast (density, compressibility) between cells and the surrounding liquid [171, 172]. In addition, since the concomitant system's miniaturization and power increase are known to adversely increase the sources of dissipation, the tweezers had to be specifically designed to prevent detrimental temperature increase and enable damage-free manipulation of cells.

4.3 Experimental setup

Spherically focused acoustical vortices (Figure 4.1A) were chosen to trap the particles. Indeed, the energy concentration resulting from the 3D focalization (Figure 4.3F) enables to reach high amplitudes at the focus from low power transducers. These spherically focused vortices were synthesized by materializing the hologram of a $\sim$ 45 MHz vortex [13] with metallic electrodes at the surface of an active piezoelectric substrate. The hologram was discretized on two levels resulting in two intertwined spiraling electrodes (Figure 4.1D), patterned in a clean room by standard photo-lithography techniques (fully described in chapter 2). The scale reduction compared to our previous generation of acoustical tweezers [13] is illustrated in Figure 4.1B. Second, the design of the electrodes was optimized to reduce Joule heating (magnified by the scale reduction) inside the electrodes. To prevent this effect, (i) the thickness of the metallic electrodes was increased by a factor of 2 (400 nm of gold and 40 nm of titanium); (ii) the width of the electrical connections (Figure 4.1D) supplying the power to the spirals was significantly increased to prevent any dissipation before the active region; and (iii) two radial electrodes spanning half of the spirals were added as a way to effectively bring power to the driving electrode. Third, a 1.1 mm glass wafer of borosilicate D263 T (PGO Online) (Figure 4.1A, C) was glued to the electrodes, using optically transparent epoxy glue (EPOTEK 301-2), and placed in between the transducers and the microfluidic chamber wherein the cells are manipulated. This glass substrate has a double function: (i) it enables the focalization of the wave and (ii) it thermally insulates the microfluidic device from the electrodes. The final device hence consists of (i) spiraling holographic transducers excited with a sinusoidal electrical signal generating an acoustical vortex that propagates and focuses inside a glass substrate; (ii) a microfluidic PDMS chamber supported by a glass slide containing cells and placed on top of the substrate, wherein the acoustical vortex creates a trap and (iii) a motorized stage that enables the X,Y displacement of the microfluidic chamber with respect to the trap. The whole transparent setup is integrated in an inverted microscope as depicted in Figure 4.1E

4.4 Characterization of the acoustical trap

The principle of high frequency acoustical vortices synthesis with these active holograms was assessed through the comparison of numerical predictions obtained from an angular spectrum code and experimental measurements of the acoustic field normal displacement at the surface of the glass slide (XY

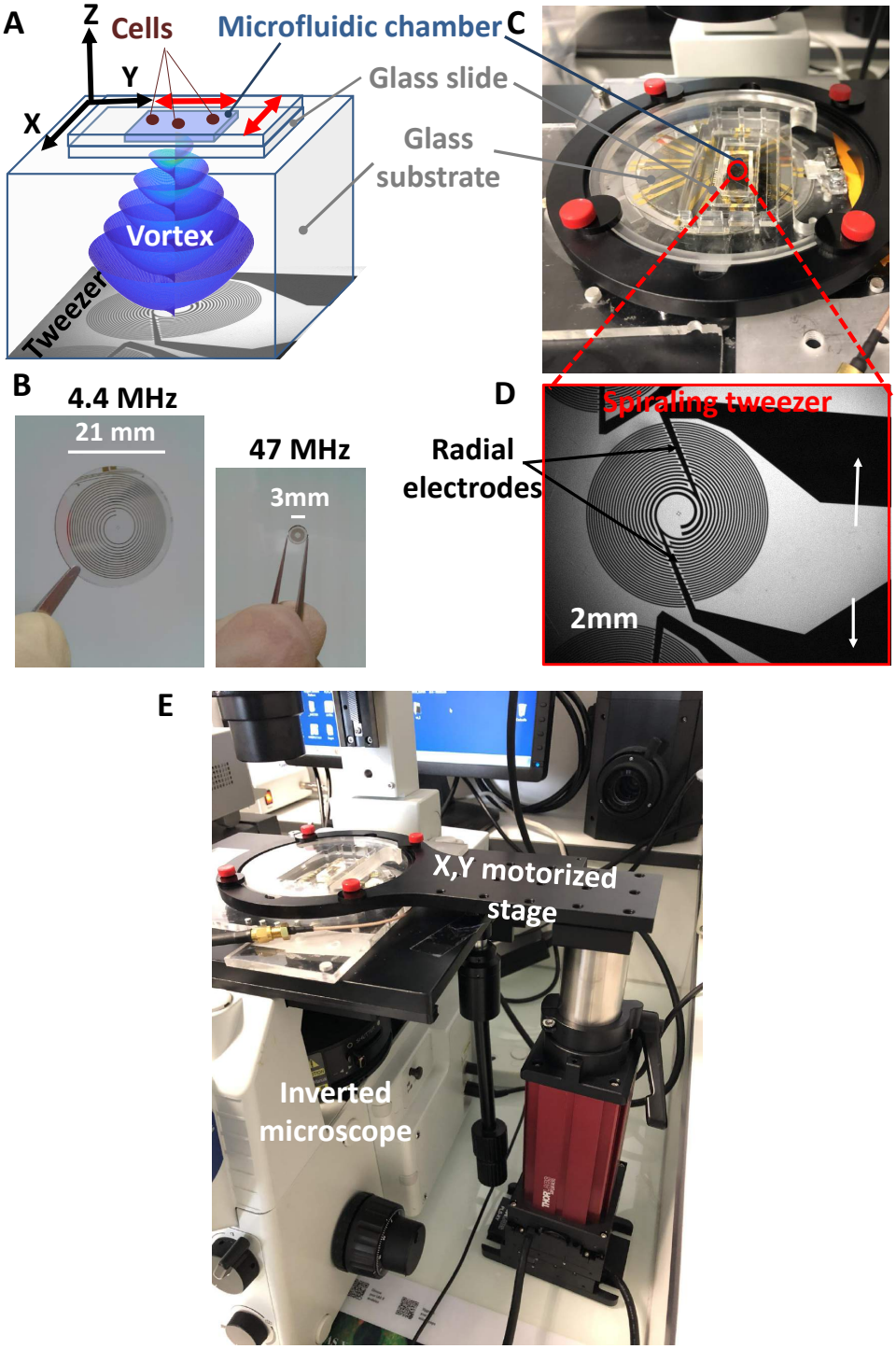
A
Z
Cells
Microfluidic chamber
Y
X
Glass slide
Glass substrate
Vortex
Tweezer
C
B
4.4 MHz
21 mm
47 MHz
3mm
D
Radial electrodes
Spiraling tweezer
2mm
E
X,Y motorized stage
Inverted microscope

Figure 4.1: Experimental setup. A) Illustration of the working principle of the tweezers designed for cells' selective manipulation: A spherically focused acoustical vortex is synthesized by spiraling active electrodes metallized at the surface of a piezoelectric substrate and actuated with a function generator connected to an amplifier. The vortex propagates and focalizes inside a glued glass substrate and then reaches a microfluidic chamber made of a glass slide and a PDMS cover containing cells embedded in a growth medium. The microfluidic device is acoustically coupled with the transducer with a thin layer of silicone oil. A cell located at the center of the acoustical vortex is trapped. Its motion relative to other cells is enabled by the displacement of the microfluidic chamber driven by a XY motorized stage. B) Picture of typical transducers used in the present study (right) and illustration of the scale reduction compared to previous lower frequency designs by Baudoin et al. [13] (left). C) Image of the actual experimental setup. D) Zoom-in on the spiral transducer and the electrical connections (in black). E) Illustration of the integration of the whole setup inside a standard inverted microscope.

plane) (Figure 4.3A-D) with a Polytech UHF-120 laser Doppler vibrometer (Figure 4.2). Note that in the simulations presented in this chapter, the source is not obtained from the Finite Element Method (FEM) introduced in Chapter 3, but by directly taking the phase descretized over two levels (design of the electrodes) as the pressure source.

Both the magnitude and phase are faithful to the simulations and demonstrate the ability to generate high frequency acoustic vortices. As expected, the wave-field exhibits a central node (corresponding to the phase central singularity) surrounded by a ring of high intensity which constitutes the acoustical trap. The magnitude of the sinusoidal acoustic field (displacement) depends on the driving electrical power and was measured to vary typically between 0.1 and 1 nm, at the electrical power used in the manipulation experiments. This corresponds to acoustic powers lying between 20 μW and 2 mW. The concentration of the acoustic energy through focalization in the propagation plane (XZ) can be seen in Figure 4.3E.

An estimation of the lateral force field exerted on a cell of 10 μm radius with density 1100 kg m^{-3} and compressibility 4×10^{-10} Pa^{-1} was computed at each point in the manipulation plane of the microfluidic chamber (XY plane, Figure 4.3F) with the theoretical formula derived by Sapozhnikov and Bailey [41]. This calculation gives an estimation of the force of the order of 100 pN, which can nevertheless strongly vary depending on the cells' exact properties. This order of magnitude agrees with the maximum force measured experimentally (200 pN) for similar parameters (presented in this chapter). These simulations of the lateral force also show that as long as a cell is located at a distance of $\leq$ 40 μm from the center of the vortex, it is

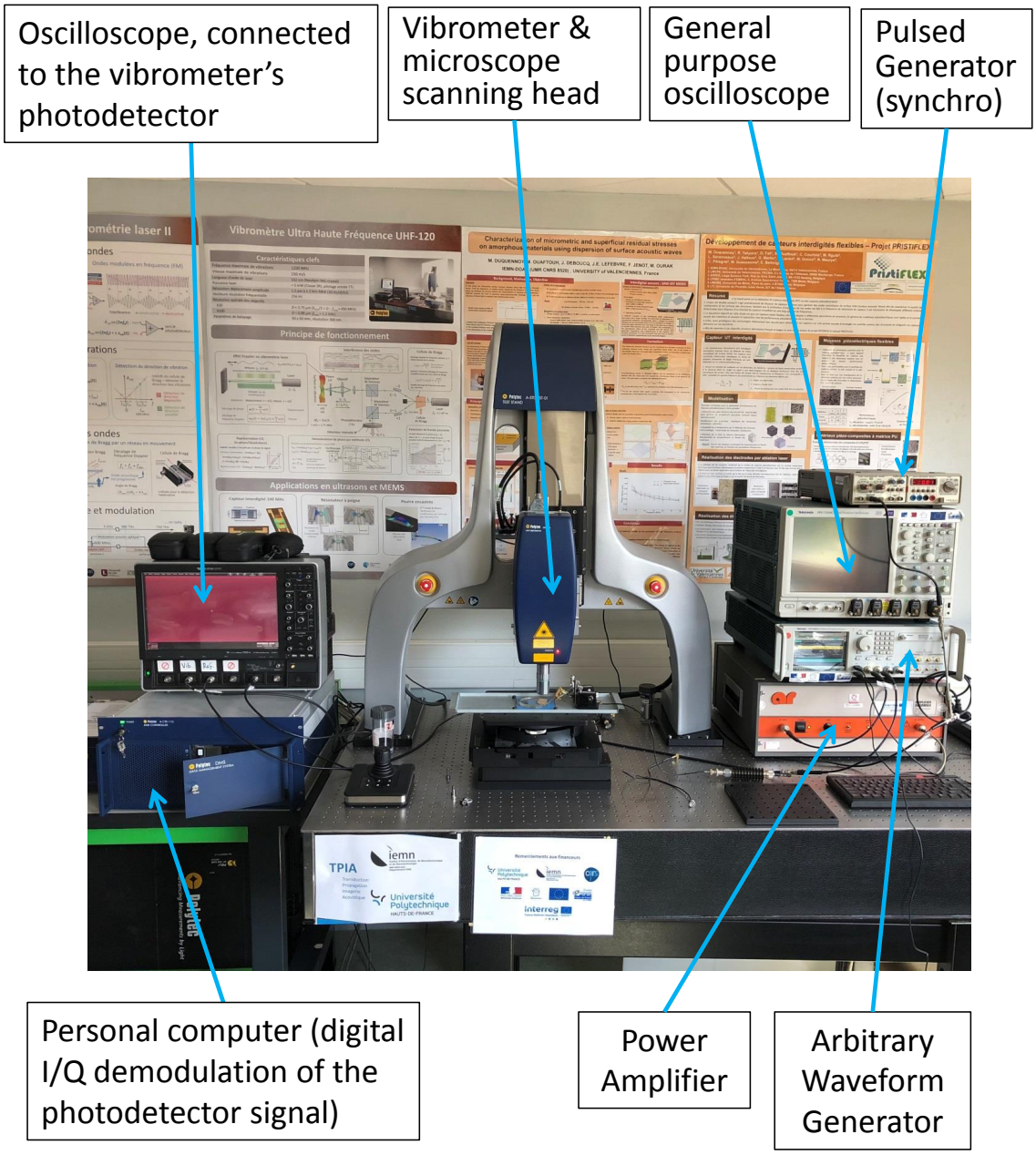

Figure 4.2: Polytech UHF-120 laser Doppler vibrometer.

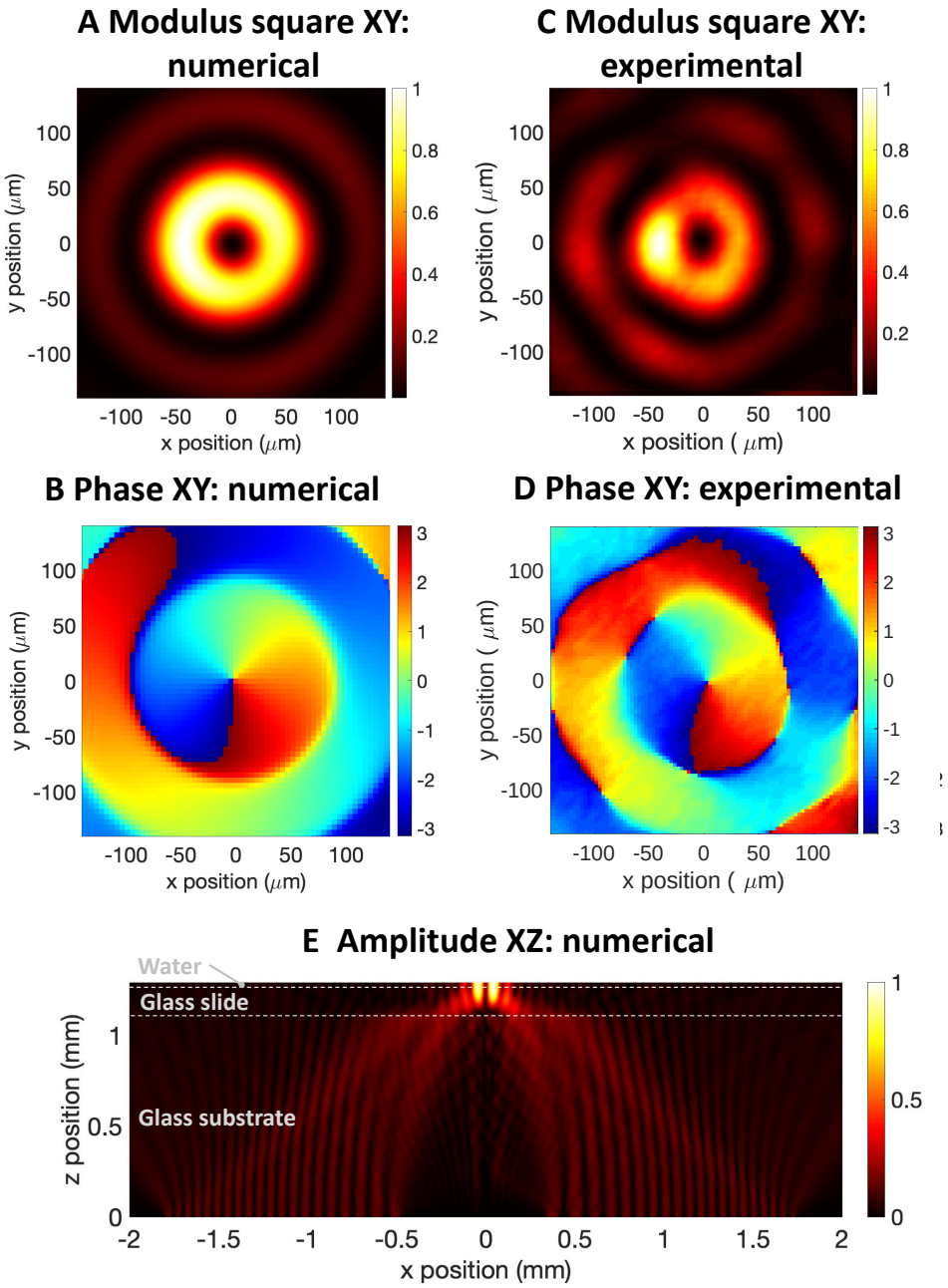
A Modulus square XY: numerical
C Modulus square XY: experimental
B Phase XY: numerical
D Phase XY: experimental
E Amplitude XZ: numerical
y position (μm)
x position (μm)
z position (mm)
x position (mm)
Water
Glass slide
Glass substrate

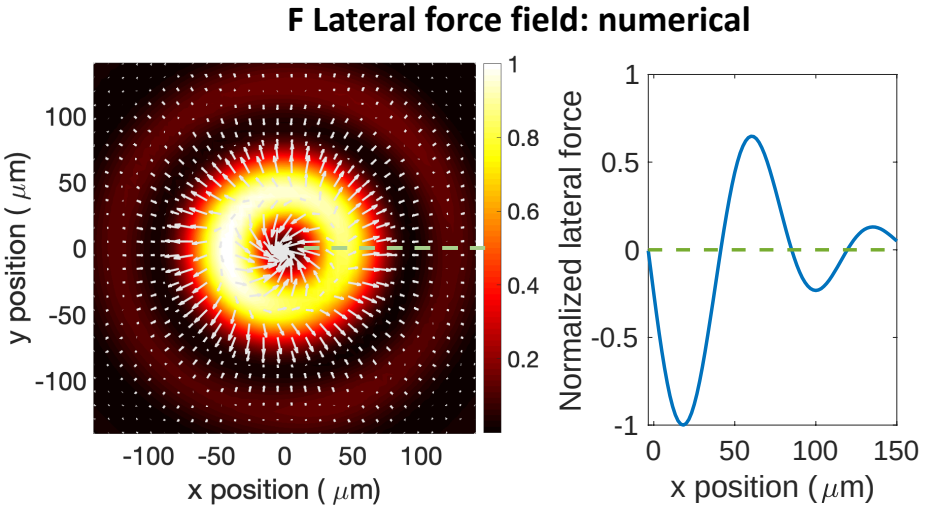

Figure 4.3: Acoustic field and radiation forces. A-D Numerical predictions (A, B) and experimental measurements (C, D) with a UHF-120 Polytec laser Doppler vibrometer of the normalized modulus square (A, C) and phase (B, D) of the acoustic normal displacement at the surface of the glass slide (XY plane). The displacement magnitude is normalized by its maximum value measured to lie between 0.1 and 1 nm depending on the electrical power applied to the transducers. E) Simulated evolution of the amplitude of the acoustic field in the propagation plane (XZ) from the source to the center of the channel. This simulation illustrates the concentration of the acoustic energy through focalization. F) Normalized magnitude and distribution of acoustic forces. Left: the white arrows show the convergence of the force field toward the center of the beam but also that the first ring is repulsive for particles located outside the trap. Right: Magnitude of the lateral force along the green dashed line plotted in the left figure. When the force is negative, the particle is pushed toward the center of the acoustic vortex, while when it is positive it is pushed outward. Zero values correspond to static equilibrium positions. The magnitude of the maximum trapping force computed with the code varies between 30 and 650 pN for vibration amplitude of 1 nm (acoustic power of 2 mW) depending on the exact cells acoustic properties [171, 172].

attracted toward the center of the beam (the lateral force is negative). This distance corresponds approximately to the first ring radius and defines the spatial selectivity of the tweezers.

4.5 Cells manipulation

Cell manipulation is demonstrated in a microfluidic device integrated in a standard inverted microscope (Figure 4.1E) to illustrate the fact that our approach can be easily transposed to standard microbiology experiments. The device is composed of a thin glass slide treated to prevent cell adhesion and a PDMS chamber of controlled height (38 μm). The cells are loaded by placing a drop of the cell suspension (10–20 μL) on the glass surface using a micro-pipette and carefully lowering the chamber on top of the drop. The position of the vortex core is spotted with four triangular marks deposited at the surface of the glass substrate. Using an XY positioning system it is thereafter possible to align the tweezers' center to any cell present in the chamber. Upon activation of the AC driving signal, a cell situated inside the vortex core is nearly instantaneously trapped. The first demonstration of the selective nature of our tweezers is showcased by our ability to pick up a single cell (breast cancer cell MDA-MB-231, 7 ± 1 μm in radius) among a collection of cells and move it along a slalom course where other free-to-move cells act as poles (see Figure 4.4). Then a second cell initially serving as a slalom marker is moved to prove that it was free.

The precise displacement can be performed in any direction as demonstrated by the square motion of a cell around another (Figure 4.5) so it demonstrates that the cell can move in all XY directions. Moreover, the displacement is performed in the presence of another cell (Figure 4.5). Displacement can be performed even in the presence of other cells without any risk of coalescence as the first ring acts as a barrier. As can be seen in Figure 4.3 C, the radius of the first repulsive ring is typically 40 μm. This repulsive ring can also be used to separate a single cell from a cluster by activating the tweezers with the repulsive barrier located between the target cell and the other cells. In this way the target cell is attracted toward the vortex center while the other is expelled (Figure 4.6).

Note also that the lateral force reaches a maximum for a distance $\sim$20 μm from the center and then decreases until it reaches 0 at 40 μm. Because of this, a cell can be moved closer than 40 μm from another cell if there is a slight adherence of the cells on the substrate. Adhered cells can then be de-

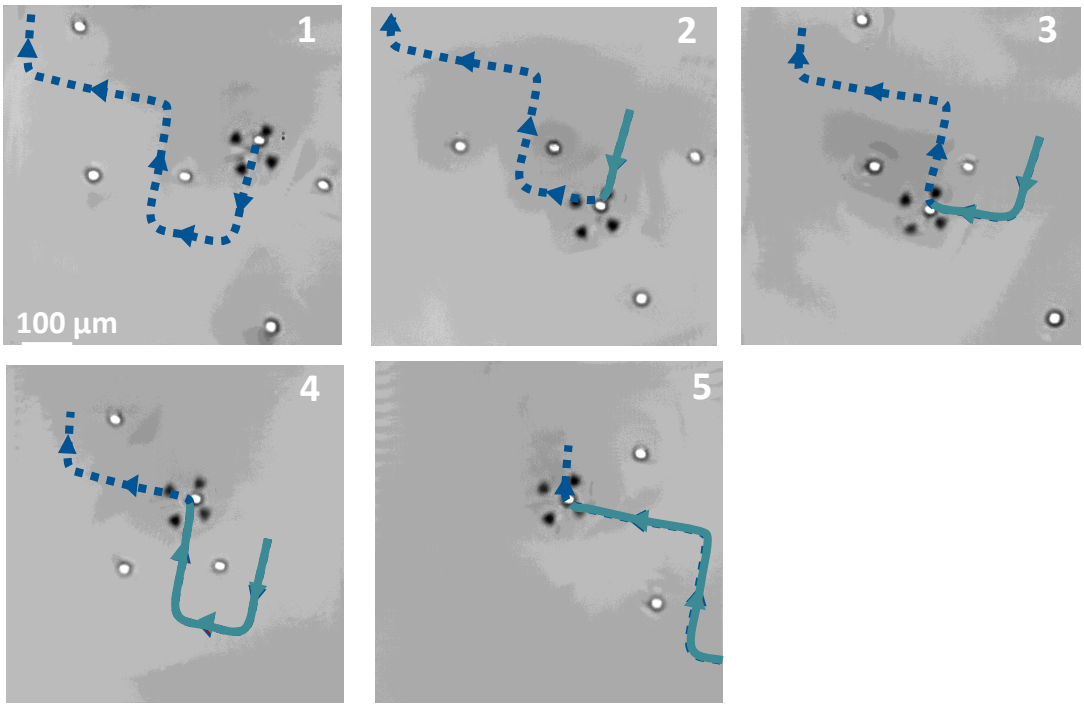

Figure 4.4: Stack of images illustrating the selective manipulation of a human breast cancer cell (MDA-MB-231) of radius 7 ± 1 μm between other cells. The blue dotted line and green continuous line show, respectively, the future and past path followed by the cell.

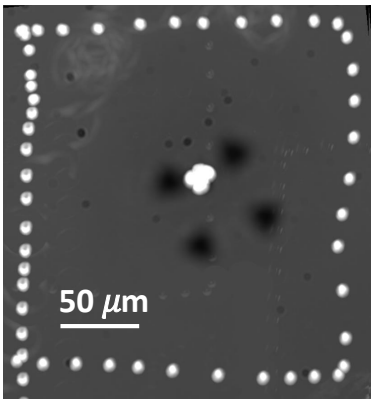

Figure 4.5: Image illustrating the square relative motion of a trapped cell 1 of 7 ± 1 μm (located in the center of the picture) around another cell 2 obtained by superimposing the images of the two cells in the frame of reference of the trapped cell. In this frame of reference, the successive positions of cell 2 form a square.

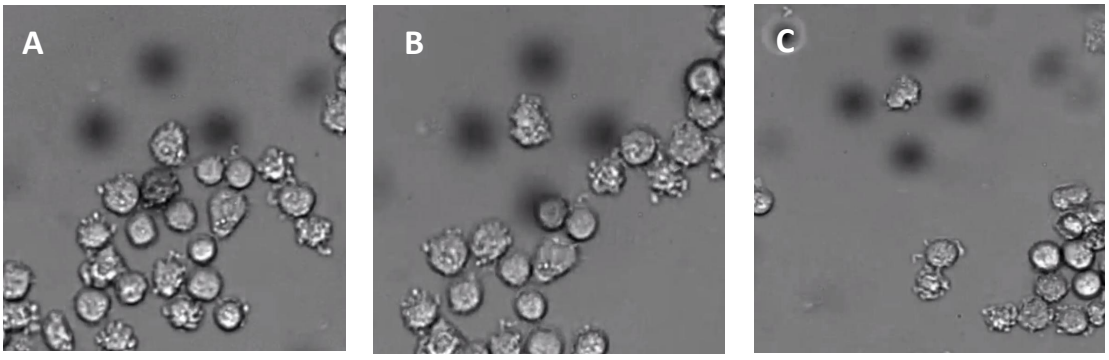

Figure 4.6: Separation of a single cell from a cluster after activating the acoustical tweezers.

tached by increasing the acoustic power. Note also that second ring of much weaker intensity can also slightly affect free cells at large power.

One of the key ability enabled by selective acoustical tweezers is the capture, positioning, and release of cells at precise locations. As an illustration, a total of ten individual MDA cells were therefore positioned to spell the letters A and T of the words Acoustical Tweezers (Figure 4.7). The total manipulation time to achieve these results was kept under 10 minutes (<2 mins per cell). All the operations represented in this section were performed with acoustic vibration displacements <0.5 nm.

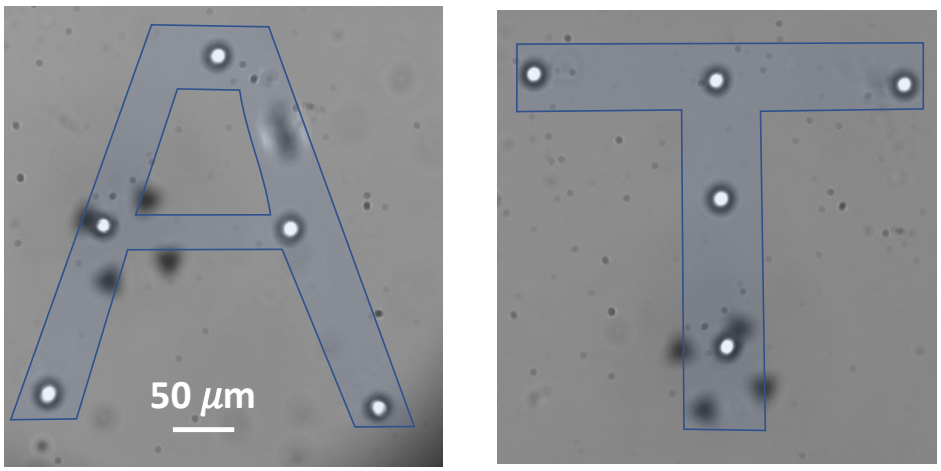

Figure 4.7: Manipulation of ten MDA cells (average radius 9 μm to form the letters A and T of the words Acoustical Tweezers). This alignment procedure was reproduced twice. Note that in these pictures the focus is voluntarily left under-focused to improve contrast of the cells.

Finally, we performed some experiments to quantify the forces that can be exerted on cells with these tweezers. For this purpose, cells were trapped and then moved with an increasing speed until it was ejected from the trap. Velocities up to 1.2 mm s^{-1} before ejection have been measured for cell displacement of diameter 12 ± 1 μm trapped with an acoustic field of magnitude 0.9 nm in a micro-chamber of height 38 μm. This corresponds to a trapping force of 194 ± 35 pN according to Faxen's formula [173], which lies in the range predicted by theory. As a comparison, this force is one order of magnitude larger than the maximum forces (20 pN) reported by Keloth et al. [165]

with optical tweezers and obtained with one order of magnitude less power (1.8 mW here compared to the 26.8 mW used for optical trapping). Note that even at these comparatively large trapping force, the mechanical index in the present experiments (≤ 0.15) remains far below the safety threshold (1.9) defined to ensure tissue safety for medical imaging. Furthermore, unlike with optical tweezers, it is still possible to substantially increase this force with acoustical tweezers by increasing the actuation power and improving the thermal management of the device, as most of the dissipated power comes from the transducer and not from the direct absorption by the medium.

4.6 Cells viability

As described in the introduction, one of the main gains that can be expected from transitioning from optical to acoustical tweezers is the absence of deleterious effects of the latter when manipulating living cells. The short and long-term viability was investigated using a fluorescent viability assay as well as post exposure cell observation. A first set of experiments was thus conducted to address the short-term viability of MDA cells on eight cells. The cells were captured for 2 min in the vortex at maximum power (amplitude 0.9 nm) to mimic a standard positioning sequence and observed for any sign of damage during manipulation and for 30 min afterwards. During manipulation, no increase of fluorescence was observed suggesting that the sound field does not induce membrane permeabilization which correlates with viability decrease [174]. After the tweezers were switched off, the cell did not display any increase of fluorescence. This supports that short-term damages produced by the acoustical tweezers are minimal. It is however known that damages experienced by a cell can lead to its death for hours afterwards [175]. To assess the long-term impact of cell manipulation using acoustical tweezers, we performed a viability assay overnight. Nine cells located at different positions in the two different microfluidic chambers were exposed to the tweezers of acoustic vortex at maximum power for 2 min each. An observation of the cells was performed after 19 h to compare their viability with a control region of the device (see Figure 4.8A). No extra mortality was observed in the illuminated region (dead/live cell ratio of 3%) compared to the statistics performed on the overall device (dead/live cell ratio of 5%). This likely indicates that the dead cells are depositing randomly and that the tweezers do not provoke extra mortality. We also studied in detail the fate of the nine illuminated individual cells (see Figure 4.8B–E). All the cells exposed to the acoustic field (the green circle indicates the extension of the first ring of the vortex) and their immediate neighbors were alive and showed

no difference compared to the nearby cells.

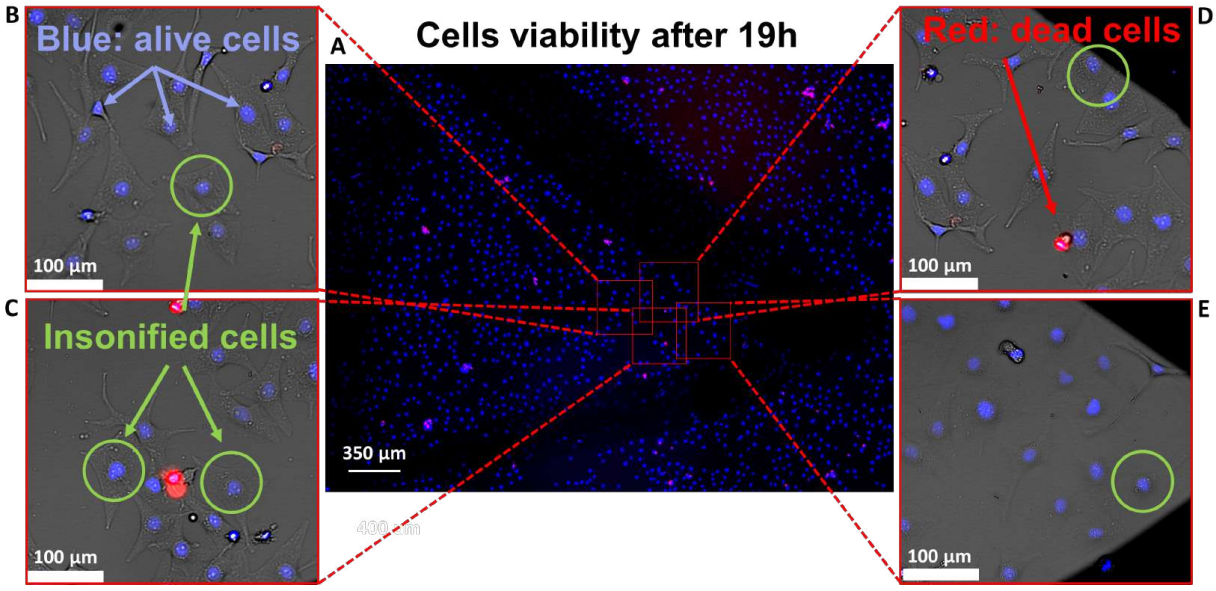

Figure 4.8: Cells' viability monitoring. A) Overview of the central part of the microfluidic device in which the viability experiments were performed. The cells are stained using a viability kit and imaged at 360 and 535 nm excitation (460 and 617 nm emission). The cell nucleus are represented in blue, while the dead cells appear in red. The whole field of view contains 4581 cells (226 dead—5%) while the region where manipulation took place contains 166 cells (5 dead 3%). B–E) Details of the five cells exposed to the acoustical tweezers for 2 min (four others were exposed on another similar device). The green circle represents the first ring of the trap. Long-term viability tests were performed overall on nine insonified cells in two different microfluidic chambers.

Another assay was made to ensure that the cells are still able to duplicate after manipulation. Five cells were exposed to 1min ultrasounds at the same power used as the one used for cells organization to for the letters A,T. After manipulation, the cells were left for 80 hours in a culture medium to study their proliferation. After this time (Figure 4.9D), we can clearly see that all manipulated cells duplicated normally, indicating that they were not affected nor damaged by the acoustic field.

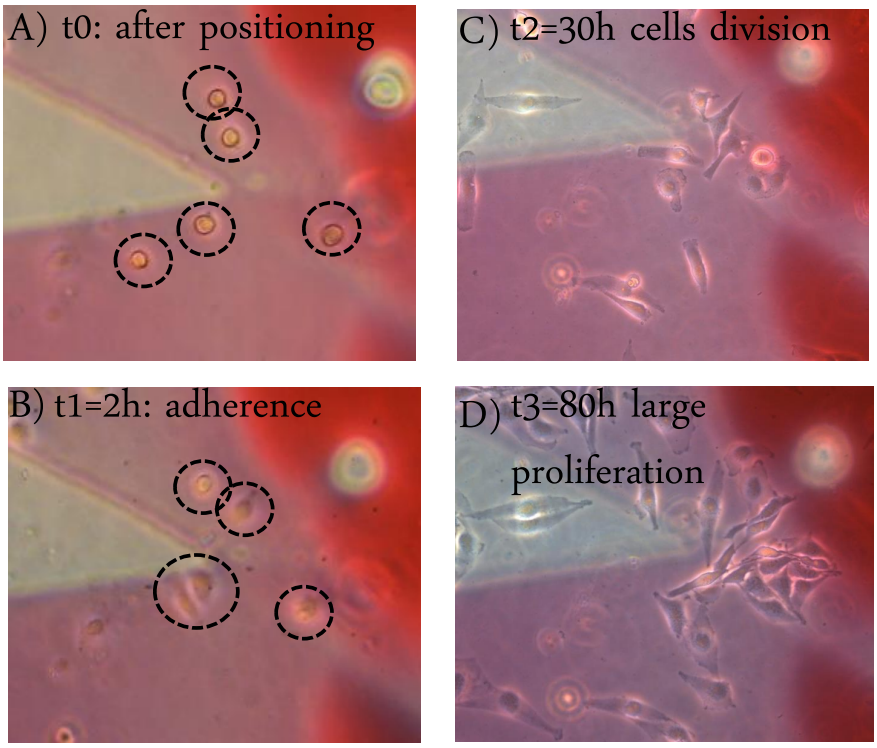

Figure 4.9: Cells duplication. A) Represents the 5 cells that were exposed to the acoustical tweezers. B) Adherence of the cells after 2 hours. C) Division of the cells after 30 hours. D) Shows the duplication of the cells after 80 hours indicating that their viability was not affected by the acoustic field.

4.7 Temperature variation induced by acoustical tweezers

Finally, the temperature increase due to Joule heating in the electrodes as well as the total temperature increase due to both Joule heating and acoustic wave absorption was measured (seen in Figure 4.10) using an infrared camera to assess potential impact on biological material. For most experiments presented in this chapter (corresponding to acoustic displacement <0.6 nm), the temperature increase is lower than 2.2^{o}C after 2 min of manipulation and even vanishes for the lowest power (0.1 nm). It reaches a maximum value of 5.4^{o}C at the top of the glass slide and 5.5 ^{o}C inside a drop of glycerol placed on top of the glass slide (acting as a perfectly absorbing medium) at the highest power used for high speed displacement of the cells. These measurements indicate that the first source of heat is Joule heating in the electrodes which could be solved by active cooling of the transducer. They also suggest that even at the largest power used in the present experiments, the moderate temperature increase remains compatible with cells' manipulation. Indeed, the thermal increase, even in the worst-case scenario remains lower than the 6^{o}C recommended to ensure tissues' safety in medical imaging.

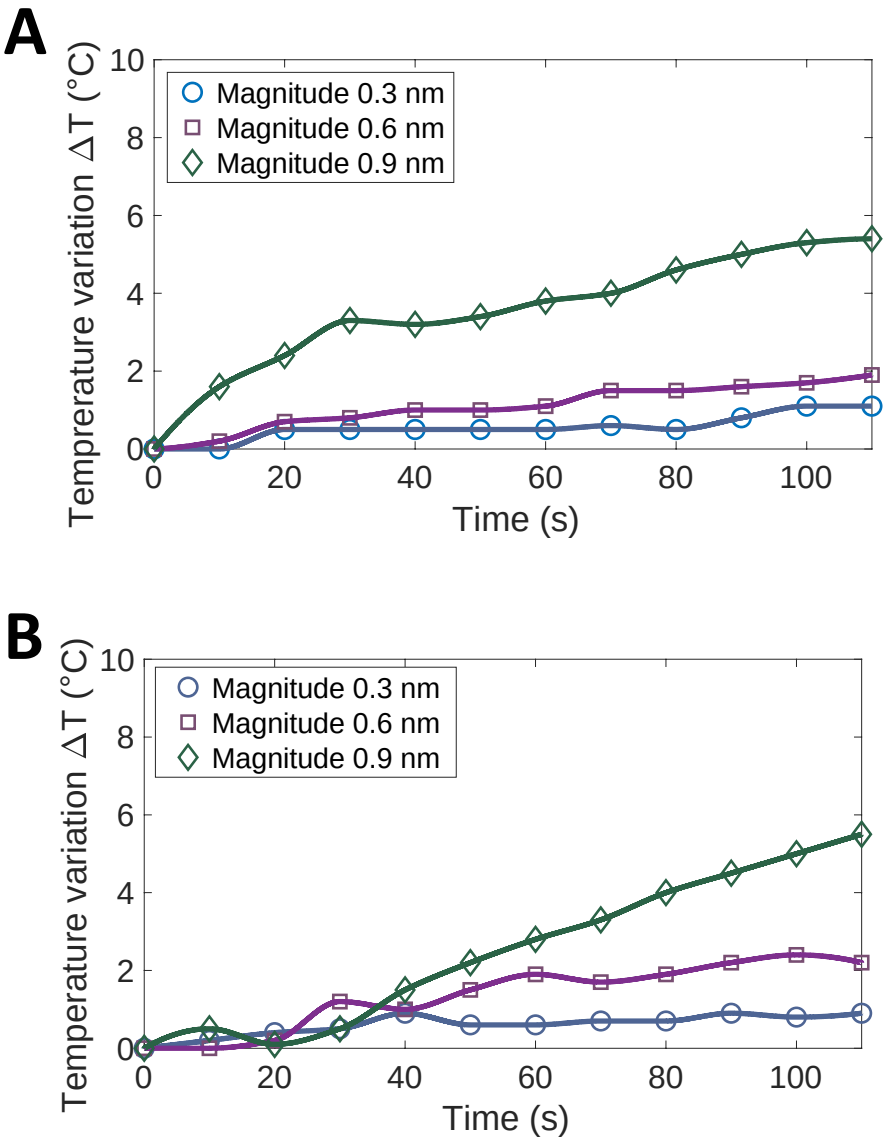

Figure 4.10: Temperature variation induced by acoustical tweezers. The measurements were performed with an infrared camera Testo 871 for different acoustic displacement magnitude. A) Measurement at the top of the glass slide. B) Measurement inside a glycerol layer deposited on top of the glass slide and acting as a perfectly absorbing layer. The data represented on these graphs represent single measurements. These measurements were conducted twice with similar results.

4.8 Conclusion

In this work, cell selective manipulation is demonstrated through the capture and precise positioning of individual cells among a collection in a standard microscopy environment. Both short and long-term viability of manipulated cells is evaluated, showing no impact on cells' integrity. This opens widespread perspectives for biological applications wherein precise organization of cells or microorganisms is a requisite. In addition, trapping force over wave intensity ratio two orders of magnitude larger than the one obtained with optical tweezers is reported with no deleterious effect such as phototoxicity. In future work, both the trapping force and selectivity could be further improved for 2D manipulation by increasing the tweezers' working frequency. Based on considerations on the dissipation of acoustic waves in water, one can indeed envision acoustical tweezers working up to several hundred MHz. The applied force could be also increased by improving thermal management of the device to limit Joule heating. In this way, it would be possible to apply stresses several orders of magnitude larger than with optical tweezers without altering cells' viability, a promising path for acoustic spectroscopy [156], cell adhesion [176] or cell mechanotransduction [177, 178] investigation. Indeed, the calibration of these tweezers would enable to apply controlled stresses to cells and monitor their response in force ranges not accessible before with other contactless tweezers. Furthermore, additional abilities could be progressively added to these tweezers: The focused vortex structure used for selective particle trapping in this chapter is also known to exhibit 3D trapping capabilities [4, 11]. This function was not investigated here owing to the confined nature of the micro-chamber but could closely follow this work. Synchronized vortices could also be used to assemble multiple particles, as recently suggested by Gong and Baudoin [179]. This would enable the investigation of tissue engineering [180] and envision 3D cell printing. Finally, the most thrilling and challenging perspective to this work might be the future development of Spatial Ultrasound Modulators (analogs to Spatial Light Modulator in optics), designed to manipulate and assemble many objects simultaneously. While such a revolution is on the way for large particles' manipulation in air [181, 182, 183], it would constitute a major breakthrough at the microscopic scale in liquids wherein the actuation frequencies are three orders of magnitude larger. The present work constitutes a cornerstone towards widespread applications of acoustical tweezers for biological applications.

Appendix

Additional information on the tweezers design

The tweezers were designed by materializing, with metallic electrodes, the hologram of a spherically focused acoustical vortex at the surface of an active piezoelectric substrate following Baudoin et al. [13] (see Chapter 2 for details). In the experiments described in this chapter, three slightly different transducers were used: The first transducer (referred as Tweezer 1, Figure 4.11A) was designed to excite transverse wave (sound speed $\approx 3500ms^1$) in a D263T borosilicate glass substrate of thickness 1.1mm. The electrodes have an inner radius of 0.75 mm and outer radius of 1.6 mm, hence describing eight turns around the central axis. Since the speed of sound in glass substrates can vary substantially depending on the exact fabrication process, the precise resonance frequency was determined with a laser Doppler vibrometer. The measured value was 47 MHz, used as the actuation frequency. These tweezers were used for the experiments reported in Figures 4.4, 4.6, 4.8, and 4.9. Note that a transverse wave in the solid can produce a longitudinal wave in the fluid as long as the incidence is not normal. Indeed, while longitudinal and transverse modes are two independent modes in the bulk of a solid they are coupled at an interface. The second transducer (Tweezer 2, Figure 4.11B) was used to produce longitudinal wave (sound speed $\approx 3200ms^1$) in a glass SF 57 HT ULTRA. The resonance frequency determined with the vibrometer was 43.5 MHz. The electrodes had an inner radius of 0.25 mm and outer radius of 2 mm, hence describing 12 turns around the central axis. This transducer was used in its longitudinal excitation mode to perform experiments reported in Figures 4.5 and 4.7. The third and last transducer (Figure 4.11C) was similar to the second transducer but with only ten turns of the electrodes. This transducer was used for the determination of the speed of displacement and for the comparison of the acoustic field represented in Figure 4.3C,D). The advantage of the second and third transducers is that the smaller inner radius of the electrodes results in weaker secondary rings. The advantage of the first transducer is that the type of glass matches with the glass slide (cover-slip also in borosilicate) resulting in better transmission of the acoustic signal from the glass substrate to the microfluidic chamber and thus higher intensities at same actuation power.

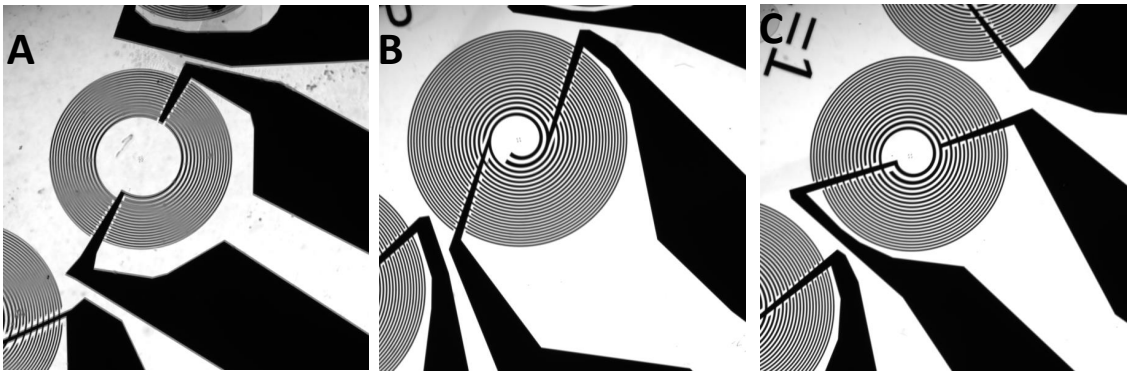

Figure 4.11: 3 different transducers used in the experiments in this chapter.

Additional details on the experimental characterization of the acoustic field

The acoustic field out-of-plane normal displacement was measured at the top of a metallized glass slide (to improve reflectivity) with a Polytech UHF-120 laser Doppler vibrometer equipped with a Mitutoyo M plan Apo $\times 20$ objective. The measures were performed in FFT mode by applying a chirp signal (typically ranging from 10 to 50 MHz), which enables a frequency treatment of the data. For the determination of the amplitude of vibration, the tweezers were excited with the exactly same frequency generator (IFR 2023 A) and amplifier (AR50A250 Amplifier 150 W) as the one used in the experiments.

Chapter 5

Ultra-high frequency vortex-based tweezers for microparticles manipulation with high spatial selectivity and NanoNewton forces

Abstract

Acoustical tweezers based on focused acoustical vortices open some tremendous perspectives for the in vitro and in vivo remote manipulation of millimetric down to micrometric objects, with combined selectivity and applied forces out of reach with any other contactless manipulation technique. Yet, the synthesis and characterization of high frequency acoustical vortices to manipulate smaller and smaller objects remains a major challenge. In this chapter, a 250 MHz acoustical vortex is synthesized with an active holographic transducer based on spiraling interdigitated transducers. It is shown that this ultra-high frequency vortex enables to trap and position individual particles in a standard microscopy environment with high spatial selectivity and NanoNewton forces. This work opens perspectives to explore acoustic force spectroscopy in some force ranges that were not accessible before.

5.1 Introduction

The precise manipulation of objects at small scales is paramount to explore the properties of the micro- and nano world. In the last decades, the development of optical and magnetic tweezers led to some revolution in microbiology [184], such as the characterization of the dynamics and force of molecular motors [185, 186] or the exploration of the structural and mechanical properties of DNA [187, 188, 189, 190]. Yet, these micro-manipulation techniques also suffer from major limitations: (i) The forces, which can be applied by these techniques are typically limited to a few picoNewtons in the operating regime compatible with bio-manipulations [191, 188, 192] even if maximum forces in the NanoNewton range have been reported for specific anti-reflection coated particles and high beam power [193]. (ii) Optical tweezers can induce photothermal and photo-chemical damages to living organisms [194, 195, 196, 197] and cannot operate in vivo in optically opaque media. (iv) magnetic tweezers can only exert forces on magnetic beads, hence requiring pre-tagging of other particles and have low spatial selectivity owing to the low steepness of the trap.

These limitations can be overcome by using selective acoustical tweezers [198], the acoustical analogue of optical tweezers. Indeed, since the first theoretical and experimental demonstration of 3D selective trapping of a particle at the core of a focused acoustical vortex [85], it has been successively demonstrated, that acoustical tweezers (i) can safely and selectively manipulate individual cells [103] with forces of the order of 200 pN (ii) can operate in vivo [199, 200] or through complex opaque media such as the skull [201, 86] and (iii) can trap a variety of objects ranging from various microparticles [84, 85], to cells [103] and bubbles [202].

Yet, these recent developments have long been hindered by the following paradox: On the one hand, spatial selectivity; the ability to manipulate one particle independently of its neighbors, and 3D trapping capability require (i) spatial localization and hence focusing of the acoustic energy to only affect the target particle and (ii) strong axial gradients to overcome axial scattering forces. But on the other hand, 3D selective trapping of micro-objects denser and stiffer than the surrounding medium cannot be achieved with a focused beam as in optics [203]. Indeed, this type of particles are generally expelled from the focal point of a focused beam, and only 2D trapping can be achieved close to some resonance of the trapped particle [203]. As we have seen previously, this paradox can be solved by using some specific beam structures called focused acoustical vortices [204].

Reducing the spatial dimensions of the acoustical vortex is mandatory to extend the capabilities of acoustical tweezers to smaller and smaller particles with increased selectivity and trapping forces, since these two last parameters strongly rely on the size of the vortex compared to the size of the particle [103]. Indeed, the vortex ring is repulsive for surrounding particles. Hence high selectivity can only be achieved when the vortex ring has a size close to the particle size. And since the force applied on the particle depends on the gradient of the acoustic field, strong forces on small objects can only be obtained at high frequencies.

Until now we were able to synthesize 5 MHz and then 40 MHz acoustical vortices (using spiraling interdigitated transducers to synthesize cylindrical and then focused acoustical vortices [105, 103]) to trap micro-particles and cells respectively. In theory this technique could be extended to higher frequency, since it has been demonstrated that it is possible to synthesize surface acoustic waves with IDTs up to several hundred MHz [205] and even GHz frequency [206]. Nevertheless, this frequency increase is a challenging task since (i) the resolution required to achieve such high frequency approaches the limit of classical photo-lithographic techniques, (ii) these high frequency waves are extremely sensitive to all the interfaces that they encounter and (iii) even the measurement of acoustical vortices at these time and spatial scales becomes a major challenge.

In this chapter, a 250 MHz acoustical vortex with a central ring of spatial extension $9\mu m$ in radius synthesized with a spiraling IDT and characterized with a high frequency laser doppler vibrometer is presented. With this tweezer the selective manipulation of some 4 μm in radius glass beads with forces in the NanoNewton range is demonstrated, with conditions (temperature) compatible with biological manipulations. Physical understanding of the vortex synthesis is achieved with the numerical code introduced in Chapter 3 combining finite element (FEM) direct numerical simulation of the wave synthesis system and angular spectrum (AS) propagation of both longitudinal and tangential waves in the solid. This mixed FEM/AM method enables to treat this high frequency complex problem with a reasonable simulation time.

5.2 Method

5.2.1 Tweezers fabrication

The ultra-high frequency tweezers are fabricated using the exact same steps used to fabricate the 40 MHz tweezers used in chapter 4. The spiraling metallic electrodes are deposited on top of a 0.5 mm thick, 3 inches, Y-36 lithium niobate piezoelectric substrate (see sketch on Figure 5.1). A glass wafer of borosilicate D263 T (PGO Online) with a diameter of 56.8 mm and a thickness of 1.1 mm is glued on the top of the piezoelectric substrate using optically transparent epoxy glue (EPOTEK 301-2) to ensure the vortex focalization before the wave reaches the manipulation chamber. The shape of the spiraling electrodes are designed by using the equations (2.1) and (2.2) (provided in [105]) and the code provided in [103] with the following parameters: driving frequency of 240 MHz, 30 turns, transverse wave speed $c_t = 3280ms^{-1}$ and focal point corresponding to the top of the glass wafer + the thickness of the microscope slide.

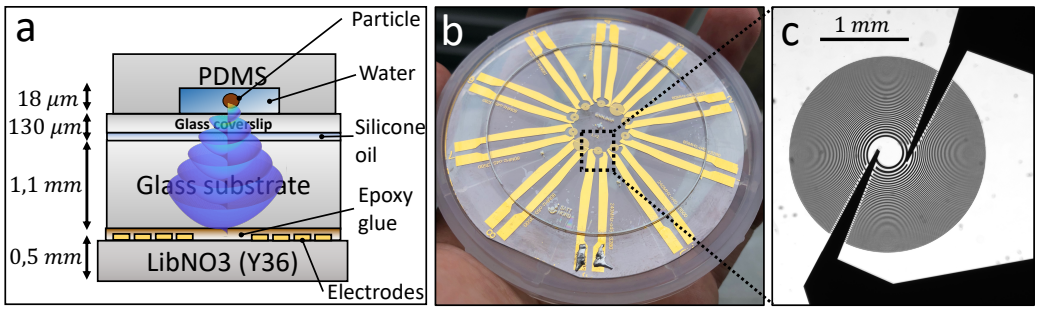

Figure 5.1: a. Sectional sketch representing the different layers constituting an acoustical tweezers. b. Picture of a set of ten acoustical tweezers designed on top of a 3 inch Y36 Niobate Lithium wafer. c. Microscope view of the spiraling electrodes of the 250 MHz acoustical tweezers fabricated for this work.

5.2.2 Tweezers characterization

Once the tweezers are fabricated, optical characterization of the vortex synthesized at the surface of the coverslip – which supports the PDMS microfluidics chamber – is carried out with a Polytec UHF-120 Laser Doppler Vibrometer (LDV) (see Figure 5.6). The acoustic tweezers covered with a 125 μm microscopic glass slide acoustically coupled with the glass slide with a drop of silicone oil (25 cSt) was mounted on the LDV's motorized stage, allowing displacements in the 50 x 50 mm range with a 0.3 μm resolution.

The LDV performs spatial acoustic field scanning in point-by-point mode; a scan grid contained a total of 1599 (39 x 41) points and with a 2.4 x 2.4 μm X-Y resolution. A Mitutoyo M Plan Apo 100x objective was used during the measurements. The 100x magnification ratio of this objective allows obtaining a 0.5 μm laser spot size and a 0.6 μm field depth, which ensures an accurate acquisition of the spatial field distribution. In order to obtain data in a wide frequency range of interest, the tweezers were excited with wave packets linearly swept from 220 to 270 MHz during 200 μs and a repetition period of 10 ms. These signals were amplified with an Amplifier Research 50W/1000A at a gain that provided 35 W of electrical power on a 50 Ohm load. Note that these high power are only used for the tweezers characterization to obtain a good signal-to-noise ratio and since in this case the tweezers are only activated 2% of the time.

5.2.3 Particle manipulation

The manipulation procedure is similar to the one of the previous chapter: A drop of silica particles suspension 4 μm in radius) to be manipulated is pipetted onto the 125 μm thick glass cover-slip and covered with a 18 μm deep polydimethylsiloxane (PDMS) microfluidic chamber (see Figure 5.1.a and 5.2.b). This cover-slip is acoustically coupled to the tweezers with a drop of 25 cT silicone oil which enables relative motion of the cover-slip compared to the tweezers. This motion is achieved with a high precision (100 nm) XY Thorlabs PLS-XY motorized stage (see Figure 5.2.a), which moves a rigid plexi glass frame glued to the glass cover-slip. The whole setup is integrated into a Nikon Ti2E microscope which enables visualization and recording of the particle displacement with a sCMOS Back Illuminated Prime-BSI photo-metrics camera at 40 fps. The tweezers are activated with a IFR 2023 A frequency generator driven at 252 MHz, whose signal is amplified with a AR50A250 150 W amplifier. The optimal activation frequency was determined using the characterization described in the previous section. The manipulation sequence is the following: (i) the particle to be manipulated is placed at the center of the markers localizing the vortex center by moving the microfluidic chamber with the motorized stage, (ii) the tweezers is activated with the electronics and (iii) the particle is moved with the motorized stage. Finally (iv) the particle is released at the target position by switching off the tweezers.

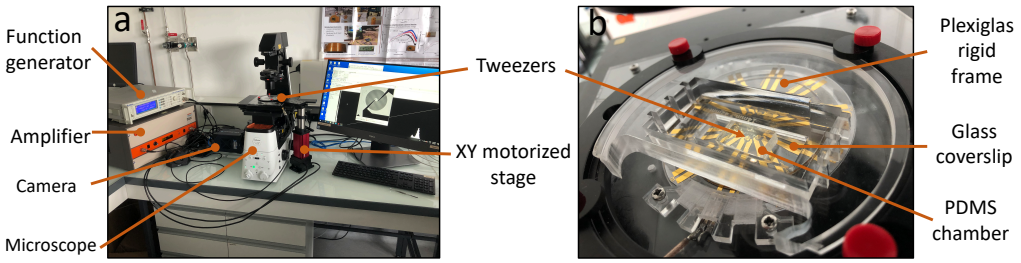

Figure 5.2: a. Picture showing the whole manipulation setup integrated in a Nikon Ti2E microscope. b. Zoom on the microfluidic chamber positioned on top of the acoustical tweezers with the rigid support used for the displacement of the chamber relative to the tweezers.

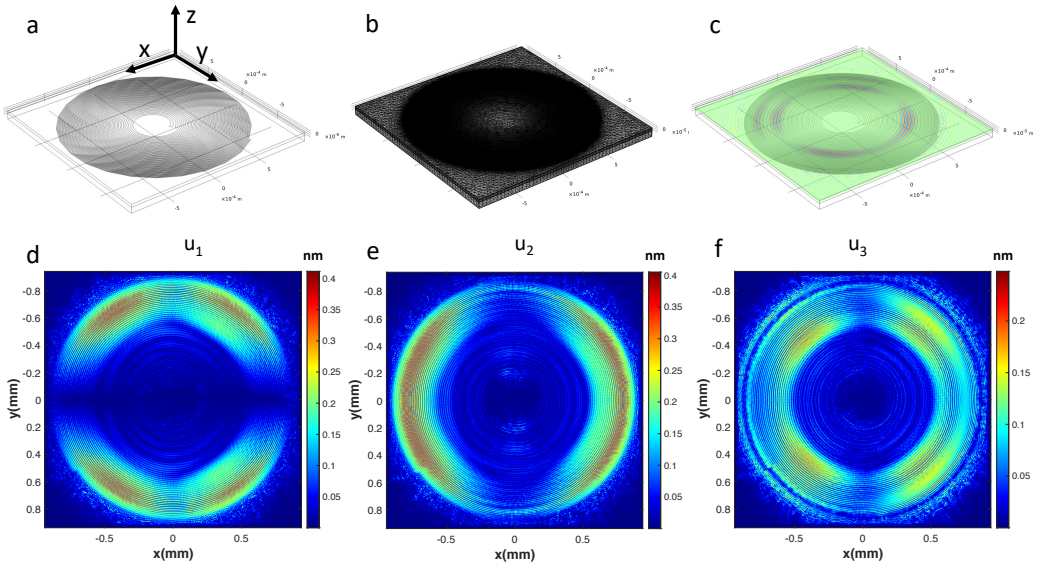

Figure 5.3: Finite Element (FEM) simulation of the wave synthesis. a. Geometry of the electrodes used for the simulations. b. Mesh used for the simulations. c. Real part of the normal displacement at the top of the piezoelectric substrate. d.e.f. Amplitude of the projections of the displacement field u_1, u_2 and u_3 over x, y and z directions respectively at the bottom of the glass substrate.

5.2.4 Simulations

To gain further insight of the active hologram wave synthesis physics, some simulations were performed with the mixed method introduced in chapter 3, combining: (i) a finite element (FEM) direct numerical simulation of the piezoelectric source, (ii) an angular spectrum (AS) technique propagating both longitudinal and tangential waves produced by the source in the glass slide and cover-slip and then the longitudinal wave in the fluid contained in the microfluidic chamber, (iii) a proper use of transmission coefficient at each interface, and finally (iv) some perfectly matched layer to reduce the computation domain. This method enables to treat this 3D high frequency complex problem – which would be hardly tractable with direct numerical simulation of the complete problem – with a reasonable simulation time.

The geometry of the electrodes used for the simulations, the mesh and the real part of the resulting vertical displacement u_3 are shown on Figure 5.3 a, b and c respectively. The displacement obtained by the finite element simulation is decomposed into (i) a shear horizontal (SH) wave whose displacement is horizontal (parallel to the piezo/glass and glass/water interfaces), (ii) a shear vertical (SV) wave and (iii) a longitudinal wave on the other hand. Since SH waves are transmitted in water only to a very thin viscous boundary layer of the order of $\delta_v = \sqrt{\mu \rho f} \sim 64$ nm, with μ the fluid viscosity, ρ the fluid density and f the frequency, they are not further considered in the fluid. The SH, SV and longitudinal waves are propagated to the interface between the glass layer and the water using the angular spectrum technique. The SV and longitudinal waves are then multiplied by the corresponding solid/fluid transmission coefficient to obtain the pressure in the fluid at the interface between the glass layer and the water. The pressure in the water is finally propagated in the thin fluid layer using also the angular spectrum technique. More details about the simulation method can be found in chapter 3.

5.3 Results and discussion

5.3.1 Vortex synthesis physics: numerical simulations and experiments

The results of the simulations performed with the mixed FEM/AS code are presented on Figures 5.3, 5.4 and 5.5. Figure 5.3 d, e, f represent the FEM simulated amplitude of the displacement u_1, u_2 (in the x and y direction respectively) and the normal displacement u_3 (in the z direction) in the glass

resulting from the activation of the electrodes. This figure shows a certain

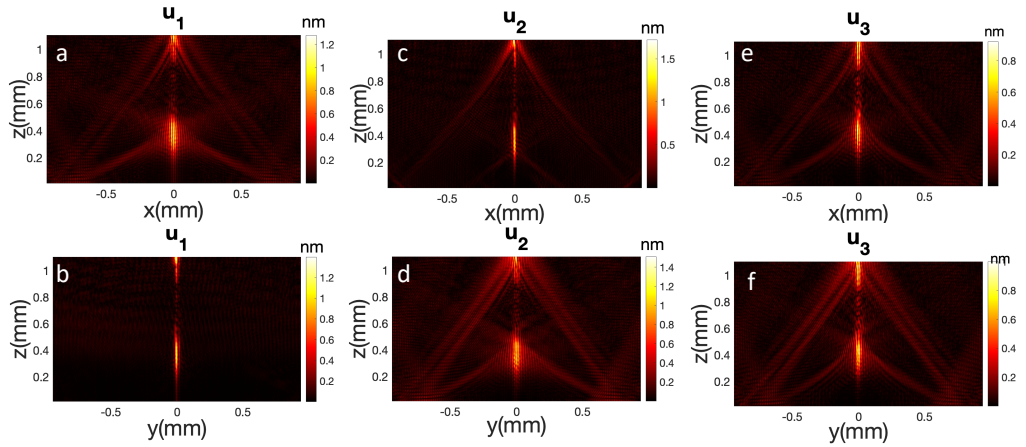

Figure 5.4: FEM/AS simulation of the propagation of the three components of the displacements displacement field u_1, u_2 and u_3 (in the x, y and z directions respectively) in the glass substrate and cover-slip. The figure shows two focal points: one in the middle of the glass and one at the top of the cover-slip.

anisotropy and in-homogeneity of the amplitude of the normal field in the glass u_3, resulting from the activation of the electrodes, while glass is an isotropic homogeneous medium. This anisotropy might be thought as the result from the anisotropy of the electromechanical coupling coefficients of the $LiNbO_3$ in the different directions. But other simulations (chapter 3) performed with a system wherein the electrodes radiate their signal directly in water, or in a glass with a strongly different wave speed exhibit a much weaker anisotropy. Hence a possible explanation of this anisotropy might be the existence of specific interface modes appearing at the interface between the $LiNbO_3$ and the glass due to the proximity of the waves speed in the Lithium Nioate and glass, which, in some specific conditions (orientation, electrodes distance) could lead to some local amplification of the produced signal. Figure 5.4 shows the propagation of the signal (three components of the displacement u_1, u_2, u_3) produced at the bottom of the glass substrate up to the upper surface of the glass cover-slip. In these simulations the coupling silicon oil layer is not considered. The simulations exhibit two focal points resulting from the activation of the electrodes : one at the top of the glass substrate, which is used in the experiments to manipulate the particles, and one in the middle of the glass substrate. The existence of these two focal points is the result of the excitation of both transverse and longitudinal waves in the glass. Indeed, the shape of the electrodes was calculated to obtain the focalization of a transverse focused vortex at the top of the glass

substrate. But some longitudinal waves can also be produced. Indeed, (i) we demonstrated recently [103] that with the same electrodes, it is also possible to generate longitudinal waves with a focal point located at the top of the glass substrate, if it is actuated at a frequency $f_l = c_l/c_t f_t$, where f_l is the activation frequency for longitudinal vortex, f_t the actuation frequency for the transverse vortex, c_l is the longitudinal wave speed and c_t is the transverse wave speed and $c_l/c_t \sim 1.6$. But here the activation frequency is f_t. (ii) In another recent paper [207], we demonstrated that the position of the focal point of a focused vortex generated by an active spiraling transducer, can be moved axially by tuning the excitation frequency. In particular if the frequency is reduced the focal point is moved downward closer to the source. This is exactly what is observed on Figure 5.4. If the electrodes had been activated at $f_l = c_l/c_t f_t$, the longitudinal wave would have focused at the top of the glass cover-slip. But since a much lower activation frequency f_t is used, the focal point of the longitudinal wave is moved downward inside the glass. We can note however that this longitudinal wave plays a minor role on the manipulation device. Indeed, after the focal point, the longitudinal waves diverges and will be scattered inside the glass, resulting into incoherent waves. The magnitude of this incoherent wave will remain weak compared to the intensity of the coherent transverse wave which impacts the upper surface of the glass and is used for the particle manipulation. It nevertheless can result in some noise, as observed in the experimental measurements (Figure 5.6 a and b). Figure 5.5 shows the normal displacement (amplitude, phase, amplitude square) expected at the surface of the glass from the FEM/AS code and inside the water contained in the microfluidic chamber. As expected the normal displacement and pressure fields are very similar since only the normal displacement is transmitted to the fluid. The simulated vortex shows a certain degree of anisotropy, which simply results from the anisotropy observed just above the electrodes. Finally, Figure 5.6, shows the signal measured with the high frequency doppler vibrometer. This figure confirms the synthesis of the high frequency vortex, with an amplitude and phase close to the predictions of the simulations, with a trap size (radius of the first ring) of the order of $9\,\mu m$.

5.3.2 Particle displacement: Selectivity and NanoNewton force

The ability of these high frequency tweezers to manipulate some $4\ \mu m$ silica beds was then investigated. Figure 5.7 illustrates the precision and selectivity of the tweezers: (i) a particle is selected and moved precisely around another

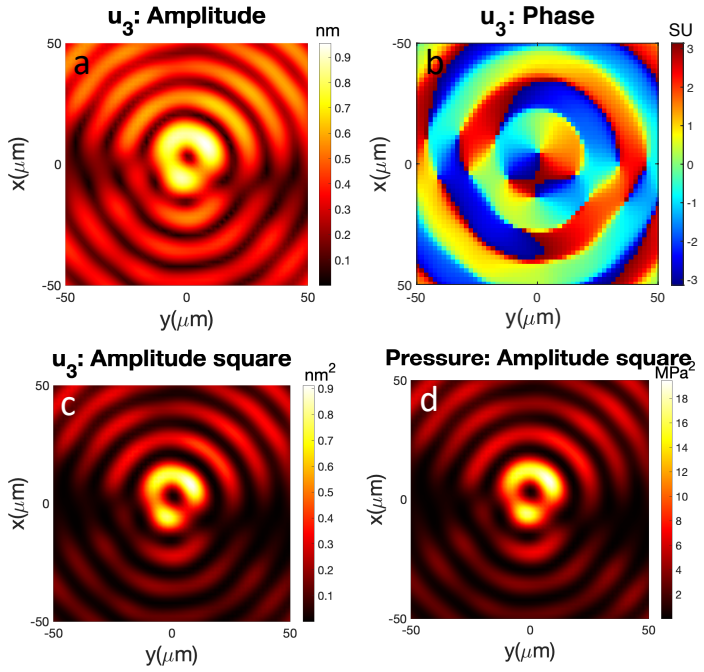

Figure 5.5: FEM/AS simulation of the wave-field in the focal plane. a. Amplitude, b. phase and c. amplitude square of the normal displacement u_3 at the top of the cover-slip. d. Pressure field in the fluid just above the cover-slip.

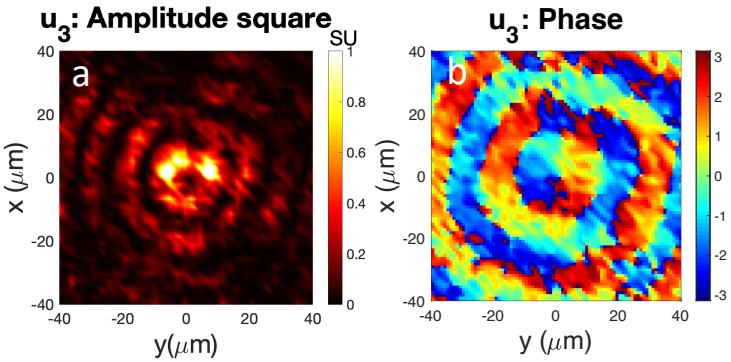

Figure 5.6: Experimental measurement with a laser doppler vibrometer of the normal displacement at the top of the coverslip. a. Normalized amplitude square and b. phase of the normal displacement u_3.

reference particle to form a rectangle and then the reference particle is moved to show that particles can be selectively picked up and moved independently. In the experiments, we can notice a slight adherence of some of the particles,

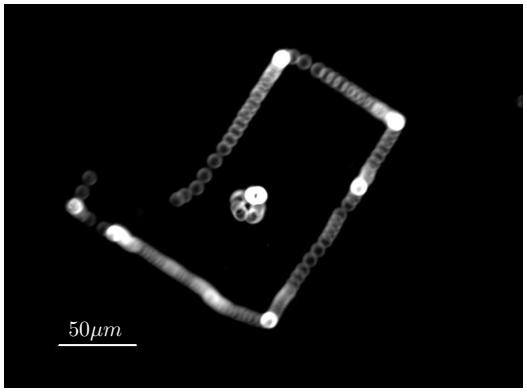

Figure 5.7: Figure illustrating the precision of the displacement of a trapped particle around a reference particle to form a rectangle. Note that in the experiments, the particle which moves is the particle at the center of the rectangle and the the reference particle is the one that forms the rectangle. Indeed, in the experiments the tweezers and hence the center of the trap remains fixed, and the cover-slip is moved comparatively to the tweezers. In the treatment of the data, obtained by standard deviation of the superposition of the stack of images shot by the camera, only the trapped particle and reference particles, are kept, the other particles are erased.

especially when the particles are introduced in the channel several minutes before the manipulation. We can note in Figure 5.7 that when the particle executes the fourth side of the rectangle, it sometimes escapes from the trap and moves on the first dark ring before coming back to the center of the trap. This is only observed when the particle is moved in one specific direction. This is consistent with the anisotropy of the amplitude of the first ring observed both in the simulations (Figure 5.5 c and d) and experiments (Figure 5.6 a), which create some weakness in the first ring wherein the amplitude of the wave, and hence the force of the trap, is weaker. Finally we conducted some experiments to measure the trapping force of these ultra-high frequency tweezers. A particle is trapped and accelerated until the particle escapes from the trap. A maximum translation speed of 11 mms^{-1} inside a 18μm height channel was measured when the particle reached the edge of the micro-chamber. The calculation of the force with Faxen's formula gives an estimation of the force of 1.4 nN. Note that the particle is lost because it reaches the edge of the chamber and not because the stokes drag made it escape from the trap. Hence, 1.4 nN constitutes a lower bound for the value of the trapping force. Note also that all the experiments were performed with driving signals leading to temperature increase of less than 1°C during

the manipulation, some conditions that remain compatible with biological manipulations.

5.4 Conclusion

In this chapter, we demonstrate that it is to possible to design some ultra-high frequency selective tweezers by using some active spiraling holograms patterned at the surface of a piezoelectric substrate. The signal generated at the bottom of a microfluidic chamber is characterized with a laser doppler vibrometer and successfully compared to some numerical predictions obtained with a mixed FEM/AS code, which enables the computation of this ultra high frequency problem with a reasonable computation time. With these tweezers it is demonstrated that $4\mu m$ particles can be picked up and moved selectively with forces in the NanoNewton range. In future work, it would be interesting to investigate (i) ways to reduce the anisotropy of the vortex and obtain a more homogeneous trap and (ii) to further optimize the piezoelectric material (e.g. the $LiNbO_3$ cut) to see whether it is possible to create signals of higher intensity with the same input power, e.g. by increasing the synthesis of the transverse wave and reducing the synthesis of longitudinal waves.

Chapter 6

Toward 3D manipulation of micrometric particles with acoustical tweezers based on spiraling interdigitated transducers

Abstract

As demonstrated in the previous chapters, the selective manipulation of micro-particles and cells can be achieved using holographic acoustical tweezers based on Archimedes-Fermat spiraling interdigitated transducers (S-IDTs). These active holograms have the ability to produce a focused vortex beam, and trap the particle at the vortex core. Yet, all the studies conducted so far with S-IDTs were conducted in 2D owing to the small depth of the microchannels. In this chapter we investigate the 3D manipulation capabilities of S-IDT based tweezers. At first we give a brief overview of some numerical results obtained by other members of the team and published in [208] showing that (i) a 3D radiation trap can be obtained with spiraling tweezers with sufficiently large aperture, (ii) that by tuning the driving frequency, the trap can be displaced axially without any motion of the transducer. Then we introduce the experimental results obtained during this PhD showing that (i) it is indeed possible to create a 3D focused vortex with a S-IDT based transducer and (ii) that its center can be moved according to the predictions by switching the actuation frequency. This work opens perspectives for 3D micro-particles and cells manipulation with single-beam acoustical tweezers.

6.1 Introduction

The 3D trapping of a particle with a single beam, i.e. with a beam coming from only one direction of the space is a complex task to achieve. Indeed, particles tend to be pushed by the radiation pressure in the direction of propagation of the beam. Hence, while it is easy to obtain an axial trap by adding a reflector or an opposite transducer to create a standing wave, achieving a 3D trap with a single beam requires the use of specifically designed beams. Baresch et al. [11, 4] were the first to propose theoretically and demonstrate experimentally the 3D trapping of a particle against gravity and against acoustic streaming by using acoustical vortices. Nevertheless, these experiments were performed at low frequency (1.15 MHz) with a complex array of transducers that is expensive, frequency limited and hardly miniaturizable. Hence these types of systems are not adapted to trap smaller particles of micrometric size. As discussed in the previous chapter, S-IDTS enable the synthesis of 3D-focused acoustical vortices up to very high frequencies. But so far, only 2D trapping capabilities [13, 14] of these tweezers in microchannels of small depth had been explored. In this chapter, we investigate the ability of S-IDT based tweezers to trap and manipulate objects in 3D. In particular, we study how, by switching the frequency, it is possible to move the focal point and hence the trap position.

6.2 Numerical results on 3D particle trapping with fields produced by spiraling sources and axial displacement induced by frequency shift

In this section, we summarize the theoretical work that has been done by Gong et al. [208] and is at the origin of the work conducted in this PhD thesis. Gong et al. demonstrated that the field produced by spiraling sources close to the fields synthesized by S-IDTs have the ability to produce a 3D radiation trap for different types of particles including Pyrex particles and cells. Then they studied the effect of tuning the actuation frequency of the holographic acoustical tweezers on the trapping equilibrium position, while keeping the geometric shapes of the IDTs identical. Indeed, it had been demonstrated that by another team for an airborne system [209] that it was possible to move the focal point of a focused vortex by tuning the excitation frequency. Gong et al. showed indeed that with spiraling sources, the focal plane can be moved toward the source plane, as shown in Figure 6.1a, c and

e, when the excitation frequency is less than f_0 (f = 38MHz < f_0 = 40MHz, Figure 6.1a), and away from it when the excitation frequency is greater than f_0 (f = 42MHz > f_0 = 40MHz, Figure 6.1e).

Moreover, simulations for the radiation force for a Pyrex spherical particle of radius r = 7μm were studied. Figure 6.1b, d and f represents the axial radiation force versus axial position z near the designed focus (z = 0) for the excitation frequencies f = 38, 40, and 42 MHz. They showed that when the frequency is tuned, a 3D trap remains and can be moved axially. For f = 38MHz, the new focal plane is located at $z_1 = -125.4\mu$m and for f = 42MHz, the new focal plane is located at $z_2 = 127.4\mu$m Hence these theoretical re-

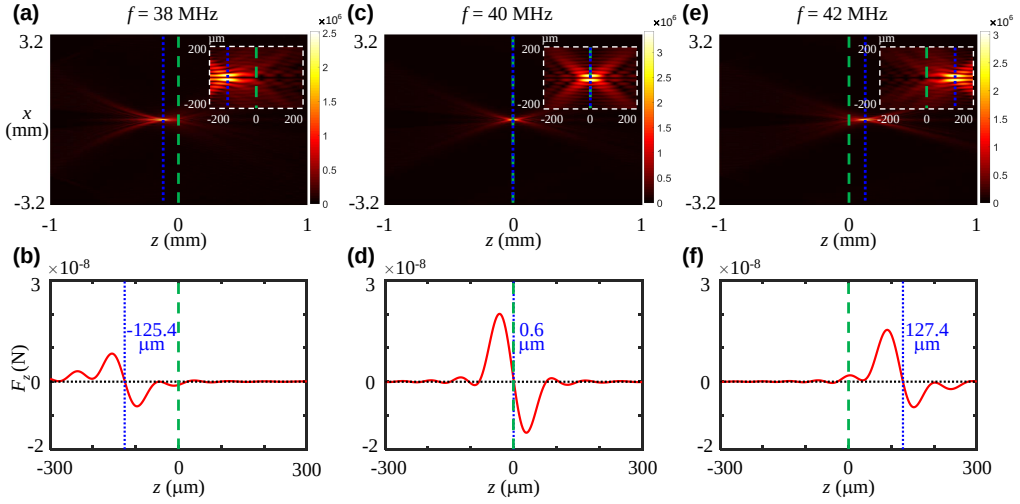

Figure 6.1: The acoustic pressure amplitude in the xz plane for different activated frequencies, a) 38 MHz, b) 40 MHz, c) 42 MHz. The top right corners shows enlarged insets including the focal plane. The axial radiation force with respect to different z positions are shown in b), d), f) for a = 7 μm (in radius) Pyrex particle. The axial equilibrium position is changed with different activated frequencies which leads to a three dimensional trap of the Pyrex particle. The originally designed axial focal position (z = 0) is described by the green dashed line that corresponds to f_0 = 40 MHz, while the actual axial position of the focal plane is indicated by the blue dotted line. When the excitation frequency deviates away from f_0, the effective restoring force decreases.

sults suggested the possibility to trap in 3D and move axially particles by using S-IDT based tweezers and tuning the driving frequency. This is what we aimed at investigating experimentally at the end of this PhD thesis.

6.3 Experimental setup

In the previous chapters, the operations were performed in a narrow microfluidic chamber. Hence a glass slide was glued on top of the piezoelectric substrate in order to focus the wave before it reaches the micro-chamber. Here no glass slide is glued on top of the piezoelectric substrate. Only a thin 2.5 μm of SU-8 2002 photo-resist layer is deposited over the substrate to protect the electrodes and avoid short circuit, except a small part at the end of the electrodes, where the connection takes place. Owing to the small thickness of this layer compared to the wavelength, this layer has a negligible effect on the wave synthesis. As can be seen, on Figure 6.2, different S-IDTs designs were deposited over the substrate to synthesize focused vortices at different frequencies (5, 10, 20 and 40 MHz vortices) and different heights (6, 3, 1.5 and 1.5mm).

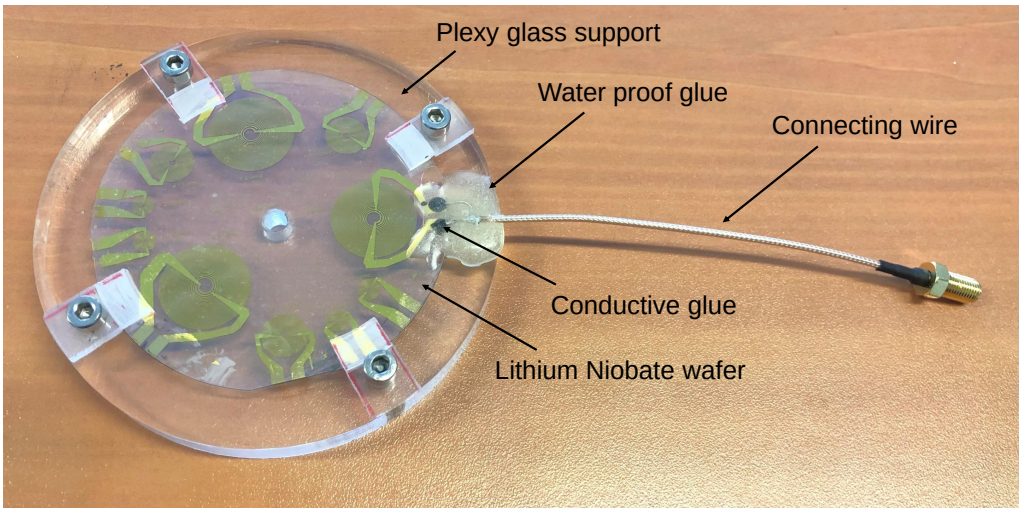

Figure 6.2: 3D acoustical tweezers based on Spiraling Interdigitated Transducers (S-IDTs). The electrodes are connected by a connecting wire (potential is applied to one of the two electrodes, the other being grounded.)

Except from the deposition of this SU8 layer, the fabrication process of this type of tweezers is similar to the one described in the previous chapters. Of course the value of the wave speed in water is used instead of the value of transverse waves in the glass to compute the shape of the electrodes. Note that the connectors are glued to the electrodes with a conductive glue that has a low melting point ($\sim 102^o$C) to prevent any thermal shock to the piezoelectric substrate, which is very sensitive to temperature gradients. Since the

whole transducer will be immersed in water, the connections are protected by water proof glue (Figure 6.2).

The final device hence, consists of (i) spiraling holographic transducers excited with a sinusoidal electrical signal generating an acoustical vortex that propagates and focuses in water, ii) a water tank (Figure 6.3A) wherein the acoustical vortex creates an acoustic field, (iii) a fiber optic hydrophone (Figure 6.3B, D) to detect the acoustical field, (iv) a motorized stage (Figure 6.3A) that enables the X,Y,Z displacement of the tweezer (center of the trap) with respect to the fiber hydrophone (Figure 6.3D), (v) hydrophone holder (Figure 6.3D) to fix the hydrophone inside the water tank.

6.4 Characterization of the acoustical trap

The transducer that is excited at 10MHz driving frequency is designed to be focused at 3.3 mm from the piezoelectric surface. The tweezer is placed in the water tank to start scanning the acoustic field in 3D after activating the tweezer. 60 planes have been scanned with a distance of $40\mu m$ separating each plane, so that we have a 2.4 mm scan distance in the z direction. Where the xy planes are 0.8×0.8 mm with a $10\mu m$ step size. Figure 6.4 shows the comparison between the theoretical predictions and the experimental measurements of the amplitude in the xy and the xz planes and the phase of focal plane at 3.3 mm from the electrodes. Both the amplitude distribution and phase are faithful to the simulations and demonstrate the ability to generate an acoustical vortex. At the focal plane (at 3.3 mm from the electrodes), we find, as expected, a vortex of order 1, as shown in Figure 6.4. The wavefield exhibits a central node (corresponding to the phase central singularity) surrounded by a ring (Figure 6.4D) of high intensity which constitutes the acoustical trap.

In addition, the acoustic field was scanned in 3D at 4 different driving frequencies: 9.5, 9.7, 10.3 and 10.5MHz. It is expected that the focal plane moves toward the source plane in the case of 9.7 and 9.5MHz (9.5MHz being the closest to the source plane), and away from it in the case of 10.3 and 10.5MHz (10.5MHz being the furthest away from the source plane). Figure 6.5 shows the numerical predictions of the amplitude in the yz plane for 10.5, 10.3, 10, 9.7, and 9.5MHz that are obtained from an angular spectrum code. It is clearly seen that as the frequency is increased, the focal plane is shifted away from the source plane and as the frequency is decreased, the focal plane moves closer to the source plane.

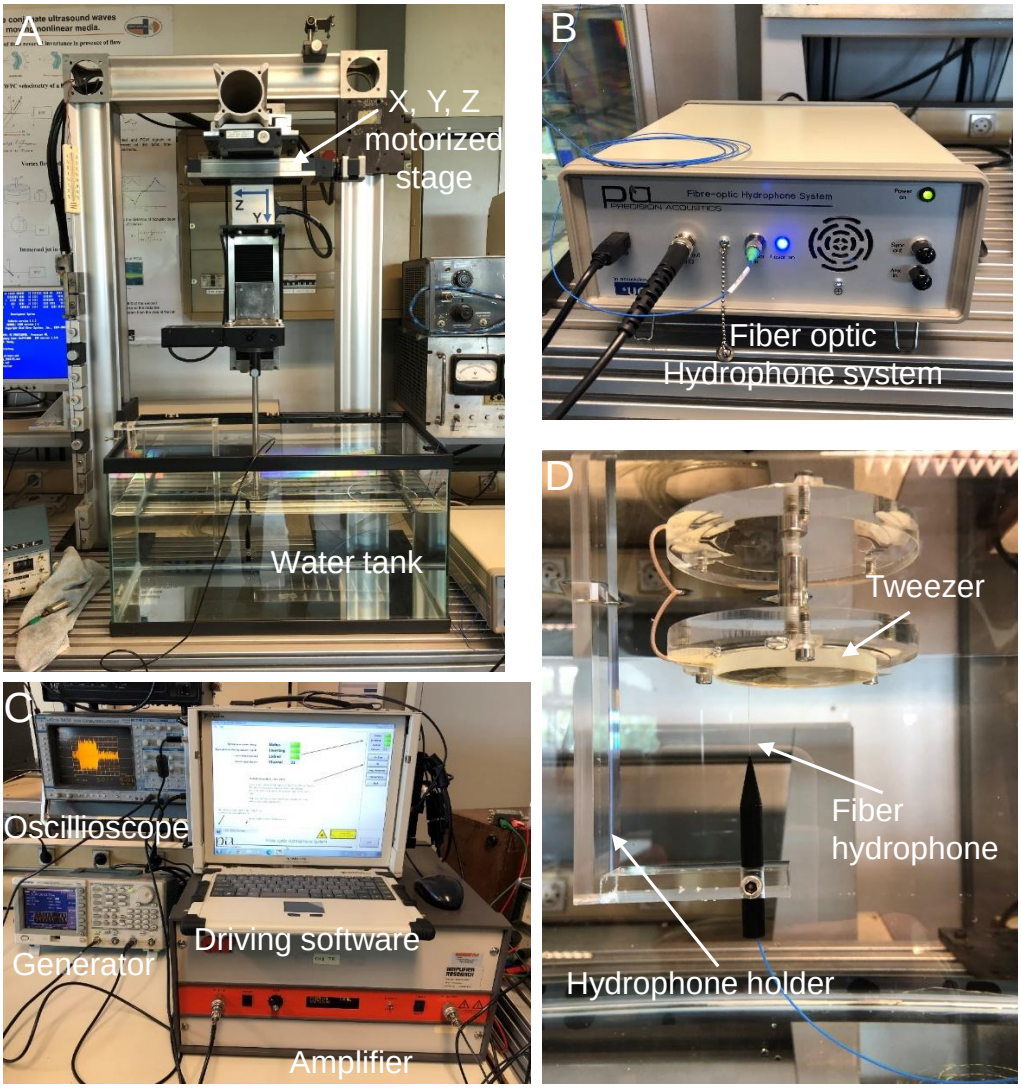

Figure 6.3: Experimental setup. A) Illustration of the integration of the whole setup. B) Fiber optic hydrophone system used in this project. C) Devices used to excite the tweezers (frequency generator (IFR 2023 A) and amplifier (AR50A250 Amplifier 150 W)), and devices used to detect the the signal (oscilloscope and a). D) Zoom on the tweezers and fiber hydrophone.

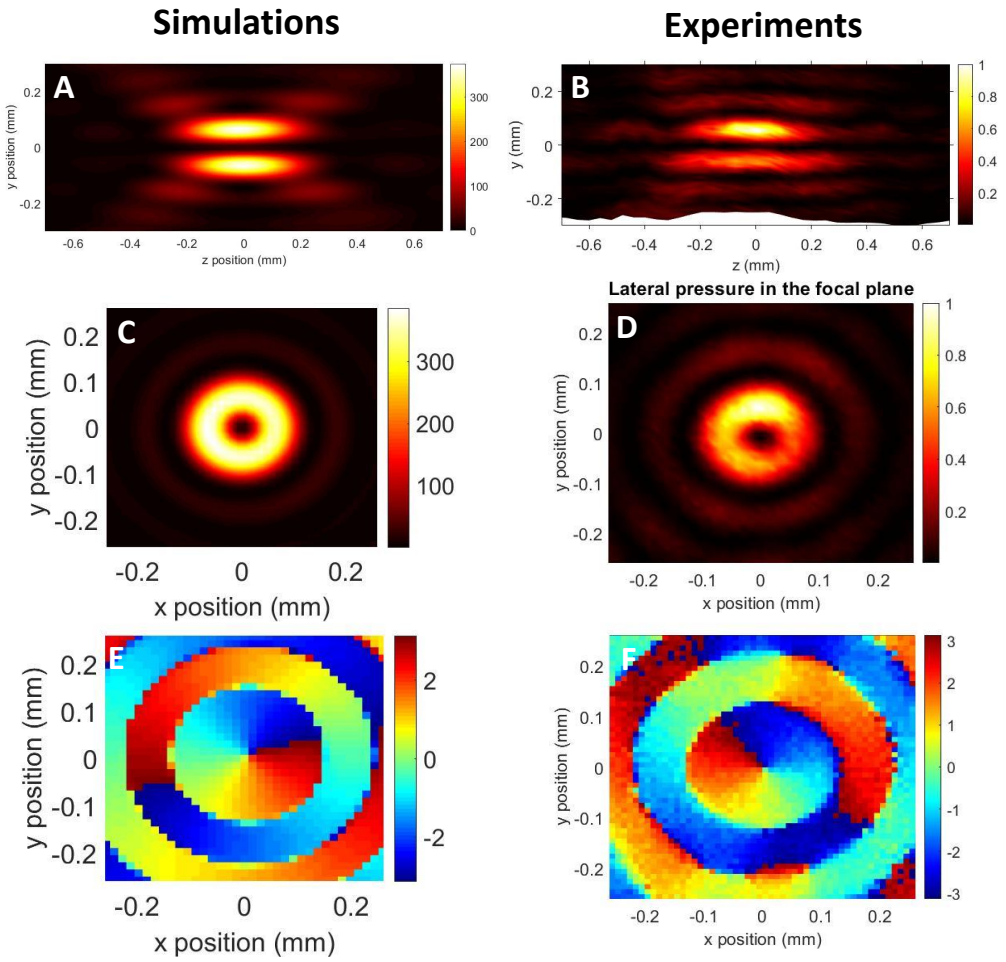

Figure 6.4: Acoustic field of a 10MHz transducer. Comparison between the numerical predictions A, C, E and experimental measurements B, D, F (performed with a fiber optic hydrophone) of the amplitude along the yz plane (A, B), the amplitude in the xy plane (C, D) and the phase (E,F) of the acoustic normal displacement at the focal plane (3.3 mm above the electrodes).

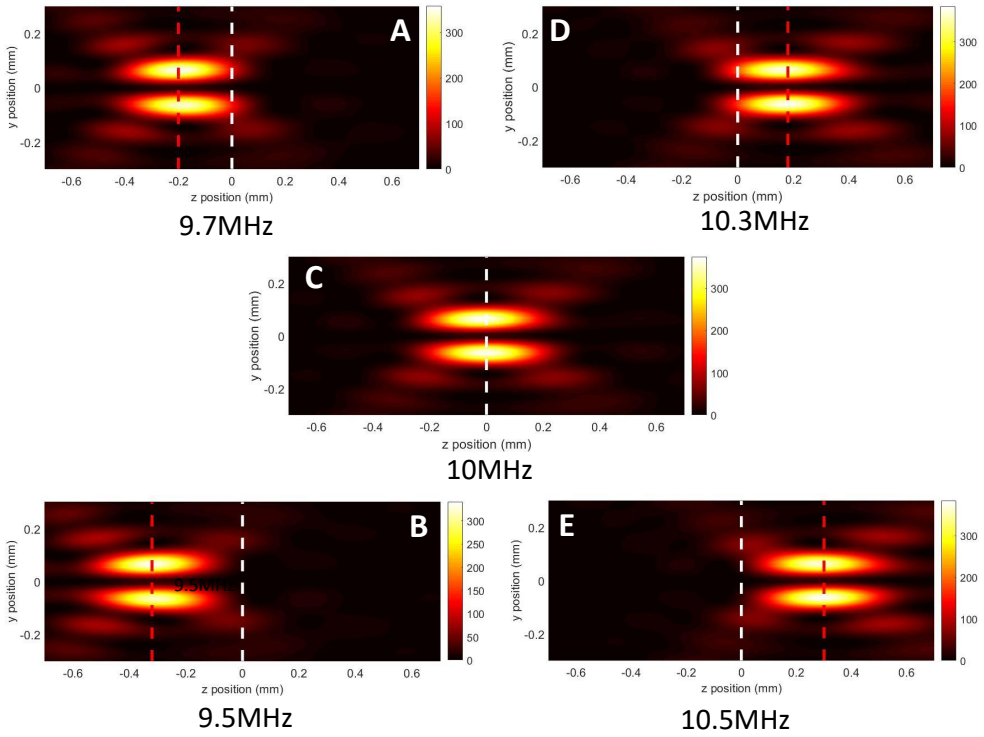

Figure 6.5: Numerical predictions of the amplitude of a transducer designed at 10MHz, propagating in the yz plane for different frequencies. A) 9.7MHz, B) 9.5MHz, C) 10MHZ, D) 10.3MHz, E) 10.5MHz.

Figure 6.6 shows the experimental measurements of the amplitudes along the yz plane for the same frequencies that were taken into consideration in the theoretical study.

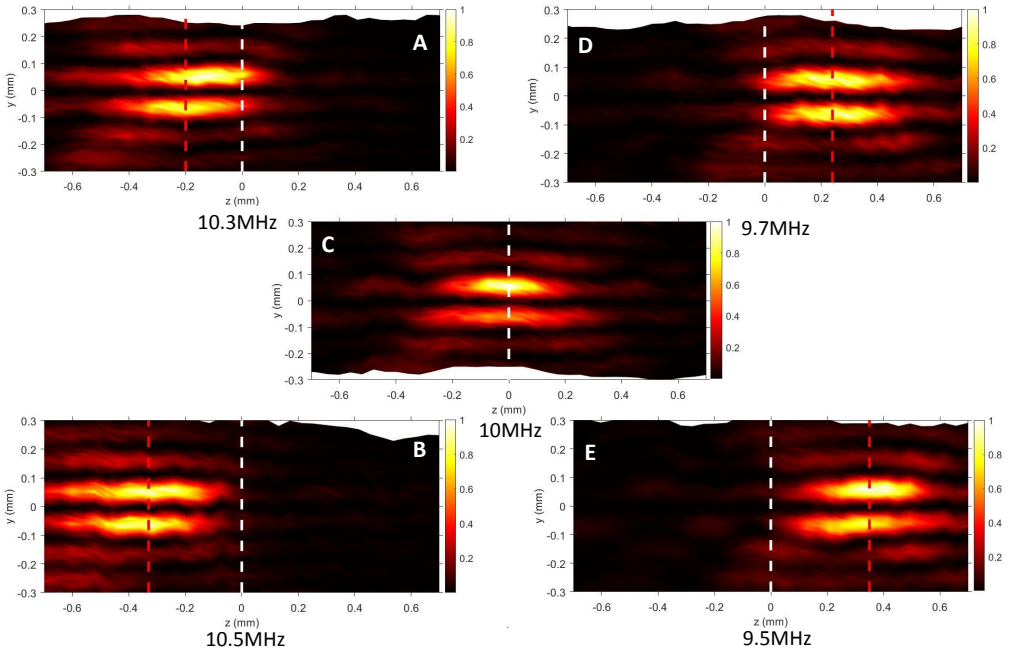

Figure 6.6: Experimental measurements of the amplitude of a transducer designed at 10MHz, propagating in the yz plane for different frequencies. A) 10.3MHz, B) 10.5MHz, C) 10MHZ, D) 9.7MHz, E) 9.5MHz.

The comparison between experimental data and numerics shows a good quantitative agreement both for the topology of the field and the location of the vortex center (see table 6.1 and Figure 6.7).

Frequency	Focal plane location expected	Focal plane location obtained
10.8 MHz	3.78 mm	
10.5 MHz	3.6 mm	3.63 mm
10.3 MHz	3.48 mm	3.5 mm
10 MHz	3.3 mm	3.3 mm
9.7 MHz	3.1 mm	3.06 mm
9.5 MHz	2.98 mm	2.95 mm
9.2 MHz	2.81 mm	

Table 6.1: Theoretical expectations vs experimental measurements of the location of the focal plane away from the source plane for different frequencies.

6.5 Conclusion

In this chapter, we were able to demonstrate that is possible to synthesize a 3D focused vortex with S-IDTs and move axially the position of the focal plane by switching the excitation frequency, in accordance with the numerical predictions. The next steps are (i) to trap a particle at the core of the vortex and demonstrate the 3D displacement of micro-particles with this system and (ii) switch to even higher frequencies, since the main advantage of S-IDT based tweezers is the ability to synthesize high frequency signals. Unfortunately, due to COVID issues, we were not able to perform these experimental measurements in the course of this PhD.

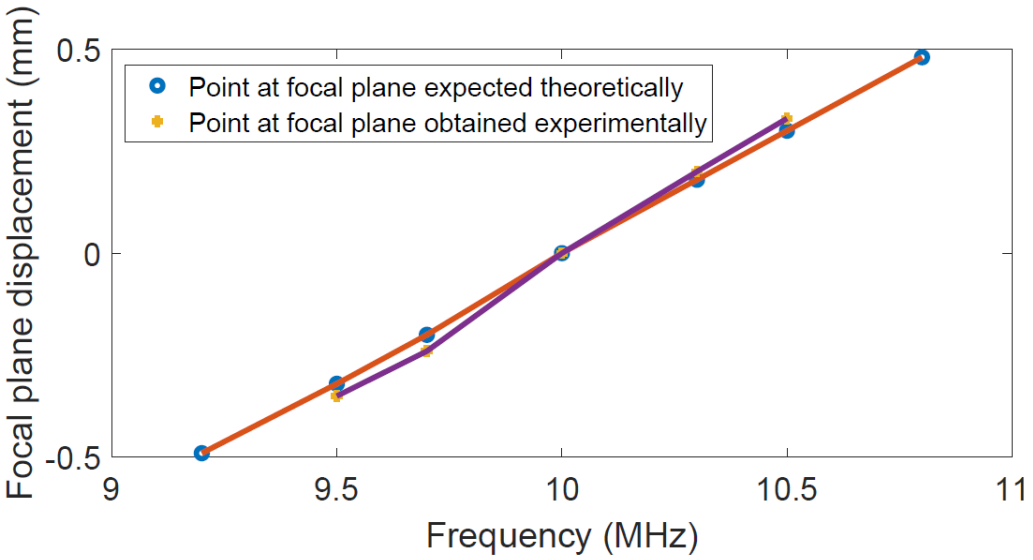

Figure 6.7: Theoretical expectations VS experimental measurements of the displacement of the focal plane with respect to the designed frequency (10MHz) that is focused at 3.3mm away from the source plane.

General conclusion

Acoustic radiation force is a nonlinear effect that can be used in acoustical tweezers to trap and manipulate particles collectively and selectively. Acoustical tweezers overcome many limitations in particle manipulation by comparison to their magnetic and optical counterparts, e.g. overheating of biological samples caused by optical tweezers when large forces are required or limitation in the trap stiffness and type of particles that can be manipulated with magnetic tweezers. Larger forces can be applied in acoustics than in optics at the same wave intensity, since the radiation pressure in optics and in acoustics are proportional to intensity of the wave divided by the speed of the wave, where the speed of light in liquids is five orders of magnitude larger than speed of sound. Moreover, ultrasonic sources are available from kilohertz to gigahertz frequencies that can trap big range of particle sizes (hundreds of nanometers to millimeters).

In acoustics, scientists started trapping particles with devices based on standing waves, wherein particles are trapped at the nodes or anti-nodes depending on the density and compressibility of the particles compared to the surrounding medium. More recently, surface acoustic waves produced by IDTs have been considered to trap smaller particles in microfluidic devices. But tweezers based on standing waves can only trap particles collectively (if there is more than one particle) due to the multiplicity of nodes and antinodes. To achieve selectivity, it is necessary to localize spatially (and hence focus) the energy. The first idea to achieve this goal was to use focused waves as in optics, where the acoustic energy is strongly localized in the area of interest. But most particles of interest (elastic particles and cells) are expelled from the focal point since they are denser and stiffer than the fluid. They are attracted to a pressure minimum instead of a pressure maximum. In addition, trapping particles in 3D using one-sided transducers remained an unsolved challenge.

Spherical acoustical vortices were proposed to solve these issues. These vor-

tices are focused helical waves spinning around a phase singularity. They are characterized by a pressure intensity minimum at the focal point surrounded by a high intensity bright ring that can ensure the trap of a particle. Trapping particles in 3D using one sided wave was demonstrated by Baresch et al. [4], with complex array of transducers. Later on, Baudoin et al. [13] replaced these type devices by active holograms made of spiraling interdigitated transducer. These type of transducers are cheap in fabrication and easily integrated in a microscope.

In this thesis, we first introduced the experimental and numerical methods that were used respectively to fabricate and optimize the spiraling interdigitated transducers. Then we introduced 3 different projects that were conducted in the course of this PhD:

The first project aimed at manipulating selectively human cells with single-beam acoustical tweezers. In this project the selective manipulation of cells and precise positioning of individual cells among a collection in a standard microscopy environment with trapping forces up to 200 pN is demonstrated. In addition, to ensure that there is no impact of the tweezer on cells' integrity, short and long-term viability was investigated using a fluorescent viability assay as post exposure cell observation, where the dead/live cell ratio of the insonified region (where the tweezer is activated) is 3%, while the dead/live cell ratio on the overall device is 5%.

The second project aimed at investigating the ability of these tweezers to synthesize ultra-high frequency (250 MHz) vortices with high spatial selectivity trapping and positioning of 4 microns individual particles with NanoNewton forces is demonstrated in a standard microscopy environment.

The last project aimed at investigating the ability of these tweezers to trap small objects in 3D and move them axially by simply changing the excitation frequency close to the original frequency used for designing the spiraling transducers. In our preliminary experiments, a 10MHz transducer was tested. It has been shown that when the excitation frequency is less than the designed frequency (f = 9.7 MHz and 9.5 MHz) the focal plane is moved toward the source plane, and when the excitation frequency is greater than the designed frequency (f = 10.3 MHz and 10.5 MHz) the focal plane is shifted away from it. In future work, 3D trapping and displacement of particles with these tweezers is envisioned.

During this PhD, we had the opportunity to investigate some of the unique

possibilities offered by active holographic tweezers based on spiraling interdigitated transducers for micro-manipulation of cells and micro-particles. This work opens many perspectives e.g. to investigate force spectroscopy in some domain that were hardly accessible with other techniques, organize precisely different type of cells and study their interaction or perform some complex operations such as In-Vitro Fertilization.

Bibliography

[1] A. Ashkin, J. M. Dziedzic, J. Bjorkholm, and S. Chu, "Observation of a single-beam gradient force optical trap for dielectric particles," *Optics letters*, vol. 11, no. 5, pp. 288–290, 1986.

[2] K. Svoboda and S. M. Block, "Biological applications of optical forces," *Annual review of biophysics and biomolecular structure*, vol. 23, no. 1, pp. 247–285, 1994.

[3] K. C. Neuman and A. Nagy, "Single-molecule force spectroscopy: optical tweezers, magnetic tweezers and atomic force microscopy," *Nature methods*, vol. 5, no. 6, p. 491, 2008.

[4] D. Baresch, J.-L. Thomas, and R. Marchiano, "Observation of a single-beam gradient force acoustical trap for elastic particles: acoustical tweezers," *Physical review letters*, vol. 116, no. 2, p. 024301, 2016.

[5] L. V. King, "On the acoustic radiation pressure on spheres," *Proceedings of the Royal Society of London. Series A-Mathematical and Physical Sciences*, vol. 147, no. 861, pp. 212–240, 1934.

[6] K. Söllner and C. Bondy, "The mechanism of coagulation by ultrasonic waves," *Transactions of the Faraday Society*, vol. 32, pp. 616–623, 1936.

[7] X. Ding, S.-C. S. Lin, B. Kiraly, H. Yue, S. Li, I.-K. Chiang, J. Shi, S. J. Benkovic, and T. J. Huang, "On-chip manipulation of single microparticles, cells, and organisms using surface acoustic waves," *Proceedings of the National Academy of Sciences*, vol. 109, no. 28, pp. 11105–11109, 2012.

[8] S. Tran, P. Marmottant, and P. Thibault, "Fast acoustic tweezers for the two-dimensional manipulation of individual particles in microfluidic channels," *Applied Physics Letters*, vol. 101, no. 11, p. 114103, 2012.

[9] A. Ozcelik, J. Rufo, F. Guo, Y. Gu, P. Li, J. Lata, and T. J. Huang, "Acoustic tweezers for the life sciences," *Nature methods*, vol. 15, no. 12, pp. 1021–1028, 2018.

[10] J. Wu, "Acoustical tweezers," *The Journal of the Acoustical Society of America*, vol. 89, no. 5, pp. 2140–2143, 1991.

[11] D. Baresch, J.-L. Thomas, and R. Marchiano, "Spherical vortex beams of high radial degree for enhanced single-beam tweezers," *Journal of Applied Physics*, vol. 113, no. 18, p. 184901, 2013.

[12] B. T. Hefner and P. L. Marston, "An acoustical helicoidal wave transducer with applications for the alignment of ultrasonic and underwater systems," *The Journal of the Acoustical Society of America*, vol. 106, no. 6, pp. 3313–3316, 1999.

[13] M. Baudoin, J.-C. Gerbedoen, A. Riaud, O. B. Matar, N. Smagin, and J.-L. Thomas, "Folding a focalized acoustical vortex on a flat holographic transducer: miniaturized selective acoustical tweezers," *Science advances*, vol. 5, no. 4, p. eaav1967, 2019.

[14] M. Baudoin, J.-L. Thomas, R. Al Sahely, J.-C. Gerbedoen, Z. Gong, A. Sivery, O. B. Matar, N. Smagin, P. Favreau, and A. Vlandas, "Spatially selective manipulation of cells with single-beam acoustical tweezers," *Nature communications*, vol. 11, no. 1, pp. 1–10, 2020.

[15] I. De Vlaminck and C. Dekker, "Recent advances in magnetic tweezers," *Annual review of biophysics*, vol. 41, pp. 453–472, 2012.

[16] J. Yan, D. Skoko, and J. F. Marko, "Near-field-magnetic-tweezer manipulation of single dna molecules," *Physical Review E*, vol. 70, no. 1, p. 011905, 2004.

[17] J. K. Fisher, J. Cribb, K. V. Desai, L. Vicci, B. Wilde, K. Keller, R. M. Taylor, J. Haase, K. Bloom, E. T. O'Brien, *et al.*, "Thin-foil magnetic force system for high-numerical-aperture microscopy," *Review of Scientific Instruments*, vol. 77, no. 2, p. 023702, 2006.

[18] C. Gosse and V. Croquette, "Magnetic tweezers: micromanipulation and force measurement at the molecular level," *Biophysical journal*, vol. 82, no. 6, pp. 3314–3329, 2002.

[19] P. Kollmannsberger and B. Fabry, "Bahigh-force magnetic tweezers with force feedback for biological applications," *Review of Scientific Instruments*, vol. 78, no. 11, p. 114301, 2007.

[20] D. G. Grier, "A revolution in optical manipulation," *nature*, vol. 424, no. 6950, pp. 810–816, 2003.

[21] A. Ashkin and J. M. Dziedzic, "Optical trapping and manipulation of viruses and bacteria," *Science*, vol. 235, no. 4795, pp. 1517–1520, 1987.

[22] H. Zhang and K.-K. Liu, "Optical tweezers for single cells," *Journal of The Royal Society Interface*, vol. 5, no. 24, pp. 671–690, 2008.

[23] `https://www.thorlabs.com/newgrouppage9.cfm?objectgroup_id=10774`.

[24] M. B. Rasmussen, L. B. Oddershede, and H. Siegumfeldt, "Optical tweezers cause physiological damage to escherichia coli and listeria bacteria," *Appl. Environ. Microbiol.*, vol. 74, no. 8, pp. 2441–2446, 2008.

[25] G. Leitz, E. Fällman, S. Tuck, and O. Axner, "Stress response in caenorhabditis elegans caused by optical tweezers: wavelength, power, and time dependence," *Biophysical journal*, vol. 82, no. 4, pp. 2224–2231, 2002.

[26] M. Baudoin and J.-L. Thomas, "Acoustic tweezers for particle and fluid micromanipulation," *Annual Review of Fluid Mechanics*, vol. 52, pp. 205–234, 2020.

[27] T. Laurell, F. Petersson, and A. Nilsson, "Chip integrated strategies for acoustic separation and manipulation of cells and particles," *Chemical Society Reviews*, vol. 36, no. 3, pp. 492–506, 2007.

[28] M. A. Ghanem, A. D. Maxwell, Y.-N. Wang, B. W. Cunitz, V. A. Khokhlova, O. A. Sapozhnikov, and M. R. Bailey, "Noninvasive acoustic manipulation of objects in a living body," *Proceedings of the National Academy of Sciences*, vol. 117, no. 29, pp. 16848–16855, 2020.

[29] M. Faraday, "Xvii. on a peculiar class of acoustical figures; and on certain forms assumed by groups of particles upon vibrating elastic surfaces," *Philosophical transactions of the Royal Society of London*, no. 121, pp. 299–340, 1831.

[30] A. Kundt and O. Lehmann, "Longitudinal vibrations and acoustic figures in cylindrical columns of liquids," *Ann. Phys. Chem*, vol. 153, no. 1, p. 1874, 1874.

[31] J. W. Strutt, "I. on the circulation of air observed in kundt's tubes, and on some allied acoustical problems," *Philosophical Transactions of the Royal Society of London*, no. 175, pp. 1–21, 1884.

[32] C. Eckart, "Vortices and streams caused by sound waves," *Physical review*, vol. 73, no. 1, p. 68, 1948.

[33] J. J. Markham, "Second-order acoustic fields: Streaming with viscosity and relaxation," *Physical Review*, vol. 86, no. 4, p. 497, 1952.

[34] L. P. Gor'kov, "On the forces acting on a small particle in an acoustical field in an ideal fluid," in *Sov. Phys. Dokl.*, vol. 6, pp. 773–775, 1962.

[35] A. P. Sarvazyan, O. V. Rudenko, and W. L. Nyborg, "Biomedical applications of radiation force of ultrasound: historical roots and physical basis," *Ultrasound in medicine & biology*, vol. 36, no. 9, pp. 1379–1394, 2010.

[36] A. A. Doinikov, "Acoustic radiation forces: Classical theory and recent advances," *Recent research developments in acoustics*, vol. 1, pp. 39–67, 2003.

[37] K. Yosioka and Y. Kawasima, "Acoustic radiation pressure on a compressible sphere," *Acta Acustica United with Acustica*, vol. 5, no. 3, pp. 167–173, 1955.

[38] H. Bruus, *Theoretical microfluidics*, vol. 18. Oxford university press Oxford, 2008.

[39] L. Andersen, A. Nysteen, and M. Settnes, "Forces acting on microparticles in acoustofluidic systems," *Bachelor thesis,(Technical University of Denmark), Denmark*, 2009.

[40] G. Silva, T. Lobo, and F. Mitri, "Radiation torque produced by an arbitrary acoustic wave," *EPL (Europhysics Letters)*, vol. 97, no. 5, p. 54003, 2012.

[41] O. A. Sapozhnikov and M. R. Bailey, "Radiation force of an arbitrary acoustic beam on an elastic sphere in a fluid," *The Journal of the Acoustical Society of America*, vol. 133, no. 2, pp. 661–676, 2013.

[42] D. Baresch, J.-L. Thomas, and R. Marchiano, "Three-dimensional acoustic radiation force on an arbitrarily located elastic sphere," *The Journal of the Acoustical Society of America*, vol. 133, no. 1, pp. 25–36, 2013.

[43] Z. Gong and M. Baudoin, "Acoustic radiation torque on a particle in a fluid: An angular spectrum based compact expression," *The Journal of the Acoustical Society of America*, vol. 148, no. 5, pp. 3131–3140, 2020.

[44] Z. I. Mandralis and D. L. Feke, "Fractionation of suspensions using synchronized ultrasonic and flow fields," *AIChE Journal*, vol. 39, no. 2, pp. 197–206, 1993.

[45] D. Bazou, G. A. Foster, J. R. Ralphs, and W. T. Coakley, "Molecular adhesion development in a neural cell monolayer forming in an ultrasound trap," *Molecular membrane biology*, vol. 22, no. 3, pp. 229–240, 2005.

[46] G. Whitworth, M. Grundy, and W. Coakley, "Transport and harvesting of suspended particles using modulated ultrasound," *Ultrasonics*, vol. 29, no. 6, pp. 439–444, 1991.

[47] C. Ratier and M. Hoyos, "Acoustic programming in step-split-flow lateral-transport thin fractionation," *Analytical chemistry*, vol. 82, no. 4, pp. 1318–1325, 2010.

[48] D. Bazou, W. T. Coakley, K. M. Meek, M. Yang, and D. T. Pham, "Characterisation of the morphology of 2-d particle aggregates in different electrolyte concentrations in an ultrasound trap," *Colloids and Surfaces A: Physicochemical and Engineering Aspects*, vol. 243, no. 1-3, pp. 97–104, 2004.

[49] J. J. Hawkes, M. J. Long, W. T. Coakley, and M. B. McDonnell, "Ultrasonic deposition of cells on a surface," *Biosensors and Bioelectronics*, vol. 19, no. 9, pp. 1021–1028, 2004.

[50] C. Ratier, *Étude et réalisation d'un dispositif de séparation acoustique et de son application à des objets biologiques*. PhD thesis, Université Paris-Diderot-Paris VII, 2009.

[51] A. Doinikov and S. Zavtrak, "Radiation forces between two bubbles in a compressible liquid," *The Journal of the Acoustical Society of America*, vol. 102, no. 3, pp. 1424–1431, 1997.

[52] P. L. Marston and D. B. Thiessen, "Manipulation of fluid objects with acoustic radiation pressure," *Annals of the New York Academy of Sciences*, vol. 1027, no. 1, pp. 414–434, 2004.

[53] G. T. Silva, "An expression for the radiation force exerted by an acoustic beam with arbitrary wavefront (l)," *The Journal of the Acoustical Society of America*, vol. 130, no. 6, pp. 3541–3544, 2011.

[54] L. Brillouin, "Les tensions de radiation; leur interprétation en mécanique classique et en relativité," *J. Phys. Radium*, vol. 6, no. 11, pp. 337–353, 1925.

[55] Z. Gong and M. Baudoin, "Equivalence between angular spectrum-based and multipole expansion-based formulas of the acoustic radiation force and torque," *arXiv preprint arXiv:2102.02678*, 2021.

[56] D. Zhao, J.-L. Thomas, and R. Marchiano, "Computation of the radiation force exerted by the acoustic tweezers using pressure field measurements," *The Journal of the Acoustical Society of America*, vol. 146, no. 3, pp. 1650–1660, 2019.

[57] M. Wiklund, R. Green, and M. Ohlin, "Acoustofluidics 14: Applications of acoustic streaming in microfluidic devices," *Lab on a Chip*, vol. 12, no. 14, pp. 2438–2451, 2012.

[58] O. Manneberg, *Multidimensional ultrasonic standing wave manipulation in microfluidic chips*. PhD thesis, KTH, 2009.

[59] M. Evander and J. Nilsson, "Acoustofluidics 20: Applications in acoustic trapping," *Lab on a Chip*, vol. 12, no. 22, pp. 4667–4676, 2012.

[60] P. Augustsson, T. Laurell, and S. Ekström, "Flow-through chip for sequential treatment and analyte elution from beads or cells," in *Twelfth International Conference on Miniaturized Systems for Chemistry and Life Sciences on Micro Total Analysis Systems, San Diego, CA, USA*, pp. 161–163, 2008.

[61] P. Augustsson, J. Persson, S. Ekström, M. Ohlin, and T. Laurell, "Decomplexing biofluids using microchip based acoustophoresis," *Lab on a Chip*, vol. 9, no. 6, pp. 810–818, 2009.

[62] F. Petersson, L. Åberg, A.-M. Swärd-Nilsson, and T. Laurell, "Free flow acoustophoresis: microfluidic-based mode of particle and cell separation," *Analytical chemistry*, vol. 79, no. 14, pp. 5117–5123, 2007.

[63] M. Wiklund, P. Spégel, S. Nilsson, and H. M. Hertz, "Ultrasonic-trap-enhanced selectivity in capillary electrophoresis," *Ultrasonics*, vol. 41, no. 4, pp. 329–333, 2003.

[64] A. Neild, S. Oberti, F. Beyeler, J. Dual, and B. J. Nelson, "A microparticle positioning technique combining an ultrasonic manipulator and a microgripper," *Journal of Micromechanics and Microengineering*, vol. 16, no. 8, p. 1562, 2006.

[65] F. Beyeler, A. Neild, S. Oberti, D. J. Bell, Y. Sun, J. Dual, and B. J. Nelson, "Monolithically fabricated microgripper with integrated force sensor for manipulating microobjects and biological cells aligned in an ultrasonic field," *Journal of microelectromechanical systems*, vol. 16, no. 1, pp. 7–15, 2007.

[66] J. Shi, D. Ahmed, X. Mao, S.-C. S. Lin, A. Lawit, and T. J. Huang, "Acoustic tweezers: patterning cells and microparticles using standing surface acoustic waves (ssaw)," *Lab on a Chip*, vol. 9, no. 20, pp. 2890–2895, 2009.

[67] J. F. Nye and M. V. Berry, "Dislocations in wave trains," *Proceedings of the Royal Society of London. A. Mathematical and Physical Sciences*, vol. 336, no. 1605, pp. 165–190, 1974.

[68] C. R. Courtney, C. E. Demore, H. Wu, A. Grinenko, P. D. Wilcox, S. Cochran, and B. W. Drinkwater, "Independent trapping and manipulation of microparticles using dexterous acoustic tweezers," *Applied Physics Letters*, vol. 104, no. 15, p. 154103, 2014.

[69] M. Baudoin and J.-L. Thomas, "Acoustic tweezers for particle and fluid micromanipulation," *Annual Review of Fluid Mechanics*, vol. 52, 2019.

[70] P. L. Marston, "Axial radiation force of a bessel beam on a sphere and direction reversal of the force," *The Journal of the Acoustical Society of America*, vol. 120, no. 6, pp. 3518–3524, 2006.

[71] P. L. Marston, "Radiation force of a helicoidal bessel beam on a sphere," *The Journal of the Acoustical Society of America*, vol. 125, no. 6, pp. 3539–3547, 2009.

[72] X.-D. Fan and L. Zhang, "Trapping force of acoustical bessel beams on a sphere and stable tractor beams," *Physical Review Applied*, vol. 11, no. 1, p. 014055, 2019.

[73] A. Marzo, S. A. Seah, B. W. Drinkwater, D. R. Sahoo, B. Long, and S. Subramanian, "Holographic acoustic elements for manipulation of levitated objects," *Nature communications*, vol. 6, p. 8661, 2015.

[74] R. Weis and T. Gaylord, "Lithium niobate: summary of physical properties and crystal structure," *Applied Physics A*, vol. 37, no. 4, pp. 191–203, 1985.

[75] `http://physique.unice.fr/sem6/2012-2013/PagesWeb/PT/Guides/niobate.html`.

[76] L. Scriven, "Physics and applications of dip coating and spin coating," *MRS Online Proceedings Library (OPL)*, vol. 121, 1988.

[77] S. Wilson, R. Hunt, and B. Duffy, "The rate of spreading in spin coating," *Journal of Fluid Mechanics*, vol. 413, pp. 65–88, 2000.

[78] J. Danglad-Flores, S. Eickelmann, and H. Riegler, "Deposition of polymer films by spin casting: A quantitative analysis," *Chemical Engineering Science*, vol. 179, pp. 257–264, 2018.

[79] `https://commons.wikimedia.org/wiki/File:Photoresist_of_Photolithography.png`.

[80] B. Hefner and P. Marston, "An acoustical helicoidal wave transducer with applications for the alignment of ultrasonic and underwater systems," *J. Acoust. Soc. Am.*, vol. 106, no. 6, pp. 3313–3316, 1999.

[81] J.-L. Thomas and R. Marchiano, "Pseudo angular momentum and topological charge conservation for nonlinear acoustical vortices," *Phys. Rev. Lett.*, vol. 91, no. 24, p. 244302, 2003.

[82] K. Volke-Sepulveda, A. Santillan, and R. Boullosa, "Transfer of angular momentum to matter from acoustical vortices in free space," *Phys. Rev. Lett.*, vol. 100, p. 024302, 2008.

[83] C. Courtney, C. Demore, H. Wu, A. Grinenko, P. Wilcox, S. Cochran, and B. Drinkwater, "Independent trapping and manipulation of microparticles using dexterous acoustic tweezers," *Appl. Phys. Lett.*, vol. 104, no. 15, p. 154103, 2014.

[84] A. Marzo, S. Seah, B. Drinkwater, D. Sahoo, B. Long, and S. Subramanian, "Holographic acoustic elements for manipulation of levitated objects," *Nat. Commun.*, vol. 6, p. 8661, 2015.

[85] D. Baresch, J. Thomas, and R. Marchiano, "Observation of single-beam gradient force acoustical trap for elastic particles: acoustical tweezers," *Phys. Rev. Lett.*, vol. 116, p. 024301, 2016.

[86] Y. Yang, T. Ma, S. Li, Q. Zhang, J. Huang, Y. Liu, J. Zhuang, Y. Li, X. Du, L. Niu, Y. Xiao, C. Wang, F. Cai, and H. Zhang, "Self-navigated 3d acoustic tweezers in complex media based on time reversal," *AAAS Research*, vol. 2021, p. 9781394, 2021.

[87] Q. Hu, T. Ma, Q. Zhang, J. Wang, Y. Yang, F. Cai, and H. Zheng, "3d acoustic tweezers using a 2d matrix array with time-multiplexed traps," *IEEE T. Ultrason. Ferr.*, vol. 92, p. 063201, 2015.

[88] A. Riaud, J.-L. Thomas, E. Charron, A. Bussonnière, O. Bou Matar, and M. Baudoin, "Anisotropic swirling surface acoustic waves from inverse filtering for on-chip generation of acoustic vortices," *Phys. Rev. Appl.*, vol. 4, no. 3, p. 034004, 2015.

[89] A. Riaud, J.-L. Thomas, M. Baudoin, and O. Bou Matar, "Taming the degeneracy of bessel beams at anisotropic-anisotropic interface: toward threed dimensional control of confined vortical waves," *Phys. Rev. E*, vol. 92, p. 063201, 2015.

[90] A. Riaud, M. Baudoin, J.-L. Thomas, and O. Bou Matar, "Saw synthesis with idts array and the inverse filter: toward a versatile saw toolbox for microfluidic and biological applications," *IEEE T. Ultrason. Ferr.*, 2016.

[91] S. Gspan, A. Meyer, S. Bernet, and M. Risch-Marte, "Optoacoustic generation of a helicoidal ultrasonic beam," *J. Acous. Soc. Am.*, vol. 115, p. 1142, 2004.

[92] J. Ealo, J. Prieeto, and F. Seco, "Airbone ultrasonic vortex generation using flexible ferroelectrets," *IEEE T. Ultrason. Ferr.*, vol. 58, pp. 1561–1657, 2011.

[93] H. Ruben Dario Muelas, J. Pazos-Ospina, and J. Ealo, "A non-expensive massive transducer array to generate helicoidal wavefronts in air.," *Phys. Proc.*, vol. 70, pp. 932–935, 2015.

[94] K. Melde, A. Mark, T. Qiu, and P. Fischer, "Holograms for acoustics," *Nature*, vol. 537, p. 7621, 2016.

[95] M. Terzi, S. Tsysar, P. Yuldashev, M. Karzova, and O. Sapozhnikov, "Generation of a vortex ultrasonic beam with a phase plate with an angular dependence of the thickness," *Moscow Univ. Phys. Bull.*, vol. 72, no. 1, pp. 61–67, 2017.

[96] X. Jiang, Y. Li, B. Liang, J.-C. Cheng, and L. Zhang, "Convert acoustic resonances to orbital angular momentum," *Phys. Rev. Lett.*, vol. 117, no. 034301, 2016.

[97] H. Esfahlani and H. Lissek, "Generation of acoustic helical wavedronts using metasurfaces," *Phys. Rev. B*, vol. 95, p. 024312, 2017.

[98] A. Marzo, A. Ghobrial, L. Cox, M. Caleap, A. Croxford, and B. Drinkwater, "Realization of compact tractor beams using acoustic delay-lines," *Appl. Phys. Lett.*, vol. 110, p. 014102, 2017.

[99] N. Jimenez, V. Sanchez-Morcillo, R. Pico, L. Garcia-Raffi, V. Romero-Garcia, and K. Stalinuas, "High order acousticl bessel beam generation by spiral gratings," *Phys. Proc.*, vol. 70, pp. 245–248, 2015.

[100] N. Jimenez, R. Pico, V. Sanchez-Morcillo, V. Romero-Garcia, L. Garcia-Raffi, and K. Staliunas, "Formation of high order acoustic bessel beams by spiral diffraction gratings," *Phys. Rev. E*, vol. 94, p. 053004, 2016.

[101] N. Jimenez, V. Romero-Gardia, L. Garcia-Raffi, F. Camarena, and K. Staliunas, "Shar acoustic vortex focusing by fresnel-spiral zone plates," *Appl. Phys. Lett.*, vol. 112, p. 204101, 2018.

[102] R. Muelas-Hurtado, J. Ealo, J. Pazos-Ospina, and K. Volke-Sepulveda, "Generation of multiple vortex beam by means of active diffraction gratings," *Appl. Phys. Lett.*, vol. 112, p. 084101, 2018.

[103] M. Baudoin, J. Thomas, R. Al Sahely, J. Gerbedoen, Z. Gong, A. Sivery, O. Bou Matar, N. Smagin, P. Favreau, and A. Vlandas, "Spatially selective mannipulation of cells with single-beam acoustical tweezers," *Nat. Commu.*, vol. 11, p. 4244, 2020.

[104] A. Riaud, M. Baudoin, O. Bou Matar, L. Becerra, and J.-L. Thomas, "Selective manipulation of microscopic particles with precursors swirling rayleigh waves," *Phys. Rev. Appl.*, vol. 7, p. 024007, 2017.

[105] M. Baudoin, J.-C. Gerbedoen, A. Riaud, O. Bou Matar, N. Smagin, and J.-L. Thomas, "Folding a focalized acoustical vortex on a flat holographic transducer: miniaturized selective acoustical tweezers," *Science Adv.*, vol. 5, p. eaav1967, 2019.

[106] L. Yeo and J. Friend, "Surface acoustic waves microfluidics," *Ann. Rev. Fluid Mech.*, vol. 46, pp. 379–406, 2014.

[107] R. Clayton and B. Engquist, "Absorbing boundary conditions for acoustic and elastic wave equations," *Bulletin of the seismological society of America*, vol. 67, no. 6, pp. 1529–1540, 1977.

[108] C. Peng and M. N. Toksöz, "An optimal absorbing boundary condition for elastic wave modeling," *Geophysics*, vol. 60, no. 1, pp. 296–301, 1995.

[109] G. Mur, "Absorbing boundary conditions for the finite-difference approximation of the time-domain electromagnetic-field equations," *IEEE transactions on Electromagnetic Compatibility*, no. 4, pp. 377–382, 1981.

[110] J. Sochacki, R. Kubichek, J. George, W. Fletcher, and S. Smithson, "Absorbing boundary conditions and surface waves," *Geophysics*, vol. 52, no. 1, pp. 60–71, 1987.

[111] J.-P. Berenger, "A perfectly matched layer for the absorption of electromagnetic waves," *Journal of computational physics*, vol. 114, no. 2, pp. 185–200, 1994.

[112] S. Gedney, "Perfectly matched layer absorbing boundary conditions," *Computational Electrodynamics: The finite-different time-domain method*, pp. 273–328, 2005.

[113] S. D. Gedney, "An anisotropic perfectly matched layer-absorbing medium for the truncation of fdtd lattices," *IEEE transactions on Antennas and Propagation*, vol. 44, no. 12, pp. 1630–1639, 1996.

[114] T. Xiao and Q. H. Liu, "Three-dimensional unstructured-grid discontinuous galerkin method for maxwell's equations with well-posed perfectly matched layer," *Microwave and optical technology letters*, vol. 46, no. 5, pp. 459–463, 2005.

[115] Q.-H. Liu and J. Tao, "The perfectly matched layer for acoustic waves in absorptive media," *The Journal of the Acoustical Society of America*, vol. 102, no. 4, pp. 2072–2082, 1997.

[116] X. Yuan, D. Borup, J. W. Wiskin, M. Berggren, R. Eidens, and S. A. Johnson, "Formulation and validation of berenger's pml absorbing boundary for the fdtd simulation of acoustic scattering," *IEEE transactions on ultrasonics, ferroelectrics, and frequency control*, vol. 44, no. 4, pp. 816–822, 1997.

[117] W. Chew and Q. Liu, "Perfectly matched layers for elastodynamics: a new absorbing boundary condition," *Journal of Computational Acoustics*, vol. 4, no. 04, pp. 341–359, 1996.

[118] F. D. Hastings, J. B. Schneider, and S. L. Broschat, "Application of the perfectly matched layer (pml) absorbing boundary condition to elastic wave propagation," *The Journal of the Acoustical Society of America*, vol. 100, no. 5, pp. 3061–3069, 1996.

[119] F. Collino and C. Tsogka, "Application of the perfectly matched absorbing layer model to the linear elastodynamic problem in anisotropic heterogeneous media," *Geophysics*, vol. 66, no. 1, pp. 294–307, 2001.

[120] F. Collino and P. B. Monk, "Optimizing the perfectly matched layer," *Computer methods in applied mechanics and engineering*, vol. 164, no. 1-2, pp. 157–171, 1998.

[121] G. Lazzi and O. P. Gandhi, "On the optimal design of the pml absorbing boundary condition for the fdtd code," *IEEE Transactions on Antennas and Propagation*, vol. 45, no. 5, pp. 914–917, 1997.

[122] J. A. Roden and S. D. Gedney, "Convolution pml (cpml): An efficient fdtd implementation of the cfs–pml for arbitrary media," *Microwave and optical technology letters*, vol. 27, no. 5, pp. 334–339, 2000.

[123] O. Bou Matar, V. Preobrazhensky, and P. Pernod, "Two-dimensional axisymmetric numerical simulation of supercritical phase conjugation of ultrasound in active solid media," *The Journal of the Acoustical Society of America*, vol. 118, no. 5, pp. 2880–2890, 2005.

[124] F. H. Drossaert and A. Giannopoulos, "Complex frequency shifted convolution pml for fdtd modelling of elastic waves," *Wave motion*, vol. 44, no. 7-8, pp. 593–604, 2007.

[125] F. H. Drossaert and A. Giannopoulos, "A nonsplit complex frequency-shifted pml based on recursive integration for fdtd modeling of elastic waves," *Geophysics*, vol. 72, no. 2, pp. T9–T17, 2007.

[126] D. Komatitsch and R. Martin, "An unsplit convolutional perfectly matched layer improved at grazing incidence for the seismic wave equation," *Geophysics*, vol. 72, no. 5, pp. SM155–SM167, 2007.

[127] E. Bécache, P. G. Petropoulos, and S. D. Gedney, "On the long-time behavior of unsplit perfectly matched layers," *IEEE Transactions on Antennas and Propagation*, vol. 52, no. 5, pp. 1335–1342, 2004.

[128] Y. Li, O. B. Matar, V. Preobrazhensky, and P. Pernod, "Convolution-perfectly matched layer (c-pml) absorbing boundary condition for wave propagation in piezoelectric solid," in *2008 IEEE Ultrasonics Symposium*, pp. 1568–1571, IEEE, 2008.

[129] E. Bécache, S. Fauqueux, and P. Joly, "Stability of perfectly matched layers, group velocities and anisotropic waves," *Journal of Computational Physics*, vol. 188, no. 2, pp. 399–433, 2003.

[130] K. C. Meza-Fajardo and A. S. Papageorgiou, "A nonconvolutional, split-field, perfectly matched layer for wave propagation in isotropic and anisotropic elastic media: Stability analysis," *Bulletin of the Seismological Society of America*, vol. 98, no. 4, pp. 1811–1836, 2008.

[131] L. Wang and S. I. Rokhlin, "Modeling of wave propagation in layered piezoelectric media by a recursive asymptotic method," *IEEE transactions on ultrasonics, ferroelectrics, and frequency control*, vol. 51, no. 9, pp. 1060–1071, 2004.

[132] F. Chagla and P. M. Smith, "Finite difference time domain methods for piezoelectric crystals," *IEEE transactions on ultrasonics, ferroelectrics, and frequency control*, vol. 53, no. 10, pp. 1895–1901, 2006.

[133] W. Chew, J. Jin, and E. Michielssen, "Complex coordinate stretching as a generalized absorbing boundary condition," *Microwave and Optical Technology Letters*, vol. 15, no. 6, pp. 363–369, 1997.

[134] M. Kuzuoglu and R. Mittra, "Frequency dependence of the constitutive parameters of causal perfectly matched anisotropic absorbers," *IEEE Microwave and Guided wave letters*, vol. 6, no. 12, pp. 447–449, 1996.

[135] A. Taflove, S. C. Hagness, and M. Piket-May, "Computational electromagnetics: the finite-difference time-domain method," *The Electrical Engineering Handbook*, vol. 3, 2005.

[136] Y. Zheng and X. Huang, "Anisotropic perfectly matched layers for elastic waves in cartesian and curvilinear coordinates," tech. rep., Massachusetts Institute of Technology. Earth Resources Laboratory, 2002.

[137] D. Appelö and G. Kreiss, "A new absorbing layer for elastic waves," *Journal of Computational Physics*, vol. 215, no. 2, pp. 642–660, 2006.

[138] Y. Li, *Développement d'outils de simulation numérique pour l'élastodynamique non linéaire: application à l'imagerie acoustique de*

défauts à l'aide de transducteur à cavité chaotique. PhD thesis, Ecole centrale de Lille, 2009.

[139] J. W. Goodman, "Introduction to fourier optics, roberts & co," *Publishers, Englewood, Colorado*, 2005.

[140] E. G. Williams, *Fourier acoustics: sound radiation and nearfield acoustical holography*. Academic press, 1999.

[141] P. Wu, R. Kazys, and T. Stepinski, "Analysis of the numerically implemented angular spectrum approach based on the evaluation of two-dimensional acoustic fields. part i. errors due to the discrete fourier transform and discretization," *The Journal of the Acoustical Society of America*, vol. 99, no. 3, pp. 1339–1348, 1996.

[142] P. Wu, R. Kazys, and T. Stepinski, "Optimal selection of parameters for the angular spectrum approach to numerically evaluate acoustic fields," *The Journal of the Acoustical Society of America*, vol. 101, no. 1, pp. 125–134, 1997.

[143] R. J. Zemp, J. Tavakkoli, and R. S. Cobbold, "Modeling of nonlinear ultrasound propagation in tissue from array transducers," *The Journal of the Acoustical Society of America*, vol. 113, no. 1, pp. 139–152, 2003.

[144] P. T. Christopher and K. J. Parker, "New approaches to the linear propagation of acoustic fields," *The Journal of the Acoustical Society of America*, vol. 90, no. 1, pp. 507–521, 1991.

[145] X. Zeng and R. J. McGough, "Evaluation of the angular spectrum approach for simulations of near-field pressures," *The Journal of the Acoustical Society of America*, vol. 123, no. 1, pp. 68–76, 2008.

[146] X. Zeng and R. J. McGough, "Optimal simulations of ultrasonic fields produced by large thermal therapy arrays using the angular spectrum approach," *The Journal of the Acoustical Society of America*, vol. 125, no. 5, pp. 2967–2977, 2009.

[147] Y. Jing, "On the use of an absorption layer for the angular spectrum approach (l)," *The Journal of the Acoustical Society of America*, vol. 131, no. 2, pp. 999–1002, 2012.

[148] D. J. Vezzetti, "Propagation of bounded ultrasonic beams in anisotropic media," *The Journal of the Acoustical Society of America*, vol. 78, no. 3, pp. 1103–1108, 1985.

[149] L. Brekhovskikh, *Waves in layered media*, vol. 16. Elsevier, 2012.

[150] F. Crick and A. Hughes, "The physical properties of cytoplasm," *Experimental Cell Research*, vol. 1, no. 1, pp. 37–80, 1950.

[151] S. B. Smith, L. Finzi, and C. Bustamante, "Direct mechanical measurements of the elasticity of single dna molecules by using magnetic beads," *Science*, vol. 258, no. 5085, pp. 1122–1126, 1992.

[152] K. C. Neuman, E. H. Chadd, G. F. Liou, K. Bergman, and S. M. Block, "Characterization of photodamage to escherichia coli in optical traps," *Biophysical journal*, vol. 77, no. 5, pp. 2856–2863, 1999.

[153] Y. Liu, D. Cheng, G. Sonek, M. Berns, C. Chapman, and B. Tromberg, "Evidence for localized cell heating induced by infrared optical tweezers," *Biophysical journal*, vol. 68, no. 5, pp. 2137–2144, 1995.

[154] Y. Liu, G. Sonek, M. Berns, and B. Tromberg, "Physiological monitoring of optically trapped cells: assessing the effects of confinement by 1064-nm laser tweezers using microfluorometry," *Biophysical Journal*, vol. 71, no. 4, pp. 2158–2167, 1996.

[155] A. Lenshof and T. Laurell, "Continuous separation of cells and particles in microfluidic systems," *Chemical Society Reviews*, vol. 39, no. 3, pp. 1203–1217, 2010.

[156] G. Sitters, D. Kamsma, G. Thalhammer, M. Ritsch-Marte, E. J. Peterman, and G. J. Wuite, "Acoustic force spectroscopy," *Nature methods*, vol. 12, no. 1, pp. 47–50, 2015.

[157] D. J. Collins, B. Morahan, J. Garcia-Bustos, C. Doerig, M. Plebanski, and A. Neild, "Two-dimensional single-cell patterning with one cell per well driven by surface acoustic waves," *Nature communications*, vol. 6, no. 1, pp. 1–11, 2015.

[158] H. Bruus, "Acoustofluidics 2: Perturbation theory and ultrasound resonance modes," *Lab on a Chip*, vol. 12, no. 1, pp. 20–28, 2012.

[159] F. S. Foster, C. J. Pavlin, K. A. Harasiewicz, D. A. Christopher, and D. H. Turnbull, "Advances in ultrasound biomicroscopy," *Ultrasound in medicine & biology*, vol. 26, no. 1, pp. 1–27, 2000.

[160] J. Hultström, O. Manneberg, K. Dopf, H. M. Hertz, H. Brismar, and M. Wiklund, "Proliferation and viability of adherent cells manipulated

by standing-wave ultrasound in a microfluidic chip," *Ultrasound in medicine & biology*, vol. 33, no. 1, pp. 145–151, 2007.

[161] M. A. Burguillos, C. Magnusson, M. Nordin, A. Lenshof, P. Augustsson, M. J. Hansson, E. Elmer, H. Lilja, P. Brundin, T. Laurell, *et al.*, "Microchannel acoustophoresis does not impact survival or function of microglia, leukocytes or tumor cells," *PloS one*, vol. 8, no. 5, p. e64233, 2013.

[162] V. Marx, "Biophysics: using sound to move cells," *Nature methods*, vol. 12, no. 1, pp. 41–44, 2015.

[163] T. L. Szabo, *Diagnostic ultrasound imaging: inside out*. Academic press, 2004.

[164] A. Riaud, M. Baudoin, O. B. Matar, L. Becerra, and J.-L. Thomas, "Selective manipulation of microscopic particles with precursor swirling rayleigh waves," *Physical Review Applied*, vol. 7, no. 2, p. 024007, 2017.

[165] A. Keloth, O. Anderson, D. Risbridger, and L. Paterson, "Single cell isolation using optical tweezers," *Micromachines*, vol. 9, no. 9, p. 434, 2018.

[166] R. Arshadi and R. S. Cobbold, "A pioneer in the development of modern ultrasound: Robert william boyle (1883–1955)," *Ultrasound in medicine & biology*, vol. 33, no. 1, pp. 3–14, 2007.

[167] G. T. Silva, J. H. Lopes, J. P. Leão-Neto, M. K. Nichols, and B. W. Drinkwater, "Particle patterning by ultrasonic standing waves in a rectangular cavity," *Physical Review Applied*, vol. 11, no. 5, p. 054044, 2019.

[168] F. Guo, Z. Mao, Y. Chen, Z. Xie, J. P. Lata, P. Li, L. Ren, J. Liu, J. Yang, M. Dao, *et al.*, "Three-dimensional manipulation of single cells using surface acoustic waves," *Proceedings of the National Academy of Sciences*, vol. 113, no. 6, pp. 1522–1527, 2016.

[169] J. Lee, S.-Y. Teh, A. Lee, H. H. Kim, C. Lee, and K. K. Shung, "Single beam acoustic trapping," *Applied physics letters*, vol. 95, no. 7, p. 073701, 2009.

[170] J. Lee, C. Lee, H. H. Kim, A. Jakob, R. Lemor, S.-Y. Teh, A. Lee, and K. K. Shung, "Targeted cell immobilization by ultrasound microbeam," *Biotechnology and bioengineering*, vol. 108, no. 7, pp. 1643–1650, 2011.

[171] M. Settnes and H. Bruus, "Forces acting on a small particle in an acoustical field in a viscous fluid," *Physical Review E*, vol. 85, no. 1, p. 016327, 2012.

[172] P. Augustsson, J. T. Karlsen, H.-W. Su, H. Bruus, and J. Voldman, "Iso-acoustic focusing of cells for size-insensitive acousto-mechanical phenotyping," *Nature communications*, vol. 7, no. 1, pp. 1–9, 2016.

[173] J. Happel and H. Brenner, *Low Reynolds number hydrodynamics: with special applications to particulate media*, vol. 1. Springer Science & Business Media, 2012.

[174] J. Teissie and M.-P. ROLS, "Manipulation of cell cytoskeleton affects the lifetime of cell membrane electropermeabilization," *Annals of the New York Academy of Sciences*, vol. 720, no. 1, pp. 98–110, 1994.

[175] M. B. Zeigler and D. T. Chiu, "Laser selection significantly affects cell viability following single-cell nanosurgery," *Photochemistry and photobiology*, vol. 85, no. 5, pp. 1218–1224, 2009.

[176] J. T. Parsons, A. R. Horwitz, and M. A. Schwartz, "Cell adhesion: integrating cytoskeletal dynamics and cellular tension," *Nature reviews Molecular cell biology*, vol. 11, no. 9, pp. 633–643, 2010.

[177] S. Block, D. Blair, and H. Berg, "Compliance of bacterial flagella measured with optical tweezers," *Nature*, vol. 338, no. 6215, p. 514, 1989.

[178] S. Suresh, "Biomechanics and biophysics of cancer cells," *Acta biomaterialia*, vol. 3, no. 4, pp. 413–438, 2007.

[179] Z. Gong and M. Baudoin, "Particle assembly with synchronized acoustic tweezers," *Physical Review Applied*, vol. 12, no. 2, p. 024045, 2019.

[180] P. Jing, Y. Liu, E. G. Keeler, N. M. Cruz, B. S. Freedman, and L. Y. Lin, "Optical tweezers system for live stem cell organization at the single-cell level," *Biomedical optics express*, vol. 9, no. 2, pp. 771–779, 2018.

[181] D. Foresti and D. Poulikakos, "Acoustophoretic contactless elevation, orbital transport and spinning of matter in air," *Physical review letters*, vol. 112, no. 2, p. 024301, 2014.

[182] A. Marzo and B. W. Drinkwater, "Holographic acoustic tweezers," *Proceedings of the National Academy of Sciences*, vol. 116, no. 1, pp. 84–89, 2019.

[183] R. Hirayama, D. M. Plasencia, N. Masuda, and S. Subramanian, "A volumetric display for visual, tactile and audio presentation using acoustic trapping," *Nature*, vol. 575, no. 7782, pp. 320–323, 2019.

[184] K. Svoboda and S. Block, "Biological applications of optical forces," *Ann. Rev. Bioph. Biomol. Struct.*, vol. 23, pp. 247–285, 1994.

[185] K. Svoboda, C. Schmidt, B. Schnapp, and S. Block, "Direct observation of kinesin stepping by optical trapping interferometry," *Nature*, vol. 365, p. 6447, 1994.

[186] J. Finer, R. Simmons, and J. Spudich, "Single myosin molecule mechanics: piconewton forces and nanometre steps," *Nature*, vol. 368, pp. 113–119, 1996.

[187] S. Smith, L. Finzi, and C. Bustamante, "Direct mechanical measurement of the elasticity of single dna molecules by using magnetic beads," *Science*, vol. 258, pp. 1122–1126, 1992.

[188] S. Smith, Y. Cui, and C. Bustamante, "Overstretching b-dna: the elastic response of individual double-stranded and single stranded dna molecules," *Science*, vol. 271, pp. 795–799, 2011.

[189] T. Strick, J.-F. Allemand, D. Bensimon, and V. Croquette, "The elasticity of a single supercoiled dna molecule," *Science*, vol. 271, pp. 1835–1837, 1996.

[190] M. Wand, H. Yin, R. Landick, J. Gelles, and S. Block, "Stretching dna with optical tweezers," *Biophysical journal*, vol. 72, pp. 1335–1346, 1997.

[191] F. Fazam and S. Block, "Optical tweezers study life under tension," *Nature Photon.*, vol. 5, pp. 318–321, 2011.

[192] J. Dong, C. Castro, M. Boyce, M. Lang, and S. Lindquist, "Optical trapping with high forces reveals unexpected behaviors of prion fibrils," *Nature Struct. Mol. Biol.*, vol. 17, pp. 1422–1430, 2010.

[193] A. Jannasch, A. Demirors, P. Van Oostrum, A. Van Blaaderen, and E. Schaffer, "Nanonewton optical force trap employing anti-refelection coated, high refractive-index titania microsphere," *Nature Photon.*, vol. 6, pp. 469–473, 2012.

[194] K. Neuman, E. Chadd, G. Liou, K. Bergman, and S. Block, "Characterization of photodamage to Escherichia coli in optical traps," *Biophys. J.*, vol. 77, pp. 2856–2863, 1999.

[195] Y. Liu, D. Cheng, G. Sonek, M. Berns, C. Chapman, and B. Tromberg, "Evidence of localized cell heating induced by infrared optical tweezers," *Biophys. J.*, vol. 68, pp. 2137–2144, 1995.

[196] Y. Liu, G. Sonek, M. Berns, and B. Tromberg, "Assessing the effects of confinement by 1064-nm laser tweezers using microflurometry," *Biophys. J.*, vol. 71, pp. 2158–2167, 1996.

[197] A. Blasquez, "Optical tweezers: Phototoxicity and thermal stress in cells and biomolecules," *Micromachines*, vol. 10, p. 507, 2019.

[198] M. Baudoin and J.-L. Thomas, "Acoustical tweezers for particle and fluid micromanipulation," *Annu. Rev. Fluid Mech.*, vol. 52, pp. 205–234, 2020.

[199] M. Ghanem, A. Maxwell, Y.-N. Wang, B. Cunitz, V. Khokhlova, O. Sapozhnikov, and M. Bailey, "Noninvasive acoustic manipulation of objects in a living body," *Proc. Nat. Ac. Sci.*, vol. 117, pp. 16848–16855, 2020.

[200] W.-C. Lo, C.-H. Fan, Y.-J. Ho, C.-W. Lin, and C.-K. Yeh, "Tornado-inspired acoustic vortex tweezer for trapping and manipulating microbubbles," *Proc. Nac. Ac. Sci.*, vol. 118, p. e2023188118, 2021.

[201] S. Jimenez-Gambin, N. Jimenez, J. Blenlloch, and F. Camarena, "Holograms to focus arbitrary ultrasonic fields through the skull," *Phys. Rev. Appl.*, vol. 12, no. 1, p. 014016, 2019.

[202] D. Baresch and V. Garbin, "Acoustic trapping of microbubbles in complex environments and controlled payload release," *Proc. Nat. Ac. Sci. USA*, vol. 117, pp. 15490–15496, 2020.

[203] Z. Gong and M. Baudoin, "Single beam acoustical tweezers based on focused beams: A numerical analysis of 2d and 3d trapping capabilities," *Submitted*, 2022.

[204] D. Baresch, J.-L. Thomas, and R. Marchiano, "Spherical vortex beams of high radial degree for enhanced single-beam tweezers," *J. Appl. Phys.*, vol. 113, no. 18, p. 184901, 2013.

[205] R. Shilton, M. Travagliati, F. Beltram, and M. Cecchini, "Nanoliter-droplet acoustic streaming via ultra high frequency surface acoustic waves," *Shilton, R.J. and Travagliati, M. and Beltram, F. and Cecchini, M.*, vol. 26, pp. 4941–4946, 2014.

[206] L. Le Brizoual, F. Sarry, O. Elmazria, P. Alnot, S. Ballandras, and T. Pastureaud, "Ghz frequency zno/si saw device," *IEEE T. Ultrason. Ferr.*, vol. 55, pp. 442–449, 2008.

[207] Z. Gong and M. Baudoin, "Three-dimensional trapping and dynamic axial manipulation with frequency-tuned spiraling acoustical tweezers: A theoretical study," *Phys. Rev. Appl.*, vol. 16, p. 024034, 2021.

[208] Z. Gong and M. Baudoin, "Three-dimensional trapping and dynamic axial manipulation with frequency-tuned spiraling acoustical tweezers: a theoretical study," *Physical Review Applied*, vol. 16, no. 2, p. 024034, 2021.

[209] R. D. Muelas-Hurtado, J. L. Ealo, and K. Volke-Sepúlveda, "Active-spiral fresnel zone plate with tunable focal length for airborne generation of focused acoustic vortices," *Applied Physics Letters*, vol. 116, no. 11, p. 114101, 2020.

Abstract (English)

Acoustical tweezers based on focused acoustical vortices open some tremendous perspectives for the in vitro and in vivo remote and selective manipulation of millimetric down to micrometric objects, with combined selectivity and applied forces out of reach with any other contactless manipulation technique. The first demonstration of 3D particle trapping and manipulation with acoustical vortices was achieved in 2016 with an array of transducers driven by programmable electronics. More recently it has been proposed to use holographic acoustical tweezers based on Archimedes-Fermat spiraling interdigitated transducers (S-IDTs) to design miniaturized acoustical tweezers compatible with a standard microscopy environment. In this PhD, we have explored the possibilities offered by these kinds of acoustical tweezers to address the following unsolved issues: 1) Manipulate selectively and organize human cells with large forces (200pN) without pre-tagging and without affecting the cells viability. 2) Create ultra-high frequency tweezers (250 MHz) with high spatial selectivity able to trap and position 4 microns individual microparticles with NanoNewton forces. 3) Manipulate microparticles in 3D in a free environment and translate them axially without motion of the transducer. These goals have been achieved by developing (i) a new numerical code based the combination of Finite Element simulation of the source and Angular Spectrum propagation of the wave and (ii) appropriate microfabrication procedures, which helped us design and fabricate tweezers with the good capabilities. This work open perspectives in microbiology to study cells interaction and their response to mechanical solicitation but also for acoustic forces spectroscopy.

Abstract (French)

Les pinces acoustiques basées sur les vortex acoustiques focalisées ouvrent de nouvelles perspectives pour la manipulation sans contact et sélective d'objets millimétriques à micrométriques, avec une sélectivité et des forces appliquées difficilement atteignables avec les autres méthodes. La première démonstration du piégeage et de la manipulation 3D d'une particule avec des vortex acoustiques a été effectuée en 2016 avec une matrice de transducteur ultrasonores pilotés par une électronique programmable. Récemment, il a été proposé d'utiliser des pinces acoustiques holographiques basées sur des transducteurs interdigités en spirales pour développer des pinces acoustiques miniaturisées compatibles avec un environnement de microscopie standard. Dans cette thèse, nous avons exploré les possibilités offertes par ce type de pince acoustiques pour adresser les problèmes suivants. 1) Manipuler sélectivement et organiser des cellules humaines avec des forces importantes (200 pN) sans pré-marquage et sans affecter la viabilité des cellules. 2) Créer des pinces acoustiques très haute fréquence (250 MHz) avec une forte sélectivité et capables de manipuler des microparticules de 4 microns avec des forces de l'ordre du NanoNewton. 4) Déplacer des microparticules en 3D dans un environnement libre et les translater axialement sans déplacement du transducteur. Ces objectifs ont été atteints en développant de nouvelles méthodes numériques et des procédure expérimentales adaptées, qui nous ont permis de concevoir des pinces acoustiques avec les capacités recherchées. Ce travail ouvre des perspectives dans le domaine de la microbiologie pour étudier les interactions cellulaires et leur réponse à des sollicitations mécanique, mais aussi pour la spectroscopie de force acoustique.